Metal-Phenolic Assembly for Engineering Multifunctional Materials: Beyond Hard Templates

Gan Lin
ORCID ID: 0000-0003-2743-4901

Submitted in total fulfillment of the requirements of the degree of Doctor of Philosophy

November 2019

Department of Chemical and Biomolecular Engineering
The University of Melbourne

Produced on archival quality paper

Abstract

Metal-phenolic coordination assembly for the fabrication of multifunctional materials for diverse applications, including catalysis, pharmaceutical, nanomedicine and sensing, has attracted much attention in recent years. However, the bulk of the literature of metal-phenolic materials has been focused on the assembly on hard templates using a single ligand. There is a scope in advancing the field by investigating the versatility of the assembly system in terms of different phenolic ligands, templates and assembly techniques, which could result in novel multifunctional materials. In this thesis, different assembly techniques, particularly the use of hard and soft templates and self-assembly, were explored to create metal-phenolic materials, including thin films and particles. Metal-phenolic assembly on traditional hard templates but using a complex multicomponent phenolic mixture was first investigated (Chapter 3). The metal–phenolic assembly exhibits selective properties in a series of complex multicomponent systems (including crude plant extracts), in which metal ions (Fe^{III}) selectively assembles with low abundant but multivalent phenolic compounds (e.g., myricetrin and quercetrin) to form thin films. This selective property was independent of the substrate properties (e.g., size, morphologies and surface charge) and the resultant metal-phenolic films demonstrated promising antioxidant properties. In Chapter 4, the transition from hard templates to microemulsions (soft) templates is described. Here, pH-sensitive poly(ethylene glycol) nanoparticles with tunable sizes and morphologies were synthesized by adjusting metal-phenolic crosslinking within the microemulsions. In Chapter 5, a template-free assembly technique was also explored to create metal-phenolic particles, which can sense and swim towards an external light source with the velocity tunable by light intensity. Nuclear magnetic resonance, confocal Raman microscopy and quantum mechanics calculations provided insight of the mechanism of light-induced movement of the metal-phenolic particles. Altogether, the

metal-phenolic materials engineered through different assembly approaches presented herein show well-tailored structures and unique properties for various biomedical and engineering applications.

Declaration

This is to certify that:

(i) The thesis comprises only my original work towards the degree of Doctor of Philosophy (PhD);

(ii) Due acknowledgement has been made in the text to all other materials used;

(iii) The thesis is fewer than 100,000 words in length, exclusive of tables, bibliographies, appendices, and footnotes.

Gan Lin

Preface

Chapter 3 of this thesis has been published in the following article:

1. **Lin G,** Rahim MA, Leeming MG, Cortez-Jugo C, Besford QA, Ju Y, Zhong QZ, Johnston ST, Zhou J, Caruso F. Selective Metal-Phenolic Assembly from Complex Multicomponent Mixtures. *ACS Appl. Mater. Interfaces*. 2019;11(19):17714-17721.

In Chapter 3, Dr. Michael Leeming provided assistance with liquid chromatography-mass spectrometry (LC-MS) experiments and data analysis. Dr. Stuart T. Johnston provided assistance in the computational simulation of film formation. Qizhi Zhong performed the AFM measurements of the MPN capsules. Dr. Md. Arifur Rahim and Dr. Quinn A. Besford gave useful advice and discussion on the mechanism behind the selective metal-phenolic assembly in complex multicomponent mixtures.

In Chapter 4, Dr. Christina Cortez-Jugo provided useful assistance and valuable advice on cell experiments. Dr. Joseph J. Richardson and Dr. Quinn A. Besford provided assistance with small angle X-ray scattering (SAXS) experiments. The fitting analysis of SAXS data was performed by Dr. Tim Ryan (Australian Synchrotron). Contact angle measurements were carried out with help from Dr. Shuaijun Pan.

In Chapter 5, Dr. Joseph J. Richardson and Dr. Quinn A. Besford provided useful assistance and advice in the motion experiments of the metal-phenolic particles. Paul Brannon provided useful advice in recording the movement of metal-phenolic particles. Dr. Heba Amhed and Dr. Amgad R. Rezk provided assistance in confocal Raman microscopy experiments. Dr. Andrew J. Christofferson provided assistance in the quantum mechanics (QM) calculations using SMD model. Dr. Jiajing Zhou and Zhixing Lin assisted in TEM and SEM experiments and analyses.

Professor Frank Caruso contributed to the development of ideas and provided useful advice in experiment design in the above chapters.

Publications

1. **Lin G**, Rahim MA, Leeming MG, Cortez-Jugo C, Besford QA, Ju Y, Zhong QZ, Johnston ST, Zhou J, Caruso F. Selective Metal-Phenolic Assembly from Complex Multicomponent Mixtures. *ACS Appl. Mater. Interfaces*. 2019;11(19):17714-17721.
2. Rahim MA, **Lin G**, Tomanin PP, Ju Y, Barlow A, Björnmalm M, Caruso, F. Self-Assembly of a Metal-Phenolic Sorbent for Broad-Spectrum Metal Sequestration. *ACS Appl. Mater. Interfaces.* 2020;12(3):3746-3754.
3. Zhou J, Lin Z, Lu D, Pan S, Ju Y, Li S, Han Y, Chen J, **Lin G**, Duan H, Richardson JJ, Caruso F. Reversible Supramolecular Complexes for Versatile Nanoparticle Engineering. (In preparation)
4. **Lin G**, Cortez-Jugo C, Ju Y, Besford QA, Ryan T, Pan S, Richardson JJ, Caruso F. Poly(ethylene glycol) Nanoparticles with Tunable Sizes and Morphologies via Adjusting Metal-Phenolic Crosslinking in Microemulsion. (In preparation)
5. **Lin G**, Richardson JJ, Amhed H, Besford QA, Lin Z, Rezk AR, Zhou J, Cortez-Jugo C, Yeo LY, Caruso F. Light-Steered Movement of Metal-Phenolic Particles. (In preparation)

Presentations

The following oral presentations were delivered during the course of the PhD candidature:

1. **Lin, G.**, "Engineering Multifunctional Films and Particles by Metal-Phenolic Assembly" PhD Completion Seminar, October 2019, Melbourne, Australia.

2. **Lin, G.**, "Light-Steered Movement of Metal-Phenolic Crystals." Nanostructured Interfaces and Materials Science (NIMS) Meeting, May 2019, Melbourne, Australia.

3. **Lin, G.**, "Antioxidant Nanofilms from Selective Metal-Phenolic Assembly in Eucalyptus Leaf Extracts." Convergent Bio-Nano Science & Technology (CBNS) Melbourne Nodes Meeting, December 2018, Melbourne, Australia.

4. **Lin, G.**, "Selective Metal-Phenolic Assembly in Complex Multicomponent Systems." Nanostructured Interfaces and Materials Science (NIMS) Meeting, September 2018, Melbourne, Australia.

5. **Lin, G.**, "Synthesis of Metal-Phenolic Nanoparticles by Microemulsion." Nanostructured Interfaces and Materials Science (NIMS) Meeting, September 2017, Melbourne, Australia.

6. **Lin, G.**, "Synthesis of Metal-Phenolic Nanoparticles by Microemulsion." Particulate Fluids Processing Centre (PFPC) Seminar, August 2017, Melbourne, Australia.

7. **Lin, G.**, "Metal-phenolic nanoflowers." Nanostructured Interfaces and Materials Science (NIMS) Meeting, December 2016, Melbourne, Australia.

Acknowledgements

I would like to express my gratitude to my supervisor, Prof. Frank Caruso, for giving me the opportunity to pursue my PhD in the Nanostructured Interfaces and Materials Science (NIMS) group at the University of Melbourne. Great thanks and appreciation to him for providing the advanced facilities and critical research environment in his group, allowing me to think and explore the scientific questions in my research field, and also to work on high-quality research projects in my PhD. I am grateful to him for giving me the freedom to explore my own ideas, and for the kind support and guidance on shaping the research projects. His guidance and advice shaped me into a better and mature scientist and will remind me in the future.

I also would like express my gratitude to my co-supervisors, Dr. Christina Cortez-Jugo and Dr. Md. Arifur Rahim, for the valuable discussions of the scientific questions in my research project. A huge appreciation to Christina and Rahim for encouraging me to be a better scientist. I am also thankful to all former and current colleagues in NIMS group for the kind help during the past years. It is great honor for me to have colleagues, like Dr. Joseph J. Richardson, Dr. Quinn A. Besford, Dr Yi Ju, Dr Francesca Cavalieri, Dr. Jiajing Zhou, Zhixing Lin, Shuaijun Pan, Dr. Junglin Guo, Dr. Tomoya Suma, Dr. Jiwei Cui, Dr. Nadja Bertleff-Zieschang, Dr. Mattias Björnmalm, Jingqu Chen, Dr. Danzi Song, Dr Jianhua Li, Dr. Matthew Faria, Dr. Wenjie Zhang, Dr. Gyeongwon Yun, Yutian Ma, Dr. Marcin Wojnilowicz, Professor Jing Hu, Pietro Pacchin Tomanin, Ewa Czuba-Wojnilowicz, Dr. Alessia Weiss, Dr Alessia Amodio, Yiyuan Han, Agata Glab, Yingjie Hu, Shiyao Li, Yijiao Qu, Jiaying Song, and Qizhi Zhong, Dr. Andrew Mitchell. They provided me with many valuable advice and experience in the past years. I am also thankful to Melanie Hutchins, Maryline Chee and Catherine Eyre for manuscript editing and numerous paperwork during my candidature. Great appreciation is also expressed to Jenny Tran and Dr. Steve Spoljaric for the chemical ordering and lab techniques.

Also big thanks to Paul Brannon (Advanced Fluorescence Imaging facility) for his advice on imaging.

I also would like to express my great appreciation to my research collaborators, Professor Leslie Y. Yeo (RMIT, Australia), Professor Trevor Smith (The University of Melbourne, Australia), Dr. Heba Amhed (RMIT, Australia), Dr. Amgad R. Rezk (RMIT, Australia), Dr. Andrew J. Christofferson (RMIT, Australia), Dr. Christopher Hall (The University of Melbourne, Australia), Dr. Jingwei Hou (University of Queensland), and Dr. Tim Ryan (Australian synchrotron, Australia) for the great help and discussion throughout my PhD.

Great thanks and appreciation are expressed to the kind support from the Department of Chemical Engineering and The University of Melbourne during my PhD, particularly for the financial support (Melbourne Research Scholarship) provided by the University of Melbourne. Great thanks to my PhD committee chair, Professor Greg Qiao (The University of Melbourne, Australia) for the valuable discussion of the scientific questions behind my research projects.

I am also thankful to Professor Gang Liu and Professor Peng Mi in China. They were always cheering me up and encouraging me to dream big through the bad time. Finally, I appreciate the kind support from my family: dad (Yibing Lin), mom (Meixian Lin) and younger brother (Quan Lin).

Table of Contents

Chapter 1

Introduction

1.1. Introduction

Billions of years of evolution has endowed nature with the capacity to develop complex naturally-occurring materials with elaborate hierarchical structures and fascinating functions. Typical examples include the strong and tough spider silk[1-3], the extensible and self-healing filamentous extensions (byssus) of mussels[4-6], the self-cleaning property of lotus leaves and many others,[7-9] all of which offers great inspiration for researchers in materials science to fabricate synthetic materials with superior properties that mimic nature.[10-12] One typical example is the mussel: the byssus thread is able to secrete adhesive proteins to adhere to various surfaces, while the cuticles that contains rich Fe-catecholate complexes offers great mechanical and self-healing properties. These outstanding capacities of mussels has inspired the development of various manmade materials for diverse applications, including adhesives, biomedicine, self-healing materials and multifunctional surface coatings.[10, 13-15]

One recent pioneering study reported by Ejima et al. offered a novel strategy for the universal surface coating by virtue of the metal-phenolic complexes, which is formed by the coordination between metal ions and natural phenolic ligands onto a wide variety of substrates irrespective of substrates properties (e.g. size, shape and surface charge).[16] A great variety of phenolic compounds, including small phenolic ligands (e.g. gallic acid)[17], dietary flavonoids (e.g. myricetin)[18], large polyphenols (tannic acid)[16, 19-21], and synthetic polymer-phenol conjugates[21-23], can be used as phenolic building blocks for film formulation. Moreover, various metals can be used to impart the films with different functionalities.[19] However, most of these studies have been focused on hard planar and particulate templates, often using a single phenolic ligand. The investigation of metal-phenolic assembly systems using different phenolic ligands and assembly techniques could potentially result in novel functional materials and advance this field.

This chapter begins with an overview of phenolic compounds, including definition,

classification and properties (e.g. biological and chemical properties). Next, the general approaches for engineering hollow nanostructures and particles will be presented. A brief review on metal-organic coordination polymer will then be presented, followed by the description of metal-phenolic networks and its current state and limitations. This chapter ends with a brief description of the scope of this thesis.

1.2. Polyphenols

Phenolic compounds are a class of natural or synthetic compounds that bear multiple phenolic structural units (Figure 1.1).[24] They are generally produced as byproducts of plant metabolism and can serve to protect the plant from ultraviolet radiation or from attack by pathogens.[25] From a strictly chemical view point, polyphenols are molecules that possess at least one benzene ring with a great variety of di- and/or trihydroxyphenyl units according to the definition by White, Bate-Smith, Swain, and Haslam (WBSSH)—the four big phytochemists who made numerous seminal investigations on polyphenol.[26]

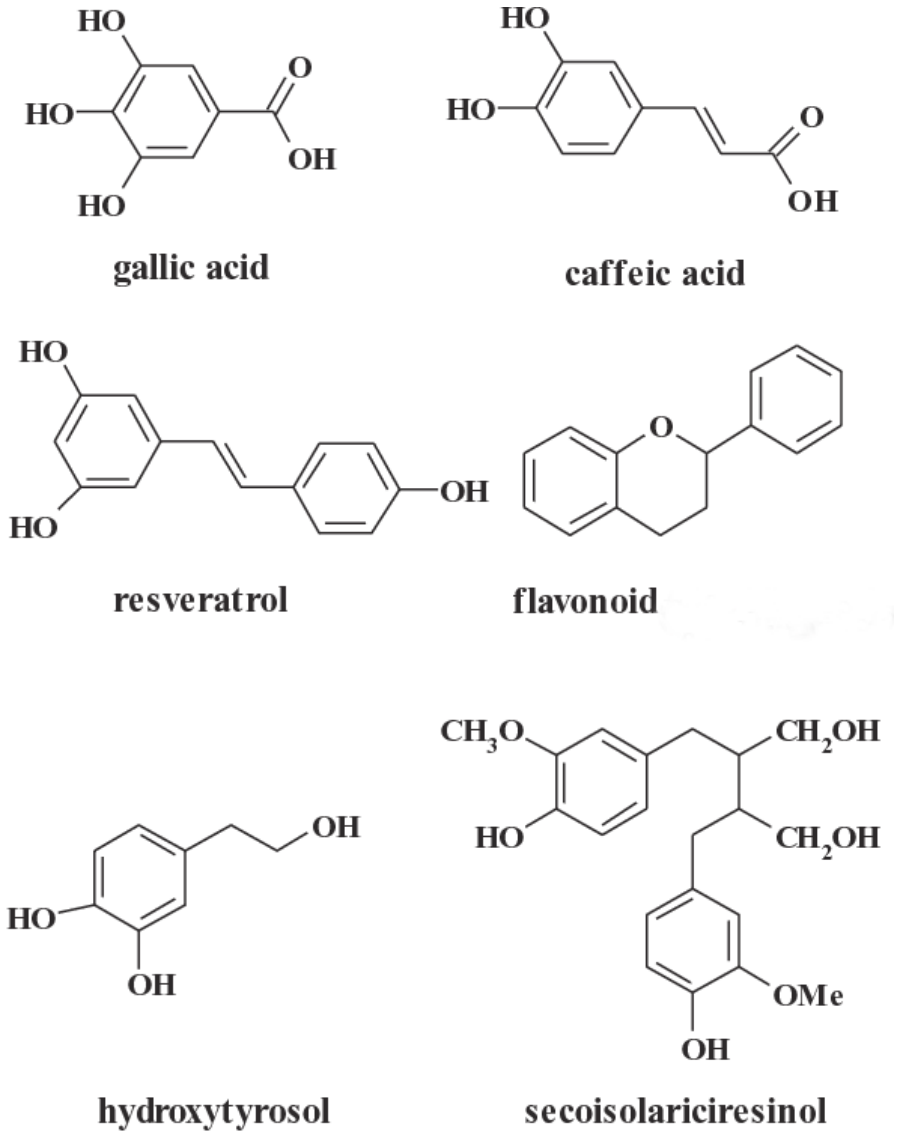

Figure 1.1. Chemical structures of some representative polyphenol (adapted from reference 24).[24]

So far, over 8000 phenolic compounds have been identified and they are usually found combined with a variety of natural sugars units (e.g. mono- and polysaccharides) and ester and/or methyl esters groups. Based on the chemical structure, these phenolic compounds can be divided into several subclasses, including phenolic acids, coumarins, flavonoids, stilbenes and lignans, as shown in Figure 1.2.[25, 27] Among them, flavonoids present the largest subclass and along with phenolic acids and lignans, are regarded as the main dietary phenolic compounds.[27-29] Phenolic compounds are important constituents of vegetable and fruit,

contributing to the taste, color and nutritional properties of fruit and vegetables.[25]

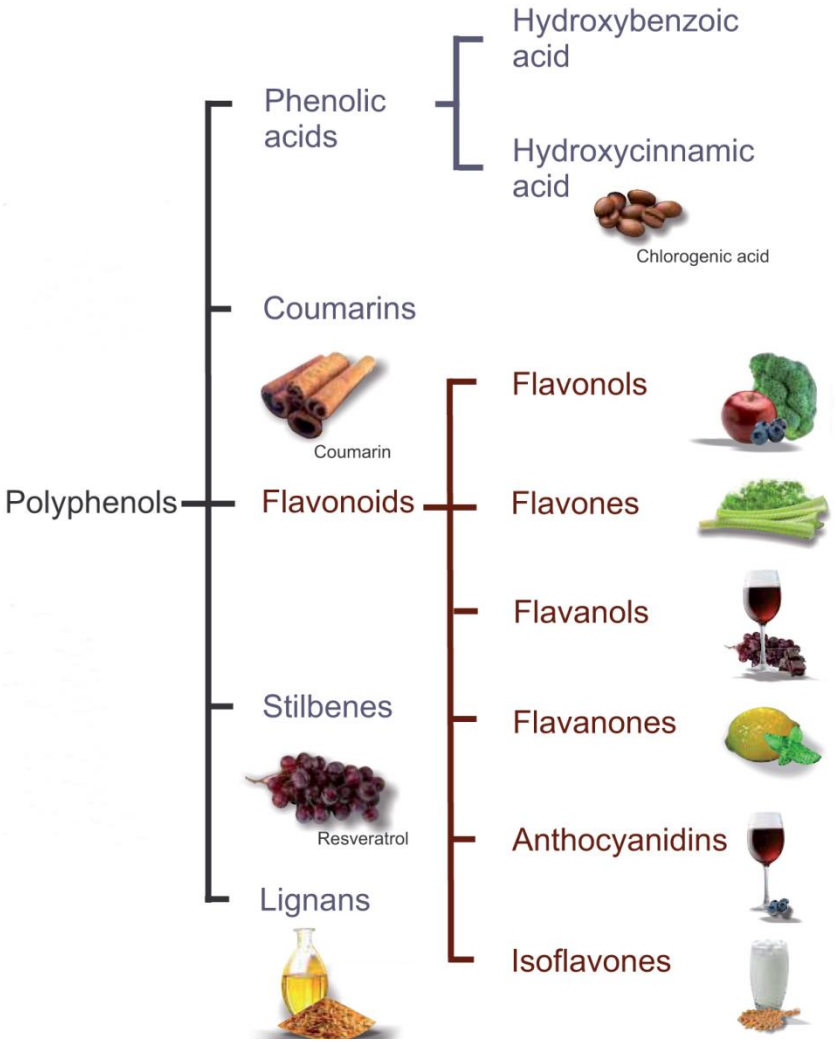

Figure 1.2. Classification of phenolic compounds (polyphenols) showing their possible food sources (adapted from reference 27).[27]

1.2.1. Biological Properties

Increasing recent studies have demonstrated the importance of dietary polyphenols in human health.[30-32] One important function of polyphenols is their antioxidant property. There is a positive correlation between the antioxidant properties of fruits and vegetables and their polyphenol content.[33-34] Many studies have shown that a rich polyphenol diet that contains high proportions of fruits and vegetables can lower the risk of chronic diseases, including

cancer, cardiovascular disease, chronic inflammation and degenerative diseases, some of which are correlated with oxidative stress caused by reactive oxygen species.[28] Recent studies have revealed the antioxidant properties of phenolic compounds that can neutralize reactive oxygen species (ROS), e.g. hydrogen peroxide (H_2O_2), superoxide anion (O_2^-), hydroxyl radical (•OH) and singlet oxygen.

Besides antioxidant properties, many of phenolic compounds have been found to play critical roles in the modulation of various cell signaling pathways in the human body.[35] Recent studies indicated several dietary phenolic compounds (e.g. quercetin, (-)-epigallocatechin (EGC), (-)-gallocatechin (GC) and (-)-epigallocatechin gallate (EGCG)) are involved in the prevention of inflammatory signaling pathways (e.g. nitric oxide, NFκB and mitogen-activated protein kinases (MaPK)).[35-36] For example, quercetin, in particular, has been found to downregulate the expression of pro-inflammatory cytokines (e.g. IL-1β, tNFα, IL-6 and IL-8) in activated human mast cell line by inactivating the NFκB pathway through prohibiting the IκBα degradation.[37] Moreover, increasing evidence demonstrate the role of phenolic compounds in the prevention of age-related cognitive decline,[38-39] while the potential for flavonoids in anti-obesity and diabetic prevention and therapy has also been suggested.[40-42]

1.2.2. Chemical Properties

The phenolic OH-group of phenolic compounds imparts an acidic property. The hydroxyl group on the benzene ring of a phenol is more acidic compared to the ones attached to unsubstituted aliphatic alcohols. From this regard, the phenolic compounds are generally weak acids. For example, phenol is a weak acid and has a modest p*K*a value (~10), which is between that of aliphatic alcohols (16-19) and that carboxylic acids (4-5), as shown in Figure 1.3.[43] Besides imparting acidity, the phenolic OH-group also renders phenolic compounds a potential candidate for hydrogen bonding. Due to the presence of abundant OH-groups, phenolic compounds can act as either a donor or a receptor of hydrogen bonding. They can form strong

hydrogen bonds with a great variety of biological and synthetic polymers containing multiply hydrogen-bond acceptors (e.g. poly(vinylpyrrolidone) (PVPON), poly(ethylene glycol) (PEG), antibiotics, protein and DNA).[44]

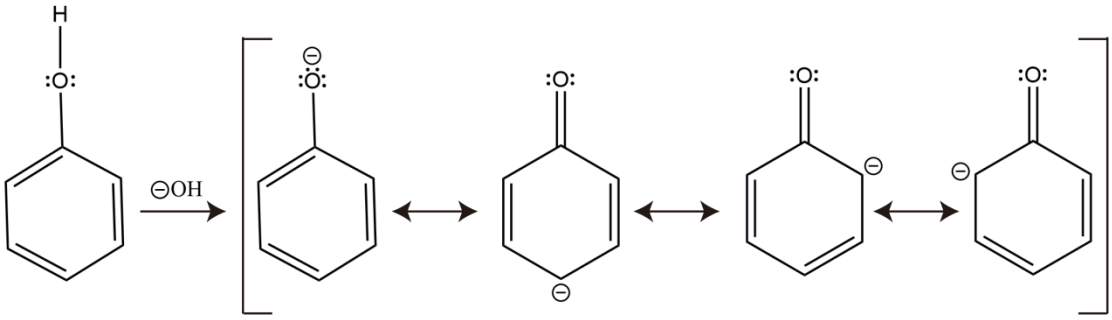

Figure 1.3. Acidity of phenol: generation of the phenoxide anion generated from phenol by the loss of the hydroxyl proton (adapted from reference 43).[43]

Another chemical property of phenolic compounds is that they are susceptible to oxidation due to their aromatic nature, which is a common problem in wine-making industries. The polyphenol is easily auto-oxidized when under the exposure of oxygen. In the presence of oxygen, phenolic compounds generate radicals, which react with each other to form a dimer, resulting in a series of different structures depending on the location of the radical electrons at different reaction time points. Figure 1.4 shows the possible pathways of catechol oxidation under oxygen, in which phenolic radicals react and form tetrahydroxy-biphenyls and quinines. Moreover, polyphenols can also serve as reducing agents under the presence of transition metal ions, where the polyphenol donate electrons and form quinones while the transition metal ions receive the electrons and are reduced into the metal nanoparticles.[45]

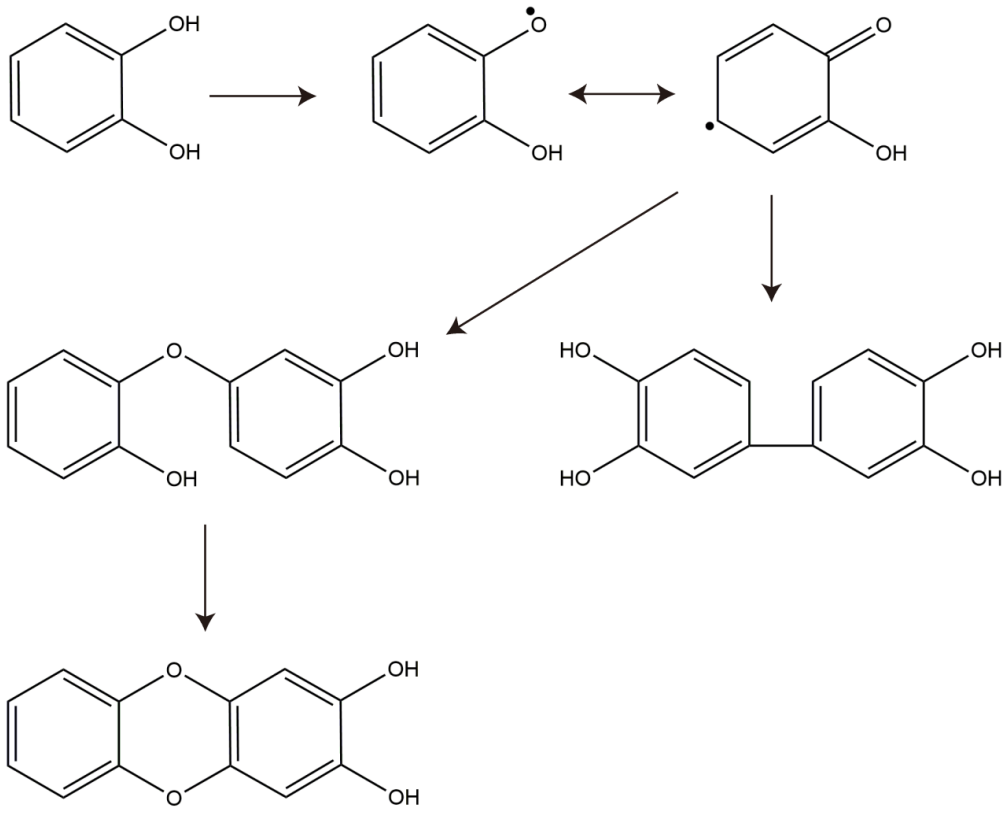

Figure 1.4. The pathways of catechol auto-oxidation with the formation of different dimers.

Another important chemical property of phenolic ligands involves the chelation with metal ions. The phenolic group could be deprotonated and have a high charge density that render the deprotonated phenolic group a potential ligand for metal chelation. In general, two or three adjacent hydroxyl groups (e.g. dihydroxyphenyl and trihydroxyphenyl) are much more favorable to coordinate with metal ions than one single hydroxyl group. Polyphenols can chelate with a great variety of metal ions, including iron (III), aluminium(III), manganese(II), gadolinium(III), cobalt(II), europium(III), nickel(II), copper(II) and zinc(II) etc., to form metal-phenolic coordination complexes.[44] A detailed description will be presented later in Chapter 1.5.

1.3. General Approaches for Engineering Hollow Nanostructures

A “hollow nanostructure” is defined as a solid nanostructure with empty space inside

it.[46] Hollow nanostructures, including capsules, are associated with some fascinating properties, such as low density, high loading capacity and large surface area. The development of approaches for the fabrication of hollow nanostructure is an active research area involving the engineering of multifunctional materials for diverse applications, including drug delivery, catalysis, energy (Li-ion batteries) and sensing. Since Caruso et al. reported the layer-by-layer (LbL) assembly method for fabricating inorganic nanoparticles-polymer hybrid hollow nanostructures in 1998[47], a great variety of templates have been developed to engineer hollow structures at the micro/nanoscale.[46] These methods can be mainly divided into two major categories based on the type of templates used: hard-templates and soft-templates method, as shown in Figure 1.5.

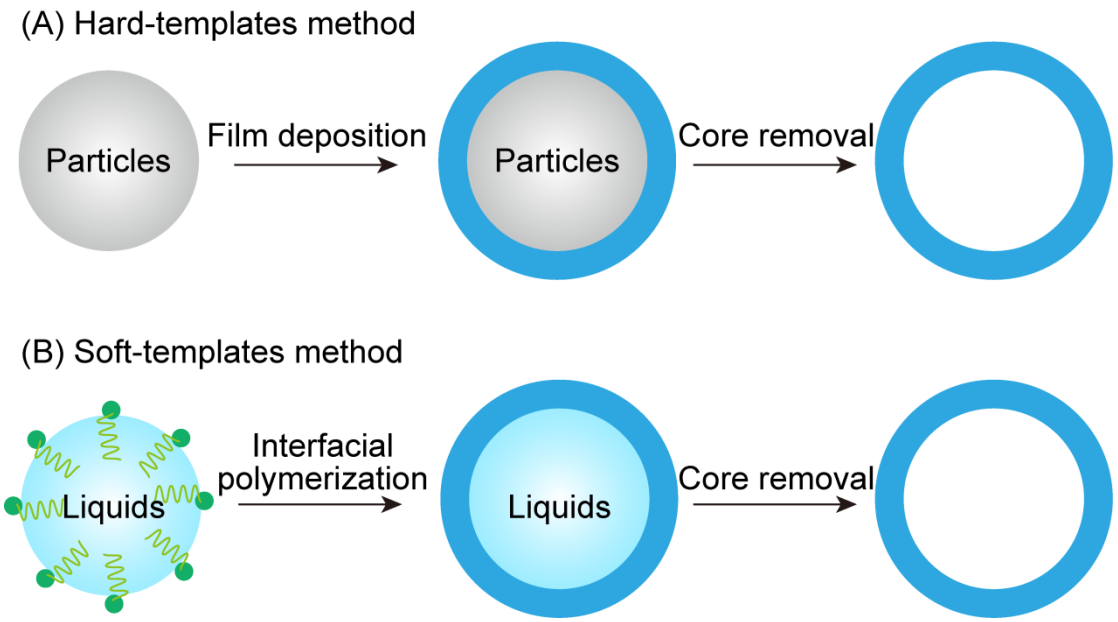

Figure 1.5. Schematic illustration showing the use of hard and soft templates for engineering hollow nanostructures. (A) Preparation of hollow nanostructures using hard templates; (B) Preparation of hollow nanostructures using soft templates.

1.3.1. Hard templates

In a typical hard template-based method, shell materials are deposited onto a pre-synthesized hard template (e.g. silica, polystyrene (PS), poly(methyl methacrylate)

(PMMA) and melamine formaldehyde (MF).[46, 48-49]) with a specific shape (e.g. sphere, rod, cubes, ellipsoids, and wires), followed by the selective removal of the core or templates, resulting in a hollow structure composed of the shell material, as shown in Figure. 1.5. As the shape of the resultant structures almost completely replicate that of the template used, the shape of nanostructures synthesized can be easily controlled by the shape of the template itself. Moreover, the properties of the shell (e.g. thickness, permeability, surface charge) can be tuned by the properties of the selected polymer or macromolecule and the parameters during the coating process.

1.3.1.1. Layer-by-layer (LbL) assembly

Layer-by-layer (LbL) assembly is one prevalent method for coating materials onto hard templates by sequentially depositing materials that have specific interactions with each other.[50-52] The concept of LbL assembly was first proposed in the mid-1960s.[53-54] R. K. Iler deposited colloidal particles onto glass by sequentially layering colloidal particles of alternating charges in 1966.[53] Recent years have witnessed the advance of layer-by-layer (LbL) assembly into fabricating hollow structures with varying properties (e.g. size, shape, morphology and surface charge) for many applications, such as biomedicine[55-57], drug delivery[58-60], catalysis[61], optics[62], separations[63], and energy.[64]

The deposition of LbL multilayer films onto a template surface can be achieved by various intermolecular interactions, including electrostatic interactions, hydrogen bonding, host-guest chemistry, surface sol-gel process, hydrophobic interactions, and biologically specific interactions.[52, 65-67] Figure 1.6 shows a general process of fabricating hollow structures (capsules) using hard templates based on the conventional LbL electrostatic interactions.[68] A template with a non-zero surface charge is immersed in a solution containing a polyelectrolyte with the opposite charge. After incubation for a certain time, the coated template is spun down and washed with water or buffer to remove unbounded polyelectrolyte, and then immersed in

the other solution containing a polyelectrolyte with the opposite charge. Sequential deposition of polyelectrolytes can allow tuning of film growth by alternating the adsorption of polyanions and polycations. Besides polyelectrolytes, a great variety of materials, including biomolecules (e.g. nucleic acids, protein, lipids, enzymes), nanoparticles and suprastructures can be used as constituents for film formulation.

To obtain hollow nanostructures, template removal is needed after film deposition. The removal can be achieved by etching the core according to the type of template used. For example, the removal of PS can be achieved by tetrahydrofuran (THF), while the etching of PMMA can be easily performed in *N*–methyl–2–pyrrolidone (NMP). In some cases, special precautions should be taken when dangerous solvents are used for etching templates (e.g., removing silica templates using hydrofluoric acid (HF)).[48, 69]

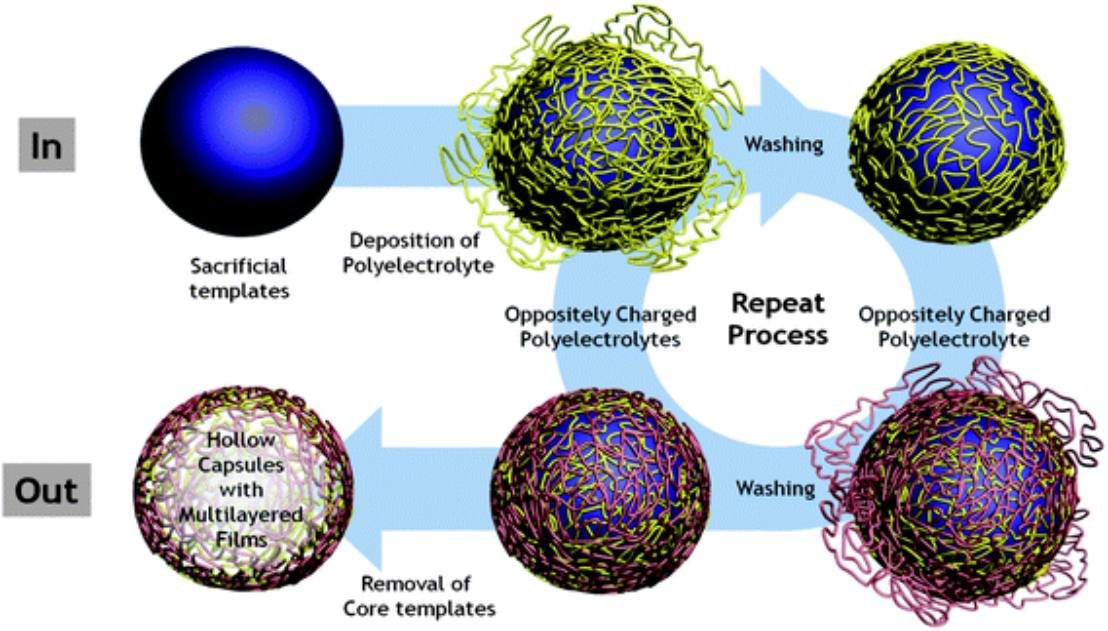

Figure 1.6. A scheme illustrating the preparation of hollow capsules consisting of polyelectrolyte multilayers by the layer-by-layer assembly on hard-templates (adapted from reference 68).[68]

1.3.1.2. Oxidative Self-Polymerization

Mussels have the capacity to adhere to almost all types of material surfaces, including

organic- and inorganic-based materials (Figure 1.7 a and b).[70] Recent studies have shown that this universal adherence of mussels likely results from the amino acid composition of proteins (mainly 3,4-dihydroxy-L-phenylalanine (DOPA) and lysine amino acids) at the tips of the byssus forming a plaque-substrate interface.[71-73] Inspired by this, Lee et al. reported a novel universal coating technique based on the oxidative self-polymerization of polydopamine (PDA), which is irrespective of template properties (e.g. size, morphologies, shape and surface charge), as shown in Figure 1.7 c.[74] So far, PDA coatings have been exploited in diverse applications and fields, including drug delivery, biomaterials, biosensors, interface chemistry, cell encapsulation, energy (Li-ion batteries) and biomineralization.[75-81]

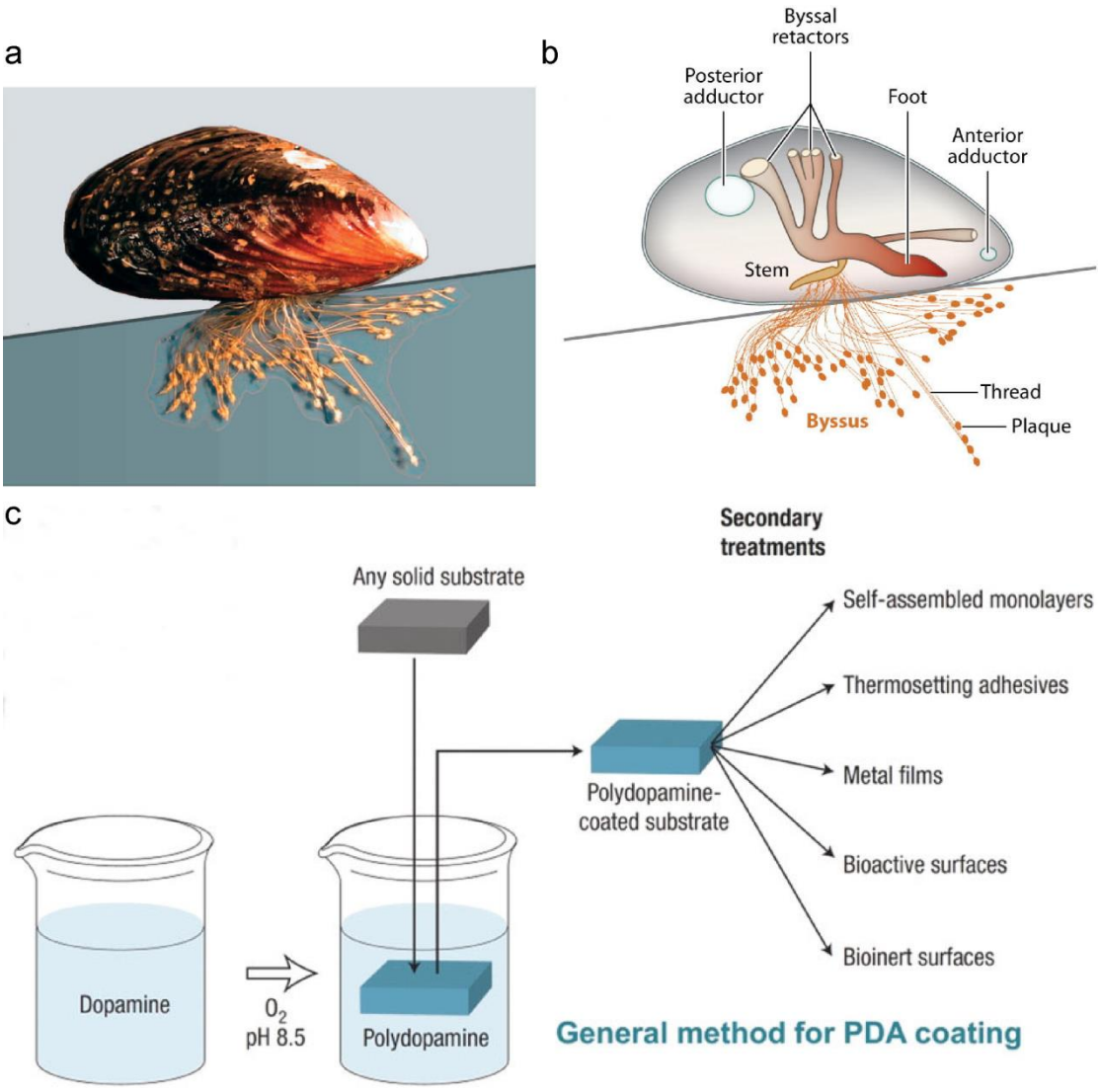

Figure 1.7. (a). The adherence of mussel to a mica surface by the byssus. (b) Schematic

illustration of the mussel structure.[82] (c). The self-polymerization of dopamine onto the substrates, results in the coating of polydopamine onto various surfaces. The polydopamine coating offers a great platform for secondary treatments for the preparation of functional materials for diverse applications.[83] Adapted from references 82, 83.

The application of PDA films in diverse fields has inspired significant research effort into the fundamental understanding of the PDA formulation pathways, although it is still controversial at the current stage. Figure 1.8 shows two possible mechanisms of PDA formation: the covalent oxidative pathway and the physical self-assembly pathway.[81] The former suggests that polydopamine formation undergoes the covalent oxidative pathway, which is similar to the melanin synthesis pathway.[83-85] In this pathway, dopamine is oxidized into 5,6-dihydroxyindole (DHI) that undergoes further oxidation and polymerization, and finally giving rise to PDA.[84-85] However, in a recent study, Dreyer et al. proposed that non-covalent self-assembly also plays a role in PDA formation in parallel with the covalent oxidative pathway.[86] In the non-covalent pathway, unpolymerized DA can complex with DHI, and forms (Dopamine)2/DHI trimers/ complexes. The non-covalent interactions in the complex that exist between DA and DHI (e.g. hydrogen bonding, cation–π, π–π, ionic, quadrupole–quadrupole interactions) drives the assembly of (Dopamine)2/DHI physical trimers and gives arise to PDA. Despite the above efforts, the mechanism of PDA remains elusive and requires further exploration in the future.

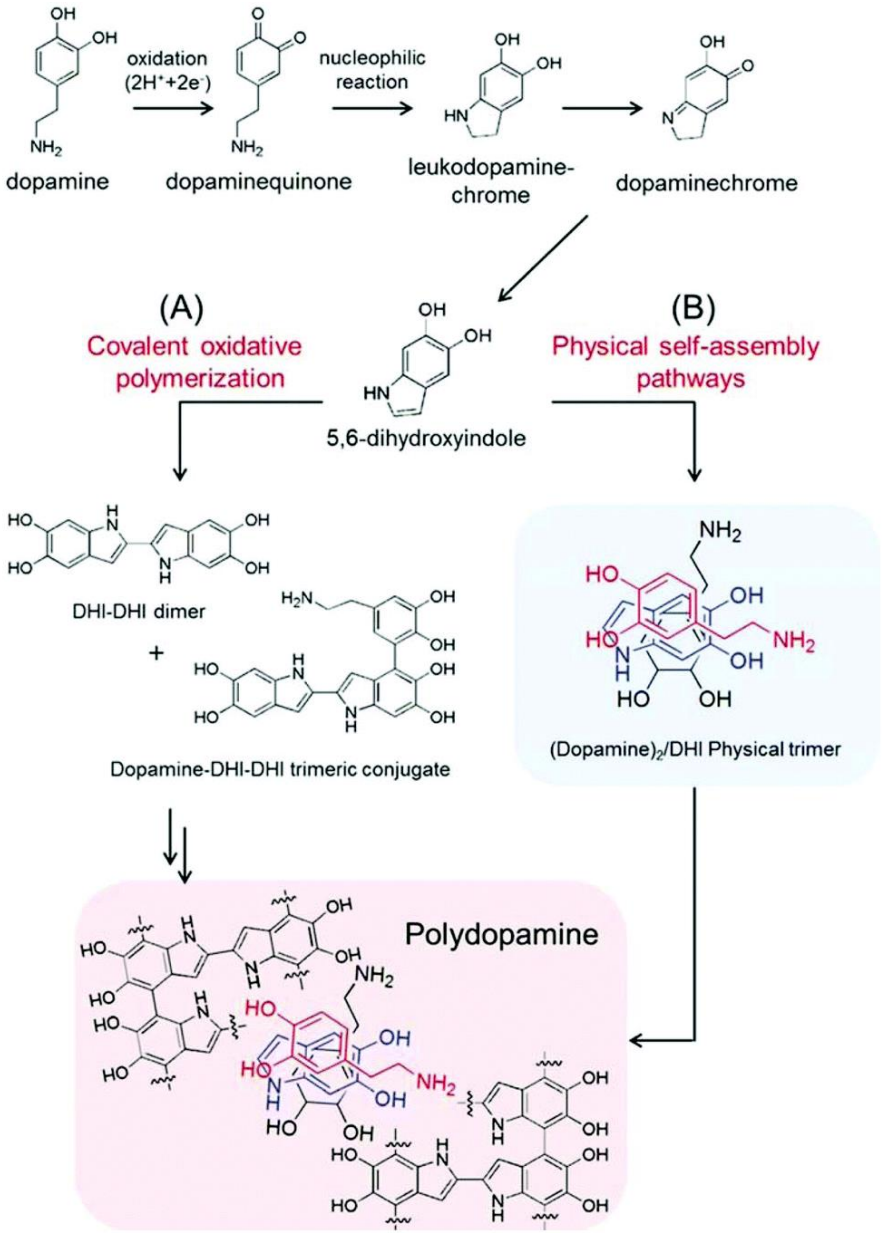

Figure 1.8. Schematic illustration of the two possible pathways of polydopamine formation: A) the covalent oxidative pathway that forms oxidative polymerization; B) the non-covalent self-assembly pathway based on the interaction between dopamine and 5,6-dihydroxyindole (DHI) (adapted from reference 86).[86]

There is also significant research effort in controlling DA polymerization and the properties of the resultant PDA. Numerous factors, including pH[87-89], concentration[90], oxidant[91], reaction time and temperature[92], have been found to influence the process of dopamine polymerization,

and thus could be employed to tune the properties (e.g. particles size and film thickness) of the resultant PDA. Besides DA, recent studies revealed that many plant-derived phenolic compounds (e.g. (Epigallocatechin gallate EGCG), pyrogallol (PG), and TA) have the capacity to undergo oxidative self-polymerization to form colorless polyphenol-inspired coatings on various substrates.[93] The low price and ubiquitous presence of polyphenol in nature plants render this polyphenol-inspired coatings a low-cost and green method for film formation and surface modification.

1.3.1.3. Other Methods for Film Fabrication

Besides LbL and oxidative self-polymerization, there are several other film deposition strategies, including Langmuir–Blodgett (LB) deposition, self-assembled monolayer (SAM), polymer brush, functionalized alkylsilanes (silanes) and continuous assembly of polymer (CAP). These established methods are still commonly used for surface modification in different fields.

1.3.2. Soft templates

The removal of hard templates usually requires specific conditions, including harsh solvents or high-temperature, that may cause deterioration of material integrity, especially when it comes to small sized (sub-100 nm) nanomaterials. To address this, a soft-template method offers an alternative way to fabricate hollow nanostructures. In this part, I will discuss the use of soft templates for engineering hollow nanostructures (e.g. polymer, metal oxides and silica-based nanomaterials). Soft templates can include emulsions, vesicles/micelles and gas bubbles.[46] This section is mainly focused on the emulsion templating method, as it is widely applied in the preparation of small-sized hollow nanostructures (below 100 nm).

Based on the size of emulsion droplets used as templates, the emulsion templating method can be divided into two classes: macroemulsions (droplet size>100 nm) and microemulsions

(droplet size <100 nm).[94] There are two major ways to prepare polymer-based hollow nanostructures using the emulsion as the templates: two-step method and one-step method. The two-step approach generally involves two separate procedures: polymerization in emulsion templates and the swelling of complexes. The surfactant (or micelles)-stabilized droplet serves as a nanoreactor containing the monomer (or precursor).[95-96] The addition of initiator triggers the polymerization in emulsion, resulting in the formation of polymer based particles. The resulting particles can be treated further to induce osmotic swelling of the complexes. For example, particles with a carboxylated core can result in hollow structures after incubation in basic solution, which causes the polymer complex to swell due to the ionization of the carboxylated core.[97] The size of the particles and the shell thickness can be tuned by controlling the process parameters, including surfactant and initiator concentration, reaction time, and the solution pH. So far, the two-step method has been applied for fabricating various polymer-based hollow nanostructures, including poly(styrene-butyl acrylate-methacrylic acid) (P(S-BA-MAA))[98], poly methyl methacrylate and ethylene glycol dimethacrylate (PMMA-EGDMA) and polystyrene nanoparticles.[99-100]

Unlike the two-step method, the one-step method is based on interfacial emulsion polymerization on the surface of the droplet. The general process of the one-step interfacial polymerization method is shown in Figure 1.5 b. Briefly, the monomer in the continuous phase polymerizes onto the emulsion droplet surface and forms a polymer layer when the initiator is added into the emulsion system. Hollow polymer nanostructures are obtained after removal of the emulsion core by evaporation or wash with some specific solvent. Gu and co-workers prepared polymer based hollow nanostructures using interfacial living/controlled (reversible addition-fragmentation chain transfer, RAFT) radical emulsion polymerization.[101] In this study, they synthesized a co-oligomer of styrene and maleic anhydride, which serves as a RAFT agent (SMA-RAFT). Their system consists of a mixture of water, ammonia, styrene,

SMA-RAFT agents and C_9H_{40}. The anhydride groups of SMA-RAFT agents were ammonolyzed into carboxyl and amide groups that turn the SMA-RAFT amphiphilic to allow anchoring at the oil/water interface and stabilize the dispersion. An injection of aqueous potassium persulfate (initiator) generates a radical in the water phase. Subsequently, the radical localizes with the amphiphilic SMA-RAFT agents on the surface of droplet, such that the RAFT polymerization was controlled at the interface. The interfacial polymerization resulted in a polymer shell where the polymer chains grew inwards as the reaction progressed. Sun et al. also developed a similar interfacial RAFT polymerization method to fabricate hollow polymer nanostructures with tunable size by copolymerization of methacrylic acid (MAA) and methyl methacrylate (MMA) in miniemulsions.[102] Moreover, Cui et al. recently employed the one-step interfacial polymerization method to prepare PDA films onto the surface of dimethyldiethoxysilane (DMDES) emulsion droplets.[103] The removal of the DMDES droplets resulted in PDA capsules with tunable sizes from 400 nm to 2.4 μm, with shell thickness controlled by modulating the concentration or condensation time of DMDES emulsion.

1.3.3. Self-Assembly

Self-assembly in nature in which disordered units assemble into an organized functional structures is key in the assembly of a variety of complex biological systems. This natural phenomenon has inspired the development of various synthetic self-assembly approaches for constructing multifunctional materials for diverse applications in numerous fields, including medicine, drug delivery, catalysis and sensing. Polymer self-assembly, which mainly involves noncovalent interaction instead of covalent bonding, has drawn increasing attention in the field of materials science, due to the reversible nature of noncovalent interactions.

Various types of molecules and compounds, including macrocycles, dendrimers, organic-inorganic complexes and other large macromolecules, such as macrocycles, dendrimers and protein, could be exploited as the starting precursor (building blocks) for

self-assembled polymeric structures.[104-108] The predominant driving forces for self-assembly are weak interactions, including van der Waals[109], hydrophobic interactions[110], hydrogen bonding[111], metal–organic coordination and host–guest interactions[112-114], which varies depending on the type of building blocks. The tunable nature of noncovalent interactions renders self-assembly a powerful approach to fabricate various nano/microstructures with different morphologies, including spheres, ellipsoids, rods, rings, cubes and cylinders.[115-118] Meanwhile, the reversibility of the noncovalent interactions impart the self-assembled nano/microstructures with stimuli-responsiveness properties[119-122], which induce chemical and/or physical variation of nano/microstructures when receiving the stimulus from the surrounding environment (e.g., pH, redox gradients, enzymes and temperature) or external forces (light, magnetic field, ultrasound or electric pulses).[123-124] These features render self-assembly as a power tool for making various nano/microstructures for different applications, such as drug and gene delivery, imaging, sensors, reactors and organelles mimicking, intelligent machines and devices.[125-129]

1.4. Metal-Organic Coordination Polymer

Recently, metal-organic coordination polymer, which involves the repeating unit of metal-organic compounds extending in 1, 2, or 3 dimensions, has attracted extensive attention in various field.[130] The metal-organic coordination polymer can be divided into two major classes: porous crystalline metal-organic coordination polymer and amorphous infinite coordination polymer.[131-133] Unlike traditional polymer based materials, the metal-organic coordination polymers consists of metal ions as building blocks and thus exhibits some intrinsic and unique advantages in optical, electronic, magnetic, catalytic and biological properties, which is greatly associated with the metal component.[134-138]

1.4.1. Porous Crystalline Coordination Polymer

Porous coordination polymers (PCPs or metal-organic frameworks (MOFs) are a subclass of coordination polymers that are composed of metal ions or clusters and organic ligands bridging to form 1, 2, and 3 dimensional structures.[139] In general, coordination bonds spread over the whole MOFs in 1, 2 and 3 dimensions.[139] Non-covalent interactions, including π–π stacking, hydrophobic effect and hydrogen bonds, facilitate the linkages between the building units (1D, 2D, 3D frameworks). MOFs generally possess a porous and crystalline structure. As MOFs are usually synthesized by hydro/solvothermal technique, in which the slow formation rate results in a highly ordered structures. This allows MOFs to be easily characterized by the powder X-ray/neutron/synchrotron diffraction studies to give structure information, which provides guidance to the design of MOFs materials.

MOFs have the following advantages, including ease of synthesis, good thermal stability, highly ordered structure, and large internal surface area (>6000 m^2/g). Moreover, the combination of different organic ligands with inorganic building blocks has led to thousands of MOFs being synthesized and studied that offers an immense flexibility on tuning the associated MOFs properties (e.g. dimension, morphologies, structure, pore size and surface chemistry), as shown in Figure 1.9.[140] MOFs have great potential in diverse application in various fields, including nanomedicine, drug delivery, catalysis, gas storage and separations.[141-145]

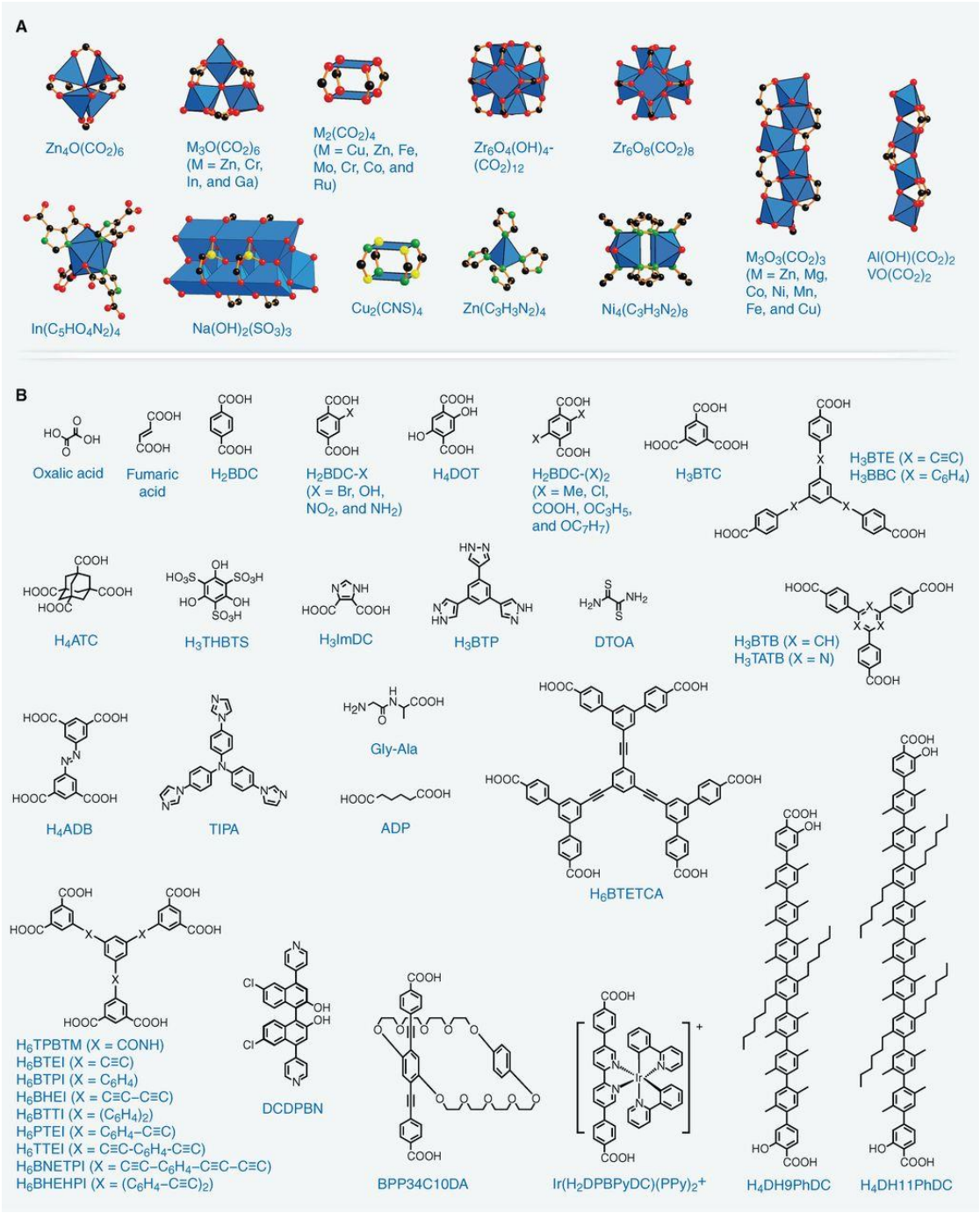

Figure 1.9. Some commonly used inorganic secondary building units (A) and organic ligands for the preparation of MOFs (adapted from reference 140).[140]

1.4.2. Amorphous Infinite Metal-Organic Coordination Polymer

Besides MOFs, there is another type of coordination polymer—infinite coordination polymer (ICP), that is also formed by the coordination between metal ions and organic

ligand.[146] Unlike MOFs which are synthesized by hydro/solvothermal method, ICPs are generally formed by solvent-induced precipitation，where the precursor in one solvent diffuses into another solvent that contains particle precursors.[147] The formation rate is usually too great to organize the building blocks into an ordered crystalline state. Therefore, ICP materials are usually amorphous such that it is difficult to employ an X-ray diffraction technique to study the process of ICPs formation and the structure of resultant ICP materials. ICPs possess a great variety of properties that are different from the crystalline MOFs. For example, the amorphous property of ICPs means they disassemble much more rapidly upon the introduction of the competitive binding agents to the metal nodes (e.g. solvent or ligand) than crystalline MOFs. This makes ICP-based materials suitable for drug delivery. Moreover, ICPs exhibit great structural tailorability (e.g. size and morphologies) through the combination of metal ions and organic ligand (Figure 1.10), a high thermal stability and are easily dispersed in a wide variety of solvents, all of which render ICPs a good platform for various applications, including imaging, drug delivery, sensing and catalysis.[148-151]

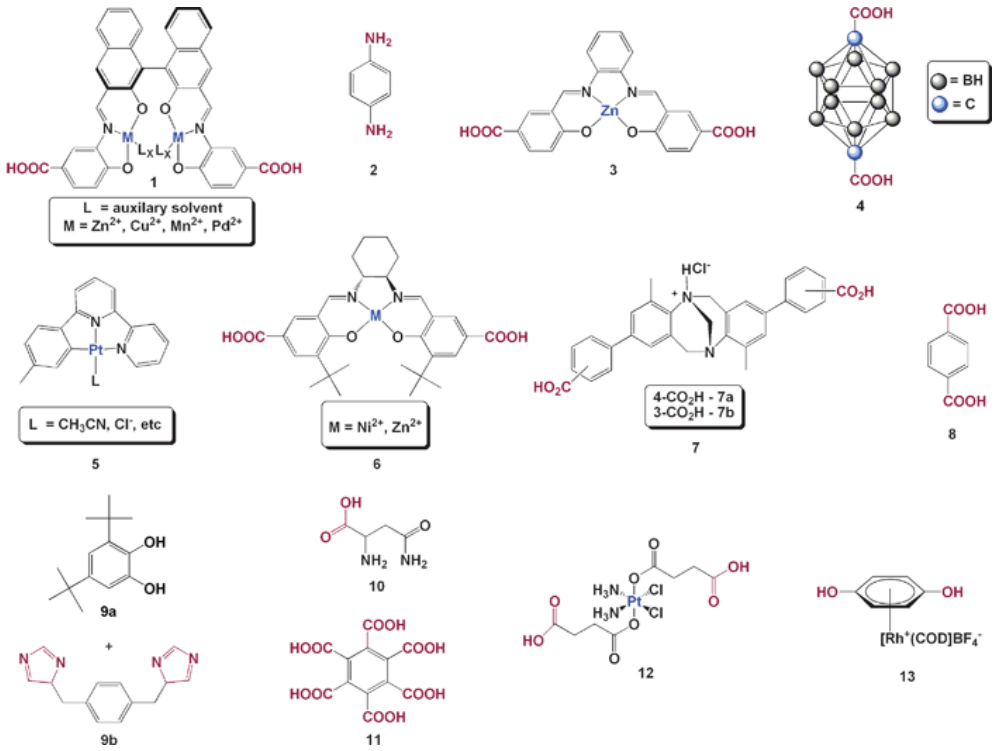

Figure 1.10. Some representative organic ligands employed in the synthesis of infinite coordination polymer (reproduced from reference 147).[147]

1.5. Metal-Phenolic Networks (MPNs)

MOFs and ICPs generally need the specific interaction between metal ions and organic ligands, the number of their combination is generally limited. Recent studies have shown that polyphenols can chelate with a variety of metal ions. Recently, the group of Caruso reported a novel universal platform to engineer hybrid films using metal-phenolic complexes formed by the coordination between metal ions and phenolic ligands that is applicable to a wide range of substrates (e.g. glass, Au, iron oxide and PDMS).[16] Multifunctional capsules and free-standing films can be obtained after the substrate removal. The general applicability of MPNs has been demonstrated by further studies using a variety of different metals and polyphenol ligands.[19]

1.5.1. Metal-Phenolic Films

In 2013, Ejima et al. reported the formation of MPN films on various substrates using tannic

acid (TA; a natural polyphenol) and iron(III) (Figure 1.11 a), which is independent of surface properties (Figure 1.11 b, c, d, e, f, g, h).[16] Due to the ubiquitous occurrence of TA in nature, hence its low cost, MPN film formulation is cheap and easy for large scale assembly. To follow this study, Caruso and co-workers established a library of metal ions (Figure 1.11 i, j) to fabricate a series of functional MPN capsules[19], as polyphenol (TA) is able to chelate different metal ions. Different metals can be selected to impart the resulting MPN capsules with different functionalities. For example, MPN capsules made from radioactive $^{64}Cu^{II}$ can serve as a positron emission tomography (PET) imaging probe for tracking particle biodistribution in vivo. The paramagnetic metals (Fe^{III}, Mn^{II}, and Gd^{III}) could endow the MPN capsules with the ability of MRI contrast enhancements. Hybrid multi-metal (Cu^{II} and Eu^{III}) containing MPN capsules can act as probes for multimodal imaging (PET and fluorescence imaging), which can accomplish high resolution and sensitivity simultaneously within one single capsule. Besides functionalities, the degradability of MPNs can be also tuned by the choice of metal ions.

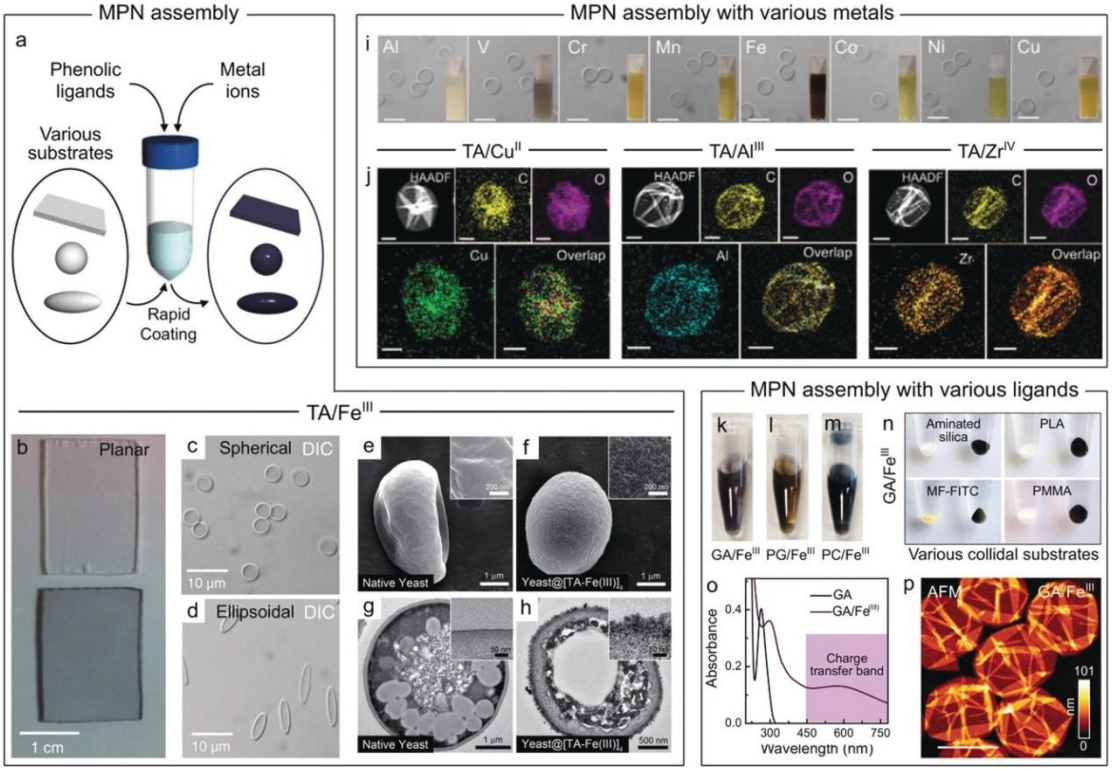

Figure 1.11. (a) Scheme illustrating the MPN assembly: TA/Fe^{III} films assembled on various

substrates: b) planar, c) spherical, d) ellipsoidal, and e–h) yeast cells (SEM). MPN assembly with different metal ions: i) capsules from the MPN assembly using TA and different metals ions (Al^{III}, V^{III}, Cr^{III}, Mn^{II}, Fe^{III}, Co^{II}, Ni^{II}, and Cu^{II}); j) high-angle annular dark-field TEM spectra and elemental mapping of the MPN capsules containing Cu^{II}, Al^{III} and Zr^{IV}. (k–p) MPN assembly using small phenolic ligands: photographs showing the sample containing the capsule of GA/Fe^{III} (k), PG/Fe^{III} (l), and PC/Fe^{III} (m), and the coating of GA/Fe^{III} onto different colloidal substrates, including silica, PLA, MF and PMMA (n); o) the UV-vis absorption spectra of free GA and GA/Fe^{III} capsule sample; p) atomic force microscopy image of GA/Fe^{III} capsules in dried state (adapted from reference 152).[152]

Besides TA, many other phenolic compounds, including simple phenolic compounds, and polyphenol, have been investigated to expand the phenolic ligand library (Figure 1.11 k, l, m, n, o, p). In a recent study, Rahim et al. investigated the feasibility of simple phenolic molecules (e.g. gallic acid (GA), PG and pyrocatechol (PC)) as phenolic building blocks for MPNs capsules. They found at least one vicinal diol group was required for MPN films formulation.[17] Moreover, many dietary natural flavonoids with diverse biological activities, such as fisetin (Fis), luteolin (Lut), Myricetin (Myr) and quercetin (Que), have been used as phenolic building blocks for MPN film formation.[18] This makes MPN assembly a promising technique in pharmaceutical and food industries, due to the potential health benefits of flavonoids (e.g. anti-tumor, anti- antioxidants, anti-inflammation and anti-bacterial, etc.).

Synthetic polyphenols, including catechol-polymer conjugates can also be applied as building blocks for the preparation of multifunctional MPNs capsules. Polyethylene glycol (PEG) is a Food and Drug Administration (FDA) approved polymer, which offers the “stealth” effect that could prevent plasma opsonization and uptake by macrophages.[153-155] Recently, Ju et al. synthesized catechol-functionalized PEG-based MPN capsules that exhibited low fouling

properties and thus a reduced nonspecific protein adsorption and cell association, compared with conventional TA-Fe MPNs capsules.[156] In addition, these PEG-based MPNs capsules showed a faster and more desirable disassembly behavior in pH 5 than TA/Fe^{III} based MPNs capsules (80% in 5 h vs 30% in 10 days), demonstrating their potential for controlled drug delivery. The introduction of phenol groups (e.g. catechol, galloyl) to the synthetic polymer combined with targeting ability could be used to imparting active targeting properties on the MPN capsules. In a recent study, MPN capsules made of catechol functionalized with hyaluronic acid (HA) demonstrated enhanced cell association towards MDA-MB-231 cancer cells which overexpressed the receptor for HA (CD44). Such enhancement in cell association can be tuned by adjusting the ratio of HA to PEG in the polymer-phenol conjugate precursor.[157]

The MPN film coating can also be applied in fabricating core-shell nanoparticles. Due to the versatility of MPN coating, various types of micro/nanoparticles, including red blood cells[158], phagocytic enzyme myeloperoxidase[159], polymer based-nanoparticles (e.g, poly(lactic-co-glycolic acid)-based polymeric nanospheres and nanovesicles)[160], MOFs[161], mesoporous silica[162], and BaGdF5 nanoparticles[163], have been coated with MPN films to modify their surfaces. The MPN coating can impart the nanoparticles with specific functionalities which depend on the metal ions used. For example, europium (Eu) endows the nanoparticles the capacity for magnetic resonance (MR), computed tomography (CT) and luminescence imaging. Paramagnetic elements (Fe^{III}, Mn^{II} and Gd^{III}) provide T_1, T_2-weighted dual-modal MR contrast enhancement. The MPN coating also confers pH-sensitive properties that can be exploited for the release of loaded cargo within MPN films in acidic environment (e.g., tumor). All of these features render MPN film assembly a powerful technique for the preparation or surface modification of nanoparticles in nanomedicine, imaging and drug delivery.[152, 164]

1.5.2. Metal-Phenolic Particles

The self-assembly driven by the coordination between phenolic compounds and metal ions has led to the formulation of nano/microparticles for various applications. Since Fe^{III} is highly biocompatible and ubiquitous in in biological systems[165-167], it has been the most commonly used metal ion for the formulation of metal-phenolic particles. The coordination complexes of phenolic compounds, including TA and gallic acid (GA), have been employed to fabricate MPN nanoparticles.[168-169] These nanoparticles shows great functionalities in nanomedicine, including MRI, photoacoustic imaging and photothermal therapy, due to their strong absorbance in the NIR region. The metal-phenolic particles (GA/Fe^{III}) could further encapsulate an anticancer drug (e.g. doxorubicin) with high efficacy (~48.3%) by the coordination interaction between Fe^{III} in metal-phenolic particles and the deprotonated hydroxyl groups of DOX.[170] A synthetic polymer (e.g poly(vinylpyrrolidone) (PVP)) with multiple metal chelating sites can help stabilize the metal-phenolic coordination particle and result in ultra-small (~ 5 nm) metal-phenolic nanoparticles that facilitate renal clearance.[171-172] Moreover, the possible metal chelating sites on phenolic compounds and/or polymer can be further used to label the particles with metal nuclide (^{64}Cu isotope) for in vivo PET imaging to monitor the biodistribution of particles in real-time.[173]

Polymer-polyphenol conjugates can also be used as phenolic building blocks for fabricating self-assembled nanoparticles via metal-phenolic coordination. A typical example is a recent study by Caruso and co-workers, which involves assembly of PEG-polyphenol and platinum (Pt)-polyphenol with metal ion into nanoparticles (PtP NPs) via an emulsification technique (Figure 1.12 a).[174] The PEG ligand endowed the PtP NPs with “stealth” properties and thus a long circulation time ($h_{1/2}\approx18$ h) in the blood of healthy mice (Figure 1.12 b), resulting in an enhanced tumor accumulation and better tumor growth inhibition than free platinum (Pt)-polyphenol and cisplatin (Figure 1.12 c).

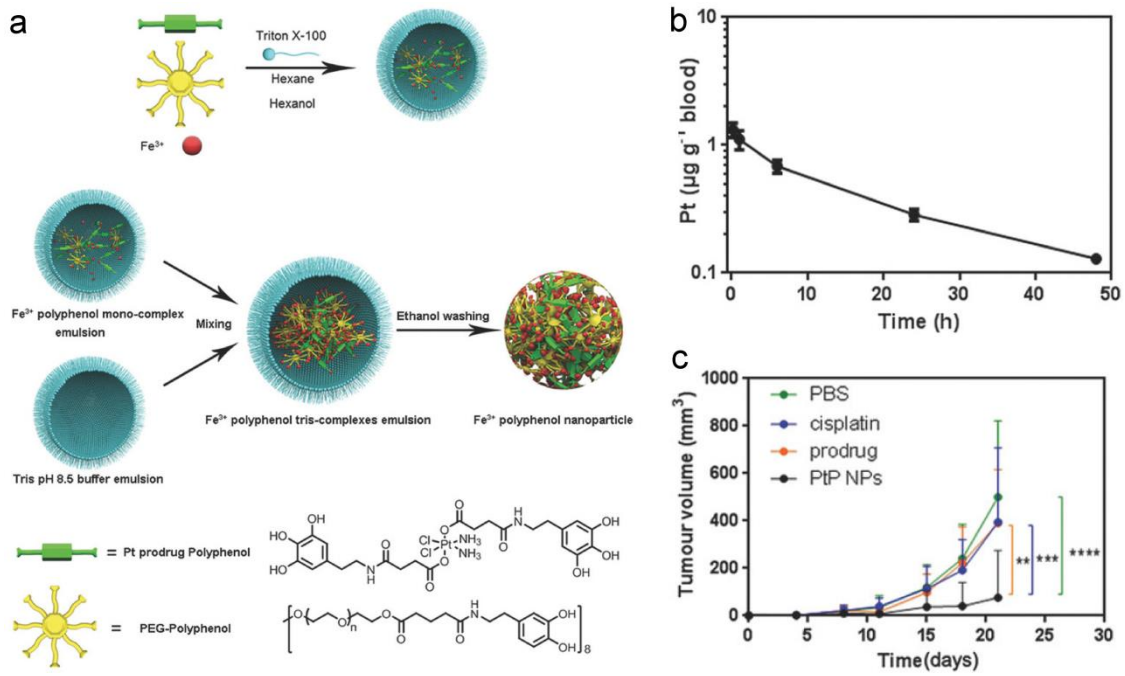

Figure 1.12. (a) Scheme illustrating the process of PtP NP self-assembly. (b) Pharmacokinetics profile of PtP NPs in healthy mice through intravenously injection. (c) Tumor growth curves of PC3 tumor expressing luciferase after the treatment of PBS, cisplatin, platinum (Pt)-polyphenol and PtP NPs at the same Pt dose (adapted from reference 174).[174]

1.6. Limitation and Challenges in MPNs

MPNs formation has demonstrated a versatile and powerful approach to engineer multifunctional films and particles for diverse applications in many fields. However, the bulk of the literature on metal-phenolic materials has been focused on the assembly on hard templates (e.g. MSN, gold, calcium carbonate, polystyrene, polymethyl methacrylate (PMMA) and etc.) using a single ligand (e.g. TA, GA, flavonoids and polymer-polyphenol conjugates). Due to the ubiquitous existence of polyphenols in nature, natural sources such as plant extracts can provide a variety of phenolic compounds that could potentially be used as phenolic building blocks for metal-phenolic assembly, which there have been limited studies on in the past. Regarding assembly techniques, the use of traditional hard templates has several limitations and disadvantages. For example, it usually requires centrifugation to remove the

free and unbound polymer or complexes, which may cause undesirable particle aggregation, especially when the size of templates are in the nanoscale. Moreover, conditions (e.g. solvent, temperature) used to dissolve the template to obtain a hollow structure or capsule, may influence the material integrity of the final capsule. Thus, to advance this field, there is a need to investigate the versatility of the metal-phenolic assembly system in terms of different phenolic ligands and assembly techniques to broaden the toolbox for metal-phenolic assembly, which could result in novel multifunctional materials with unique properties.

1.7. Scope of Thesis

This thesis explores different assembly techniques, from hard to soft templates, and to template-free self-assembly, to create a series of multifunctional metal-phenolic materials, including thin films, nanoparticles and crystals. A variety of instruments and techniques were employed for the characterization of these materials and building blocks. An overview of instrument and underlying principles along with experimental set-up is presented in Chapter 2.

Beyond the conventional metal-phenolic assembly using a single ligand, metal-phenolic assembly in a natural extract containing a multicomponent mixture of phenolic compounds was explored in Chapter 3. Metal–phenolic coordination-driven self-assembly exhibits selective properties in a series of complex multicomponent systems (including crude plant extracts), in which the metal (Fe^{III}) selectively assembles with low abundant phenolic components (e.g., myricetrin and quercetrin) into thin films. This selective metal–phenolic assembly is independent of the substrate properties (e.g., size, surface charge, and shape) and the resultant metal-phenolic films demonstrate great antioxidant potential.

To address the drawbacks in the use of hard template, I transitioned from using traditional hard templates to soft templates (microemulsions) in Chapter 4. A series of pH-sensitive poly(ethylene glycol) small sized nanoparticles (20-50 nm) with tunable sizes and

morphologies could be synthesized by adjusting the metal-phenolic crosslinking in the microemulsions. The variations in size and morphology observed likely resulted from the changing amphiphilicity of PEG-gallol/Mn^{II} complexes at different metal-to-phenol ratios. These tunable poly(ethylene glycol) nanoparticles are pH-sensitive, non-cytotoxic in cell culture and have low fouling properties, demonstrating their potential in drug delivery.

Chapter 5 reports the self-assembly of monodispersed metal-phenolic crystals formed from the coordination between metal ions (zinc) and ellagic acid— a natural phenolic acid found in many fruits and vegetables. These metal-phenolic crystals show a positive “phototaxis” property, meaning they can sense light and orient towards the illumination source with a velocity tuned by the light intensity. A detailed mechanism study was performed by nuclear magnetic resonance (NMR), confocal Raman microscopy and quantum mechanics calculations, and provided insight into the light-induced movement of the metal-phenolic particles.

1.8. References

(1) Römer, L.; Scheibel, T. The elaborate structure of spider silk: Structure and function of a natural high performance fiber. *Prion* **2008,** *2* (4), 154-161, DOI: 10.4161/pri.2.4.7490.

(2) Tokareva, O.; Jacobsen, M.; Buehler, M.; Wong, J.; Kaplan, D. L. Structure-function-property-design interplay in biopolymers: spider silk. *Acta Biomater* **2014,** *10* (4), 1612-1626, DOI: 10.1016/j.actbio.2013.08.020.

(3) Scheibel, T. Spider silks: Recombinant synthesis, assembly, spinning, and engineering of synthetic proteins. *Microbial Cell Factories* **2004,** *3* (1), 14, DOI: 10.1186/1475-2859-3-14.

(4) Waite, J. H.; Qin, X.-X.; Coyne, K. J. The peculiar collagens of mussel byssus. *Matrix Biology* **1998,** *17* (2), 93-106, DOI: https://doi.org/10.1016/S0945-053X(98)90023-3.

(5) Waite, J. H. The formation of mussel byssus: Anatomy of a natural manufacturing process. In *Structure, Cellular Synthesis and Assembly of Biopolymers*; Case, S. T., Ed.; Springer Berlin Heidelberg: Berlin, Heidelberg, 1992; pp 27-54.

(6) Waite, J. H. Mussel adhesion – essential footwork. *The Journal of Experimental Biology* **2017,** *220* (4), 517, DOI: 10.1242/jeb.134056.

(7) Cheng, Y. T.; Rodak, D. E.; Wong, C. A.; Hayden, C. A. Effects of micro- and nano-structures on the self-cleaning behaviour of lotus leaves. *Nanotechnology* **2006,** *17* (5), 1359-1362, DOI: 10.1088/0957-4484/17/5/032.

(8) Ganesh, V. A.; Raut, H. K.; Nair, A. S.; Ramakrishna, S. A review on self-cleaning coatings. *Journal of Materials Chemistry* **2011,** *21* (41), 16304-16322, DOI: 10.1039/C1JM12523K.

(9) Watson, G. S.; Gellender, M.; Watson, J. A. Self-propulsion of dew drops on lotus leaves: A potential mechanism for self cleaning. *Biofouling* **2014,** *30* (4), 427-434, DOI: 10.1080/08927014.2014.880885.

(10) Lee, B. P.; Messersmith, P. B.; Israelachvili, J. N.; Waite, J. H. Mussel-inspired adhesives and coatings. *Annu Rev Mater Res* **2011,** *41*, 99-132, DOI:

10.1146/annurev-matsci-062910-100429.

(11) Yang, H.; Liang, F.; Chen, Y.; Wang, Q.; Qu, X.; Yang, Z. Lotus leaf inspired robust superhydrophobic coating from strawberry-like Janus particles. *NPG Asia Materials* **2015,** *7* (4), e176-e176, DOI: 10.1038/am.2015.33.

(12) Koeppel, A.; Holland, C. Progress and trends in artificial silk spinning: A systematic review. *ACS Biomaterials Science & Engineering* **2017,** *3* (3), 226-237, DOI: 10.1021/acsbiomaterials.6b00669.

(13) Krogsgaard, M.; Behrens, M. A.; Pedersen, J. S.; Birkedal, H. Self-healing mussel-inspired multi-pH-responsive hydrogels. *Biomacromolecules* **2013,** *14* (2), 297-301, DOI: 10.1021/bm301844u.

(14) Li, L.; Smitthipong, W.; Zeng, H. Mussel-inspired hydrogels for biomedical and environmental applications. *Polymer Chemistry* **2015,** *6* (3), 353-358, DOI: 10.1039/C4PY01415D.

(15) Krogsgaard, M.; Nue, V.; Birkedal, H. Mussel-inspired materials: self-healing through coordination chemistry. *Chemistry – A European Journal* **2016,** *22* (3), 844-857, DOI: 10.1002/chem.201503380.

(16) Ejima, H.; Richardson, J. J.; Liang, K.; Best, J. P.; van Koeverden, M. P.; Such, G. K.; Cui, J.; Caruso, F. One-step assembly of coordination complexes for versatile film and particle engineering. *Science* **2013,** *341* (6142), 154, DOI: 10.1126/science.1237265.

(17) Rahim, M. A.; Kempe, K.; Müllner, M.; Ejima, H.; Ju, Y.; van Koeverden, M. P.; Suma, T.; Braunger, J. A.; Leeming, M. G.; Abrahams, B. F.; Caruso, F. Surface-confined amorphous films from metal-coordinated simple phenolic ligands. *Chemistry of Materials* **2015,** *27* (16), 5825-5832, DOI: 10.1021/acs.chemmater.5b02790.

(18) Bertleff-Zieschang, N.; Rahim, M. A.; Ju, Y.; Braunger, J. A.; Suma, T.; Dai, Y.; Pan, S.; Cavalieri, F.; Caruso, F. Biofunctional metal–phenolic films from dietary flavonoids. *Chemical*

Communications **2017,** *53* (6), 1068-1071, DOI: 10.1039/C6CC08607A.

(19) Guo, J.; Ping, Y.; Ejima, H.; Alt, K.; Meissner, M.; Richardson, J. J.; Yan, Y.; Peter, K.; von Elverfeldt, D.; Hagemeyer, C. E.; Caruso, F. Engineering multifunctional capsules through the assembly of metal–phenolic networks. *Angewandte Chemie International Edition* **2014,** *53* (22), 5546-5551, DOI: 10.1002/anie.201311136.

(20) Rahim, M. A.; Ejima, H.; Cho, K. L.; Kempe, K.; Müllner, M.; Best, J. P.; Caruso, F. Coordination-driven multistep assembly of metal–polyphenol films and capsules. *Chemistry of Materials* **2014,** *26* (4), 1645-1653, DOI: 10.1021/cm403903m.

(21) Yun, G.; Besford, Q. A.; Johnston, S. T.; Richardson, J. J.; Pan, S.; Biviano, M.; Caruso, F. Self-assembly of nano- to macroscopic metal–phenolic materials. *Chemistry of Materials* **2018,** *30* (16), 5750-5758, DOI: 10.1021/acs.chemmater.8b02616.

(22) Ju, Y.; Cui, J.; Sun, H.; Müllner, M.; Dai, Y.; Guo, J.; Bertleff-Zieschang, N.; Suma, T.; Richardson, J. J.; Caruso, F. Engineered metal-phenolic capsules show tunable targeted delivery to cancer cells. *Biomacromolecules* **2016,** *17* (6), 2268-2276, DOI: 10.1021/acs.biomac.6b00537.

(23) Besford, Q. A.; Ju, Y.; Wang, T.-Y.; Yun, G.; Cherepanov, P.; Hagemeyer, C. E.; Cavalieri, F.; Caruso, F. Self-assembled metal–phenolic networks on emulsions as low-fouling and pH-responsive particles. *Small* **2018,** *14* (39), 1802342, DOI: 10.1002/smll.201802342.

(24) Jianbo Xiao, G. K. A review of dietary polyphenol-plasma protein interactions: Characterization, influence on the bioactivity, and structure-affinity relationship. *Critical reviews in food science and nutrition* **2012,** *52* (1), 85-101.

(25) Manach, C.; Scalbert, A.; Morand, C.; Rémésy, C.; Jiménez, L. Polyphenols: Food sources and bioavailability. *The American Journal of Clinical Nutrition* **2004,** *79* (5), 727-747, DOI: 10.1093/ajcn/79.5.727.

(26) Quideau, S.; Deffieux, D.; Douat-Casassus, C.; Pouységu, L. Plant polyphenols: Chemical

properties, biological activities, and synthesis. *Angewandte Chemie International Edition* **2011,** *50* (3), 586-621, DOI: 10.1002/anie.201000044.

(27) Bondonno, C. P.; Croft, K. D.; Ward, N.; Considine, M. J.; Hodgson, J. M. Dietary flavonoids and nitrate: effects on nitric oxide and vascular function. *Nutrition Reviews* **2015,** *73* (4), 216-235, DOI: 10.1093/nutrit/nuu014.

(28) Kumar, S.; Pandey, A. K. Chemistry and biological activities of flavonoids: An overview. *The Scientific World Journal* **2013,** *2013*, 16, DOI: 10.1155/2013/162750.

(29) Nijveldt, R. J.; van Nood, E.; van Hoorn, D. E. C.; Boelens, P. G.; van Norren, K.; van Leeuwen, P. A. M. Flavonoids: a review of probable mechanisms of action and potential applications. *The American Journal of Clinical Nutrition* **2001,** *74* (4), 418-425, DOI: 10.1093/ajcn/74.4.418.

(30) Khan, N.; Mukhtar, H. Tea polyphenols for health promotion. *Life Sciences* **2007,** *81* (7), 519-533, DOI: https://doi.org/10.1016/j.lfs.2007.06.011.

(31) Del Rio, D.; Costa, L. G.; Lean, M. E. J.; Crozier, A. Polyphenols and health: What compounds are involved? *Nutrition, Metabolism and Cardiovascular Diseases* **2010,** *20* (1), 1-6, DOI: https://doi.org/10.1016/j.numecd.2009.05.015.

(32) Fraga, C. G.; Galleano, M.; Verstraeten, S. V.; Oteiza, P. I. Basic biochemical mechanisms behind the health benefits of polyphenols. *Molecular Aspects of Medicine* **2010,** *31* (6), 435-445, DOI: https://doi.org/10.1016/j.mam.2010.09.006.

(33) Someya, S.; Yoshiki, Y.; Okubo, K. Antioxidant compounds from bananas (Musa Cavendish). *Food Chemistry* **2002,** *79* (3), 351-354, DOI: https://doi.org/10.1016/S0308-8146(02)00186-3.

(34) Sarawong, C.; Schoenlechner, R.; Sekiguchi, K.; Berghofer, E.; Ng, P. K. W. Effect of extrusion cooking on the physicochemical properties, resistant starch, phenolic content and antioxidant capacities of green banana flour. *Food Chemistry* **2014,** *143*, 33-39, DOI:

https://doi.org/10.1016/j.foodchem.2013.07.081.

(35) Rasouli, H.; Farzaei, M. H.; Khodarahmi, R. Polyphenols and their benefits: A review. *International Journal of Food Properties* **2017,** *20* (sup2), 1700-1741, DOI: 10.1080/10942912.2017.1354017.

(36) Chen, L.; Teng, H.; Jia, Z.; Battino, M.; Miron, A.; Yu, Z.; Cao, H.; Xiao, J. Intracellular signaling pathways of inflammation modulated by dietary flavonoids: The most recent evidence. *Critical Reviews in Food Science and Nutrition* **2018,** *58* (17), 2908-2924, DOI: 10.1080/10408398.2017.1345853.

(37) Comalada, M.; Camuesco, D.; Sierra, S.; Ballester, I.; Xaus, J.; Gálvez, J.; Zarzuelo, A. In vivo quercitrin anti-inflammatory effect involves release of quercetin, which inhibits inflammation through down-regulation of the NF-κB pathway. *European Journal of Immunology* **2005,** *35* (2), 584-592, DOI: 10.1002/eji.200425778.

(38) Gildawie, K. R.; Galli, R. L.; Shukitt-Hale, B.; Carey, A. N. Protective effects of foods containing flavonoids on age-related cognitive decline. *Current Nutrition Reports* **2018,** *7* (2), 39-48, DOI: 10.1007/s13668-018-0227-0.

(39) Queen, B. L.; Tollefsbol, T. O. Polyphenols and aging. *Curr Aging Sci* **2010,** *3* (1), 34-42.

(40) Zhao, Y.; Chen, B.; Shen, J.; Wan, L.; Zhu, Y.; Yi, T.; Xiao, Z. The beneficial effects of quercetin, curcumin, and resveratrol in obesity. *Oxid Med Cell Longev* **2017,** *2017*, 1459497-1459497, DOI: 10.1155/2017/1459497.

(41) Chen, S.; Jiang, H.; Wu, X.; Fang, J. Therapeutic effects of quercetin on inflammation, obesity, and type 2 diabetes. *Mediators of Inflammation* **2016,** *2016*, 5, DOI: 10.1155/2016/9340637.

(42) Zhao, L.; Zhang, Q.; Ma, W.; Tian, F.; Shen, H.; Zhou, M. A combination of quercetin and resveratrol reduces obesity in high-fat diet-fed rats by modulation of gut microbiota. *Food & Function* **2017,** *8* (12), 4644-4656, DOI: 10.1039/C7FO01383C.

(43) Vermerris, W.; Nicholson, R. Chemical properties of phenolic compounds. *Phenolic Compound Biochemistry*; Vermerris, W.; Nicholson, R., Eds.; Springer Netherlands: Dordrecht, 2006; pp 35-62.

(44) Xu, L. Q.; Neoh, K.-G.; Kang, E.-T. Natural polyphenols as versatile platforms for material engineering and surface functionalization. *Progress in Polymer Science* **2018,** *87*, 165-196, DOI: https://doi.org/10.1016/j.progpolymsci.2018.08.005.

(45) Ahmad, T. Reviewing the tannic acid mediated synthesis of metal nanoparticles. *Journal of Nanotechnology* **2014,** *2014*, 11, DOI: 10.1155/2014/954206.

(46) Wang, X.; Feng, J.; Bai, Y.; Zhang, Q.; Yin, Y. Synthesis, properties, and applications of hollow micro-/nanostructures. *Chemical Reviews* **2016,** *116* (18), 10983-11060, DOI: 10.1021/acs.chemrev.5b00731.

(47) Caruso, F.; Caruso, R. A.; Möhwald, H. Nanoengineering of inorganic and hybrid hollow spheres by colloidal templating. *Science* **1998,** *282* (5391), 1111, DOI: 10.1126/science.282.5391.1111.

(48) Wang, Y.; Angelatos, A. S.; Caruso, F. Template synthesis of nanostructured materials via layer-by-layer assembly. *Chemistry of Materials* **2008,** *20* (3), 848-858, DOI: 10.1021/cm7024813.

(49) Bentz, K. C.; Savin, D. A. Hollow polymer nanocapsules: synthesis, properties, and applications. *Polymer Chemistry* **2018,** *9* (16), 2059-2081, DOI: 10.1039/C8PY00142A.

(50) Richardson, J. J.; Björnmalm, M.; Caruso, F. Technology-driven layer-by-layer assembly of nanofilms. *Science* **2015,** *348* (6233), aaa2491, DOI: 10.1126/science.aaa2491.

(51) Richardson, J. J.; Cui, J.; Björnmalm, M.; Braunger, J. A.; Ejima, H.; Caruso, F. Innovation in layer-by-layer assembly. *Chemical Reviews* **2016,** *116* (23), 14828-14867, DOI: 10.1021/acs.chemrev.6b00627.

(52) Zhang, X.; Chen, H.; Zhang, H. Layer-by-layer assembly: from conventional to

unconventional methods. *Chemical Communications* **2007,** (14), 1395-1405, DOI: 10.1039/B615590A.

(53) Iler, R. K. Multilayers of colloidal particles. *Journal of Colloid and Interface Science* **1966,** *21* (6), 569-594, DOI: https://doi.org/10.1016/0095-8522(66)90018-3.

(54) Kirkland, J. J. Porous thin-layer modified glass bead supports for gas liquid chromatography. *Analytical Chemistry* **1965,** *37* (12), 1458-1461, DOI: 10.1021/ac60231a004.

(55) Boudou, T.; Crouzier, T.; Ren, K.; Blin, G.; Picart, C. Multiple functionalities of polyelectrolyte multilayer films: new biomedical applications. *Advanced Materials* **2010,** *22* (4), 441-467, DOI: 10.1002/adma.200901327.

(56) Costa, R. R.; Mano, J. F. Polyelectrolyte multilayered assemblies in biomedical technologies. *Chemical Society Reviews* **2014,** *43* (10), 3453-3479, DOI: 10.1039/C3CS60393H.

(57) Yan, Y.; Such, G. K.; Johnston, A. P. R.; Lomas, H.; Caruso, F. Toward therapeutic delivery with layer-by-layer engineered particles. *ACS Nano* **2011,** *5* (6), 4252-4257, DOI: 10.1021/nn201793f.

(58) Correa, S.; Dreaden, E. C.; Gu, L.; Hammond, P. T. Engineering nanolayered particles for modular drug delivery. *Journal of Controlled Release* **2016,** *240*, 364-386, DOI: https://doi.org/10.1016/j.jconrel.2016.01.040.

(59) De Koker, S.; Hoogenboom, R.; De Geest, B. G. Polymeric multilayer capsules for drug delivery. *Chemical Society Reviews* **2012,** *41* (7), 2867-2884, DOI: 10.1039/C2CS15296G.

(60) Delcea, M.; Möhwald, H.; Skirtach, A. G. Stimuli-responsive LbL capsules and nanoshells for drug delivery. *Advanced Drug Delivery Reviews* **2011,** *63* (9), 730-747, DOI: https://doi.org/10.1016/j.addr.2011.03.010.

(61) Xiao, M.; Wang, Z.; Lyu, M.; Luo, B.; Wang, S.; Liu, G.; Cheng, H.-M.; Wang, L. Hollow nanostructures for photocatalysis: Advantages and challenges. *Advanced Materials* **2019,** *31*

(38), 1801369, DOI: 10.1002/adma.201801369.

(62) Facchetti, A.; Abbotto, A.; Beverina, L.; van der Boom, M. E.; Dutta, P.; Evmenenko, G.; Pagani, G. A.; Marks, T. J. Layer-by-layer self-assembled pyrrole-based donor−acceptor chromophores as electro-optic materials. *Chemistry of Materials* **2003,** *15* (5), 1064-1072, DOI: 10.1021/cm020929d.

(63) Joseph, N.; Ahmadiannamini, P.; Hoogenboom, R.; Vankelecom, I. F. J. Layer-by-layer preparation of polyelectrolyte multilayer membranes for separation. *Polymer Chemistry* **2014,** *5* (6), 1817-1831, DOI: 10.1039/C3PY01262J.

(64) Hamedi, M.; Karabulut, E.; Marais, A.; Herland, A.; Nyström, G.; Wågberg, L. Nanocellulose aerogels functionalized by rapid layer-by-layer assembly for high charge storage and beyond. *Angewandte Chemie International Edition* **2013,** *52* (46), 12038-12042, DOI: 10.1002/anie.201305137.

(65) Borges, J.; Mano, J. F. Molecular interactions driving the layer-by-layer assembly of multilayers. *Chemical Reviews* **2014,** *114* (18), 8883-8942, DOI: 10.1021/cr400531v.

(66) Fu, J.; Schlenoff, J. B. Driving forces for oppositely charged polyion association in aqueous solutions: Enthalpic, entropic, but not electrostatic. *Journal of the American Chemical Society* **2016,** *138* (3), 980-990, DOI: 10.1021/jacs.5b11878.

(67) Matsusaki, M.; Ajiro, H.; Kida, T.; Serizawa, T.; Akashi, M. Layer-by-layer assembly through weak interactions and their biomedical applications. *Advanced Materials* **2012,** *24* (4), 454-474, DOI: 10.1002/adma.201103698.

(68) Hong, J.; Han, J. Y.; Yoon, H.; Joo, P.; Lee, T.; Seo, E.; Char, K.; Kim, B.-S. Carbon-based layer-by-layer nanostructures: from films to hollow capsules. *Nanoscale* **2011,** *3* (11), 4515-4531, DOI: 10.1039/C1NR10575B.

(69) Knotter, D. M. Etching mechanism of vitreous silicon dioxide in HF-based solutions. *Journal of the American Chemical Society* **2000,** *122* (18), 4345-4351, DOI:

10.1021/ja993803z.

(70) Waite, J. H.; Andersen, N. H.; Jewhurst, S.; Sun, C. Mussel adhesion: finding the tricks worth mimicking. *The Journal of Adhesion* **2005,** *81* (3-4), 297-317, DOI: 10.1080/00218460590944602.

(71) Lee, H.; Scherer, N. F.; Messersmith, P. B. Single-molecule mechanics of mussel adhesion. *Proc Natl Acad Sci U S A* **2006,** *103* (35), 12999-13003, DOI: 10.1073/pnas.0605552103.

(72) Waite, J. H.; Qin, X. Polyphosphoprotein from the adhesive pads of mytilus edulis. *Biochemistry* **2001,** *40* (9), 2887-2893, DOI: 10.1021/bi002718x.

(73) Wei, W.; Yu, J.; Broomell, C.; Israelachvili, J. N.; Waite, J. H. Hydrophobic enhancement of dopa-mediated adhesion in a mussel foot protein. *Journal of the American Chemical Society* **2013,** *135* (1), 377-383, DOI: 10.1021/ja309590f.

(74) Lee, H.; Dellatore, S. M.; Miller, W. M.; Messersmith, P. B. Mussel-inspired surface chemistry for multifunctional coatings. *Science* **2007,** *318* (5849), 426, DOI: 10.1126/science.1147241.

(75) Lynge, M. E.; van der Westen, R.; Postma, A.; Städler, B. Polydopamine—a nature-inspired polymer coating for biomedical science. *Nanoscale* **2011,** *3* (12), 4916-4928, DOI: 10.1039/C1NR10969C.

(76) Ku, S. H.; Lee, J. S.; Park, C. B. Spatial control of cell adhesion and patterning through mussel-inspired surface modification by polydopamine. *Langmuir* **2010,** *26* (19), 15104-15108, DOI: 10.1021/la102825p.

(77) Yang, S. H.; Kang, S. M.; Lee, K.-B.; Chung, T. D.; Lee, H.; Choi, I. S. Mussel-inspired encapsulation and functionalization of individual yeast cells. *Journal of the American Chemical Society* **2011,** *133* (9), 2795-2797, DOI: 10.1021/ja1100189.

(78) Ryou, M.-H.; Lee, Y. M.; Park, J.-K.; Choi, J. W. Mussel-inspired polydopamine-treated polyethylene separators for high-power Li-ion batteries. *Advanced Materials* **2011,** *23* (27),

3066-3070, DOI: 10.1002/adma.201100303.

(79) Ryu, J.; Ku, S. H.; Lee, H.; Park, C. B. Mussel-inspired polydopamine coating as a universal route to hydroxyapatite crystallization. *Advanced Functional Materials* **2010,** *20* (13), 2132-2139, DOI: 10.1002/adfm.200902347.

(80) Postma, A.; Yan, Y.; Wang, Y.; Zelikin, A. N.; Tjipto, E.; Caruso, F. Self-polymerization of dopamine as a versatile and robust technique to prepare polymer capsules. *Chemistry of Materials* **2009,** *21* (14), 3042-3044, DOI: 10.1021/cm901293e.

(81) Batul, R.; Tamanna, T.; Khaliq, A.; Yu, A. Recent progress in the biomedical applications of polydopamine nanostructures. *Biomaterials Science* **2017,** *5* (7), 1204-1229, DOI: 10.1039/C7BM00187H.

(82) Lee, B. P.; Messersmith, P. B.; Israelachvili, J. N.; Waite, J. H. Mussel-inspired adhesives and coatings. *Annu Rev Mater Res* **2011,** *41* (1), 99-132, DOI: 10.1146/annurev-matsci-062910-100429.

(83) Waite, J. H. Mussel power. *Nature Materials* **2008,** *7* (1), 8-9, DOI: 10.1038/nmat2087.

(84) Panzella, L.; Pezzella, A.; Napolitano, A.; d'Ischia, M. The first 5,6-dihydroxyindole tetramer by oxidation of 5,5‘,6,6‘-tetrahydroxy-2,4‘-biindolyl and an unexpected issue of positional reactivity en route to eumelanin-related polymers. *Organic Letters* **2007,** *9* (7), 1411-1414, DOI: 10.1021/ol070268w.

(85) Adhyaru, B. B.; Akhmedov, N. G.; Katritzky, A. R.; Bowers, C. R. Solid-state cross-polarization magic angle spinning ^{13}C and ^{15}N NMR characterization of Sepia melanin, Sepia melanin free acid and Human hair melanin in comparison with several model compounds. *Magnetic Resonance in Chemistry* **2003,** *41* (6), 466-474, DOI: 10.1002/mrc.1193.

(86) Hong, S.; Na, Y. S.; Choi, S.; Song, I. T.; Kim, W. Y.; Lee, H. Non-covalent self-assembly and covalent polymerization co-contribute to polydopamine formation. *Advanced Functional*

Materials **2012,** *22* (22), 4711-4717, DOI: 10.1002/adfm.201201156.

(87) Ho, C.-C.; Ding, S.-J. The pH-controlled nanoparticles size of polydopamine for anti-cancer drug delivery. *Journal of Materials Science: Materials in Medicine* **2013,** *24* (10), 2381-2390, DOI: 10.1007/s10856-013-4994-2.

(88) Zheng, W.; Fan, H.; Wang, L.; Jin, Z. Oxidative self-polymerization of dopamine in an acidic environment. *Langmuir* **2015,** *31* (42), 11671-11677, DOI: 10.1021/acs.langmuir.5b02757.

(89) Della Vecchia, N. F.; Luchini, A.; Napolitano, A.; D'Errico, G.; Vitiello, G.; Szekely, N.; d'Ischia, M.; Paduano, L. Tris buffer modulates polydopamine growth, aggregation, and paramagnetic properties. *Langmuir* **2014,** *30* (32), 9811-9818, DOI: 10.1021/la501560z.

(90) Della Vecchia, N. F.; Avolio, R.; Alfè, M.; Errico, M. E.; Napolitano, A.; d'Ischia, M. Building-block diversity in polydopamine underpins a multifunctional eumelanin-type platform tunable through a quinone control point. *Advanced Functional Materials* **2013,** *23* (10), 1331-1340, DOI: 10.1002/adfm.201202127.

(91) Wei, Q.; Zhang, F.; Li, J.; Li, B.; Zhao, C. Oxidant-induced dopamine polymerization for multifunctional coatings. *Polymer Chemistry* **2010,** *1* (9), 1430-1433, DOI: 10.1039/C0PY00215A.

(92) Jiang, J.; Zhu, L.; Zhu, L.; Zhu, B.; Xu, Y. Surface characteristics of a self-polymerized dopamine coating deposited on hydrophobic polymer films. *Langmuir* **2011,** *27* (23), 14180-14187, DOI: 10.1021/la202877k.

(93) Sileika, T. S.; Barrett, D. G.; Zhang, R.; Lau, K. H. A.; Messersmith, P. B. Colorless multifunctional coatings inspired by polyphenols found in tea, chocolate, and wine. *Angewandte Chemie International Edition* **2013,** *52* (41), 10766-10770, DOI: 10.1002/anie.201304922.

(94) Serrano-Luginbühl, S.; Ruiz-Mirazo, K.; Ostaszewski, R.; Gallou, F.; Walde, P. Soft and

dispersed interface-rich aqueous systems that promote and guide chemical reactions. *Nature Reviews Chemistry* **2018,** *2* (10), 306-327, DOI: 10.1038/s41570-018-0042-6.

(95) Harkins, W. D. A general theory of the mechanism of emulsion polymerization[1]. *Journal of the American Chemical Society* **1947,** *69* (6), 1428-1444, DOI: 10.1021/ja01198a053.

(96) Harkins, W. D. General theory of mechanism of emulsion polymerization. II. *Journal of Polymer Science* **1950,** *5* (2), 217-251, DOI: 10.1002/pol.1950.120050208.

(97) McDonald, C. J.; Bouck, K. J.; Chaput, A. B.; Stevens, C. J. Emulsion polymerization of voided particles by encapsulation of a nonsolvent. *Macromolecules* **2000,** *33* (5), 1593-1605, DOI: 10.1021/ma991284e.

(98) Okubo, M.; Ichikawa, K.; Fujimura, M. Production of multi-hollow polymer microspheres by stepwise alkali/acid method II. Alkali treatment process. *Colloid and Polymer Science* **1991,** *269* (12), 1257-1262, DOI: 10.1007/BF00652534.

(99) Omi, S.; Ma, G.-H.; Nagai, M. Membrane emulsification a versatile tool for the synthesis of polymeric microspheres. *Macromolecular Symposia* **2000,** *151* (1), 319-330, DOI: 10.1002/1521-3900(200002)151:1<319::AID-MASY319>3.0.CO;2-X.

(100) Ma, G.-H.; Omi, S.; Dimonie, V. L.; Sudol, E. D.; El-Aasser, M. S. Study of the preparation and mechanism of formation of hollow monodisperse polystyrene microspheres by SPG (Shirasu Porous Glass) emulsification technique. *Journal of Applied Polymer Science* **2002,** *85* (7), 1530-1543, DOI: 10.1002/app.10785.

(101) Luo, Y.; Gu, H. A general strategy for nano-encapsulation via interfacially confined living/controlled radical miniemulsion polymerization. *Macromolecular Rapid Communications* **2006,** *27* (1), 21-25, DOI: 10.1002/marc.200500649.

(102) Sun, Z.; Luo, Y. Fabrication of non-collapsed hollow polymeric nanoparticles with shell thickness in the order of ten nanometres and anti-reflection coatings. *Soft Matter* **2011,** *7* (3), 871-875, DOI: 10.1039/C0SM00983K.

(103) Cui, J.; Wang, Y.; Postma, A.; Hao, J.; Hosta-Rigau, L.; Caruso, F. Monodisperse polymer capsules: tailoring Size, shell thickness, and hydrophobic cargo loading via emulsion templating. *Advanced Functional Materials* **2010,** *20* (10), 1625-1631, DOI: 10.1002/adfm.201000209.

(104) Whitesides, G. M.; Grzybowski, B. Self-assembly at all scales. *Science* **2002,** *295* (5564), 2418, DOI: 10.1126/science.1070821.

(105) Sánchez-Iglesias, A.; Grzelczak, M.; Altantzis, T.; Goris, B.; Pérez-Juste, J.; Bals, S.; Van Tendeloo, G.; Donaldson, S. H.; Chmelka, B. F.; Israelachvili, J. N.; Liz-Marzán, L. M. Hydrophobic interactions modulate self-assembly of nanoparticles. *ACS Nano* **2012,** *6* (12), 11059-11065, DOI: 10.1021/nn3047605.

(106) Hormoz, S.; Brenner, M. P. Design principles for self-assembly with short-range interactions. *Proceedings of the National Academy of Sciences* **2011,** *108* (13), 5193, DOI: 10.1073/pnas.1014094108.

(107) Claessens, C. G.; Stoddart, J. F. π–π interactions in self-assembly. *Journal of Physical Organic Chemistry* **1997,** *10* (5), 254-272, DOI: 10.1002/(SICI)1099-1395(199705)10:5<254::AID-POC875>3.0.CO;2-3.

(108) Huang, F.; O'Reilly, R.; Zimmerman, S. C. Polymer self-assembly: a web themed issue. *Chemical Communications* **2014,** *50* (88), 13415-13416, DOI: 10.1039/C4CC90367F.

(109) Wu, Z.; Liu, J.; Li, Y.; Cheng, Z.; Li, T.; Zhang, H.; Lu, Z.; Yang, B. Self-assembly of nanoclusters into mono-, few-, and multilayered sheets via dipole-induced asymmetric van der waals attraction. *ACS Nano* **2015,** *9* (6), 6315-6323, DOI: 10.1021/acsnano.5b01823.

(110) Gao, W.; Pei, A.; Feng, X.; Hennessy, C.; Wang, J. Organized self-assembly of Janus micromotors with hydrophobic hemispheres. *Journal of the American Chemical Society* **2013,** *135* (3), 998-1001, DOI: 10.1021/ja311455k.

(111) Corradi, E.; Meille, S. V.; Messina, M. T.; Metrangolo, P.; Resnati, G. Halogen bonding

versus hydrogen bonding in driving self-assembly processes. *Angewandte Chemie International Edition* **2000,** *39* (10), 1782-1786, DOI: 10.1002/(SICI)1521-3773(20000515)39:10<1782::AID-ANIE1782>3.0.CO;2-5.

(112) Dai, F.; Dou, J.; He, H.; Zhao, X.; Sun, D. Self-assembly of metal−organic supramolecules: from a metallamacrocycle and a metal−organic coordination cage to 1D or 2D coordination polymers based on flexible dicarboxylate ligands. *Inorganic Chemistry* **2010,** *49* (9), 4117-4124, DOI: 10.1021/ic902178c.

(113) Wei, P.; Yan, X.; Huang, F. Supramolecular polymers constructed by orthogonal self-assembly based on host–guest and metal–ligand interactions. *Chemical Society Reviews* **2015,** *44* (3), 815-832, DOI: 10.1039/C4CS00327F.

(114) Yebeutchou, R. M.; Tancini, F.; Demitri, N.; Geremia, S.; Mendichi, R.; Dalcanale, E. Host–guest driven self-assembly of linear and star supramolecular polymers. *Angewandte Chemie International Edition* **2008,** *47* (24), 4504-4508, DOI: 10.1002/anie.200801002.

(115) Klinger, D.; Wang, C. X.; Connal, L. A.; Audus, D. J.; Jang, S. G.; Kraemer, S.; Killops, K. L.; Fredrickson, G. H.; Kramer, E. J.; Hawker, C. J. A facile synthesis of dynamic, shape-changing polymer particles. *Angewandte Chemie International Edition* **2014,** *53* (27), 7018-7022, DOI: 10.1002/anie.201400183.

(116) Wang, X.; Gao, P.; Yang, Y.; Guo, H.; Wu, D. Dynamic and programmable morphology and size evolution via a living hierarchical self-assembly strategy. *Nature Communications* **2018,** *9* (1), 2772, DOI: 10.1038/s41467-018-05142-3.

(117) Li, L.; Raghupathi, K.; Song, C.; Prasad, P.; Thayumanavan, S. Self-assembly of random copolymers. *Chemical Communications* **2014,** *50* (88), 13417-13432, DOI: 10.1039/C4CC03688C.

(118) Bucknall, D. G.; Anderson, H. L. Polymers get organized. *Science* **2003,** *302* (5652), 1904, DOI: 10.1126/science.1091064.

(119) Stuart, M. A. C.; Huck, W. T. S.; Genzer, J.; Müller, M.; Ober, C.; Stamm, M.; Sukhorukov, G. B.; Szleifer, I.; Tsukruk, V. V.; Urban, M.; Winnik, F.; Zauscher, S.; Luzinov, I.; Minko, S. Emerging applications of stimuli-responsive polymer materials. *Nature Materials* **2010,** *9* (2), 101-113, DOI: 10.1038/nmat2614.

(120) Wang, Y.; Shim, M. S.; Levinson, N. S.; Sung, H.-W.; Xia, Y. Stimuli-responsive materials for controlled release of theranostic agents. *Advanced Functional Materials* **2014,** *24* (27), 4206-4220, DOI: 10.1002/adfm.201400279.

(121) Yan, X.; Wang, F.; Zheng, B.; Huang, F. Stimuli-responsive supramolecular polymeric materials. *Chemical Society Reviews* **2012,** *41* (18), 6042-6065, DOI: 10.1039/C2CS35091B.

(122) Zhuang, J.; Gordon, M. R.; Ventura, J.; Li, L.; Thayumanavan, S. Multi-stimuli responsive macromolecules and their assemblies. *Chemical Society Reviews* **2013,** *42* (17), 7421-7435, DOI: 10.1039/C3CS60094G.

(123) Liu, M.; Du, H.; Zhang, W.; Zhai, G. Internal stimuli-responsive nanocarriers for drug delivery: Design strategies and applications. *Materials Science and Engineering: C* **2017,** *71*, 1267-1280, DOI: https://doi.org/10.1016/j.msec.2016.11.030.

(124) Shen, X.; Zhang, L.; Jiang, X.; Hu, Y.; Guo, J. Reversible surface switching of nanogel triggered by external stimuli. *Angewandte Chemie International Edition* **2007,** *46* (37), 7104-7107, DOI: 10.1002/anie.200701368.

(125) Li, S.; Zou, Q.; Xing, R.; Govindaraju, T.; Fakhrullin, R.; Yan, X. Peptide-modulated self-assembly as a versatile strategy for tumor supramolecular nanotheranostics. *Theranostics* **2019,** *9* (11), 3249-3261, DOI: 10.7150/thno.31814.

(126) Vigderman, L.; Khanal, B. P.; Zubarev, E. R. Functional gold nanorods: synthesis, self-assembly, and sensing applications. *Advanced Materials* **2012,** *24* (36), 4811-4841, DOI: 10.1002/adma.201201690.

(127) Lee, M.; Jang, C.-J.; Ryu, J.-H. Supramolecular reactor from self-assembly of rod−coil

molecule in aqueous environment. *Journal of the American Chemical Society* **2004,** *126* (26), 8082-8083, DOI: 10.1021/ja048264z.

(128) Krishnamachari, Y.; Pearce, M. E.; Salem, A. K. Self-assembly of cell–microparticle hybrids. *Advanced Materials* **2008,** *20* (5), 989-993, DOI: 10.1002/adma.200701689.

(129) Schoonen, L.; van Hest, J. C. M. Compartmentalization approaches in soft matter science: from nanoreactor development to organelle mimics. *Advanced Materials* **2016,** *28* (6), 1109-1128, DOI: 10.1002/adma.201502389.

(130) Della Rocca, J.; Liu, D.; Lin, W. Nanoscale metal-organic frameworks for biomedical imaging and drug delivery. *Acc Chem Res* **2011,** *44* (10), 957-68, DOI: 10.1021/ar200028a.

(131) Batten, S. R.; Champness, N. R.; Chen, X.-M.; Garcia-Martinez, J.; Kitagawa, S.; Öhrström, L.; O'Keeffe, M.; Suh, M. P.; Reedijk, J. Coordination polymers, metal–organic frameworks and the need for terminology guidelines. *CrystEngComm* **2012,** *14* (9), 3001-3004, DOI: 10.1039/C2CE06488J.

(132) Fromm, K. M.; Sagué, J. L.; Mirolo, L. Coordination polymer networks: An alternative to classical polymers? *Macromolecular Symposia* **2010,** *291-292* (1), 75-83, DOI: 10.1002/masy.201050509.

(133) Biradha, K.; Ramanan, A.; Vittal, J. J. Coordination polymers versus metal−organic frameworks. *Crystal Growth & Design* **2009,** *9* (7), 2969-2970, DOI: 10.1021/cg801381p.

(134) Kitagawa, S.; Kitaura, R.; Noro, S.-i. Functional porous coordination polymers. *Angewandte Chemie International Edition* **2004,** *43* (18), 2334-2375, DOI: 10.1002/anie.200300610.

(135) Ma, Z.; Moulton, B. Recent advances of discrete coordination complexes and coordination polymers in drug delivery. *Coordination Chemistry Reviews* **2011,** *255* (15), 1623-1641, DOI: https://doi.org/10.1016/j.ccr.2011.01.031.

(136) Novio, F.; Simmchen, J.; Vázquez-Mera, N.; Amorín-Ferré, L.; Ruiz-Molina, D.

Coordination polymer nanoparticles in medicine. *Coordination Chemistry Reviews* **2013,** *257* (19), 2839-2847, DOI: https://doi.org/10.1016/j.ccr.2013.04.022.

(137) Gómez-Herrero, J.; Zamora, F. Coordination polymers for nanoelectronics. *Advanced Materials* **2011,** *23* (44), 5311-5317, DOI: 10.1002/adma.201101952.

(138) Masoomi, M. Y.; Morsali, A. Applications of metal–organic coordination polymers as precursors for preparation of nano-materials. *Coordination Chemistry Reviews* **2012,** *256* (23), 2921-2943, DOI: https://doi.org/10.1016/j.ccr.2012.05.032.

(139) Gangu, K. K.; Maddila, S.; Mukkamala, S. B.; Jonnalagadda, S. B. A review on contemporary metal–organic framework materials. *Inorganica Chimica Acta* **2016,** *446*, 61-74, DOI: https://doi.org/10.1016/j.ica.2016.02.062.

(140) Furukawa, H.; Cordova, K. E.; O'Keeffe, M.; Yaghi, O. M. The chemistry and applications of metal-organic frameworks. *Science* **2013,** *341* (6149), 1230444, DOI: 10.1126/science.1230444.

(141) Cai, W.; Chu, C.-C.; Liu, G.; Wáng, Y.-X. J. Metal–organic framework-based nanomedicine platforms for drug delivery and molecular imaging. *Small* **2015,** *11* (37), 4806-4822, DOI: 10.1002/smll.201500802.

(142) Llabrés i Xamena, F. X.; Abad, A.; Corma, A.; Garcia, H. MOFs as catalysts: Activity, reusability and shape-selectivity of a Pd-containing MOF. *Journal of Catalysis* **2007,** *250* (2), 294-298, DOI: https://doi.org/10.1016/j.jcat.2007.06.004.

(143) Chang, Z.; Zhang, D.-S.; Chen, Q.; Bu, X.-H. Microporous organic polymers for gas storage and separation applications. *Physical Chemistry Chemical Physics* **2013,** *15* (15), 5430-5442, DOI: 10.1039/C3CP50517K.

(144) Li, B.; Wen, H.-M.; Zhou, W.; Chen, B. Porous metal–organic frameworks for gas storage and separation: What, how, and why? *The Journal of Physical Chemistry Letters* **2014,** *5* (20), 3468-3479, DOI: 10.1021/jz501586e.

(145) Li, B.; Wen, H.-M.; Cui, Y.; Zhou, W.; Qian, G.; Chen, B. Emerging multifunctional metal–organic framework materials. *Advanced Materials* **2016,** *28* (40), 8819-8860, DOI: 10.1002/adma.201601133.

(146) Oh, M.; Mirkin, C. A. Chemically tailorable colloidal particles from infinite coordination polymers. *Nature* **2005,** *438* (7068), 651-654, DOI: 10.1038/nature04191.

(147) Spokoyny, A. M.; Kim, D.; Sumrein, A.; Mirkin, C. A. Infinite coordination polymer nano- and microparticle structures. *Chemical Society Reviews* **2009,** *38* (5), 1218-1227, DOI: 10.1039/B807085G.

(148) Rieter, W. J.; Kim, J. S.; Taylor, K. M. L.; An, H.; Lin, W.; Tarrant, T.; Lin, W. Hybrid silica nanoparticles for multimodal imaging. *Angewandte Chemie International Edition* **2007,** *46* (20), 3680-3682, DOI: 10.1002/anie.200604738.

(149) Rieter, W. J.; Pott, K. M.; Taylor, K. M. L.; Lin, W. Nanoscale coordination polymers for platinum-based anticancer drug delivery. *Journal of the American Chemical Society* **2008,** *130* (35), 11584-11585, DOI: 10.1021/ja803383k.

(150) Rieter, W. J.; Taylor, K. M. L.; Lin, W. Surface modification and functionalization of nanoscale metal-organic frameworks for controlled release and luminescence sensing. *Journal of the American Chemical Society* **2007,** *129* (32), 9852-9853, DOI: 10.1021/ja073506r.

(151) Dai, L.-X. Chiral metal–organic assemblies—A new approach to immobilizing homogeneous asymmetric catalysts. *Angewandte Chemie International Edition* **2004,** *43* (43), 5726-5729, DOI: 10.1002/anie.200460301.

(152) Rahim, M. A.; Kristufek, S. L.; Pan, S.; Richardson, J. J.; Caruso, F. Phenolic building blocks for the assembly of functional materials. *Angewandte Chemie International Edition* **2019,** *58* (7), 1904-1927, DOI: 10.1002/anie.201807804.

(153) Gref, R.; Lück, M.; Quellec, P.; Marchand, M.; Dellacherie, E.; Harnisch, S.; Blunk, T.; Müller, R. H. 'Stealth' corona-core nanoparticles surface modified by polyethylene glycol

(PEG): influences of the corona (PEG chain length and surface density) and of the core composition on phagocytic uptake and plasma protein adsorption. *Colloids and Surfaces B: Biointerfaces* **2000,** *18* (3), 301-313, DOI: https://doi.org/10.1016/S0927-7765(99)00156-3.

(154) D'souza, A. A.; Shegokar, R. Polyethylene glycol (PEG): a versatile polymer for pharmaceutical applications. *Expert Opinion on Drug Delivery* **2016,** *13* (9), 1257-1275, DOI: 10.1080/17425247.2016.1182485.

(155) Knop, K.; Hoogenboom, R.; Fischer, D.; Schubert, U. S. Poly(ethylene glycol) in drug delivery: Pros and Cons as well as potential alternatives. *Angewandte Chemie International Edition* **2010,** *49* (36), 6288-6308, DOI: 10.1002/anie.200902672.

(156) Ju, Y.; Cui, J.; Mullner, M.; Suma, T.; Hu, M.; Caruso, F. Engineering low-fouling and pH-degradable capsules through the assembly of metal-phenolic networks. *Biomacromolecules* **2015,** *16* (3), 807-14, DOI: 10.1021/bm5017139.

(157) Ju, Y.; Cui, J.; Sun, H.; Mullner, M.; Dai, Y.; Guo, J.; Bertleff-Zieschang, N.; Suma, T.; Richardson, J. J.; Caruso, F. Engineered metal-phenolic capsules show tunable targeted delivery to cancer cells. *Biomacromolecules* **2016,** *17* (6), 2268-76, DOI: 10.1021/acs.biomac.6b00537.

(158) Park, T.; Kim, J. Y.; Cho, H.; Moon, H. C.; Kim, B. J.; Park, J. H.; Hong, D.; Park, J.; Choi, I. S. Artificial spores: Immunoprotective nanocoating of red blood cells with supramolecular ferric ion-tannic acid complex. *Polymers (Basel)* **2017,** *9* (4), 140, DOI: 10.3390/polym9040140.

(159) Dai, Y.; Cheng, S.; Wang, Z.; Zhang, R.; Yang, Z.; Wang, J.; Yung, B. C.; Wang, Z.; Jacobson, O.; Xu, C.; Ni, Q.; Yu, G.; Zhou, Z.; Chen, X. Hypochlorous acid promoted platinum drug chemotherapy by myeloperoxidase-encapsulated therapeutic metal phenolic nanoparticles. *ACS Nano* **2018,** *12* (1), 455-463, DOI: 10.1021/acsnano.7b06852.

(160) Liu, T.; Zhang, M.; Liu, W.; Zeng, X.; Song, X.; Yang, X.; Zhang, X.; Feng, J. Metal

ion/tannic acid assembly as a versatile photothermal platform in engineering multimodal nanotheranostics for advanced applications. *ACS Nano* **2018,** *12* (4), 3917-3927, DOI: 10.1021/acsnano.8b01456.

(161) Wang, X.; Li, X.; Liang, X.; Liang, J.; Zhang, C.; Yang, J.; Wang, C.; Kong, D.; Sun, H. ROS-responsive capsules engineered from green tea polyphenol–metal networks for anticancer drug delivery. *Journal of Materials Chemistry B* **2018,** *6* (7), 1000-1010, DOI: 10.1039/C7TB02688A.

(162) Fan, J.-X.; Zheng, D.-W.; Mei, W.-W.; Chen, S.; Chen, S.-Y.; Cheng, S.-X.; Zhang, X.-Z. A metal–polyphenol network coated nanotheranostic system for metastatic tumor treatments. *Small* **2017,** *13* (48), 1702714, DOI: 10.1002/smll.201702714.

(163) Zhu, W.; Liang, S.; Wang, J.; Yang, Z.; Zhang, L.; Yuan, T.; Xu, Z.; Xu, H.; Li, P. Europium-phenolic network coated BaGdF5 nanocomposites for tri-modal computed tomography/magnetic resonance/luminescence imaging. *Journal of Materials Science: Materials in Medicine* **2017,** *28* (5), 74, DOI: 10.1007/s10856-017-5888-5.

(164) Ejima, H.; Richardson, J. J.; Caruso, F. Metal-phenolic networks as a versatile platform to engineer nanomaterials and biointerfaces. *Nano Today* **2017,** *12*, 136-148, DOI: https://doi.org/10.1016/j.nantod.2016.12.012.

(165) Fleischer, E. B.; Palmer, J. M.; Srivastava, T. S.; Chatterjee, A. Thermodyamic and kinetic properties of an iron-porphyrin system. *Journal of the American Chemical Society* **1971,** *93* (13), 3162-3167, DOI: 10.1021/ja00742a012.

(166) Raymond, K. N.; Carrano, C. J. Coordination chemistry and microbial iron transport. *Accounts of Chemical Research* **1979,** *12* (5), 183-190, DOI: 10.1021/ar50137a004.

(167) Wilker, J. J. Marine bioinorganic materials: mussels pumping iron. *Current Opinion in Chemical Biology* **2010,** *14* (2), 276-283, DOI: https://doi.org/10.1016/j.cbpa.2009.11.009.

(168) Saowalak, K.; Titipun, T.; Somchai, T.; Chalermchai, P. Iron(III)-tannic molecular

nanoparticles enhance autophagy effect and T(1) MRI contrast in liver cell lines. *Sci Rep* **2018,** *8* (1), 6647-6647, DOI: 10.1038/s41598-018-25108-1.

(169) Zeng, J.; Cheng, M.; Wang, Y.; Wen, L.; Chen, L.; Li, Z.; Wu, Y.; Gao, M.; Chai, Z. pH-Responsive Fe(III)–gallic acid nanoparticles for in vivo photoacoustic-imaging-guided photothermal therapy. *Advanced Healthcare Materials* **2016,** *5* (7), 772-780, DOI: 10.1002/adhm.201500898.

(170) Han, K.; Zhang, W.-Y.; Zhang, J.; Ma, Z.-Y.; Han, H.-Y. pH-Responsive nanoscale coordination polymer for efficient drug delivery and real-time release monitoring. *Advanced Healthcare Materials* **2017,** *6* (19), 1700470, DOI: 10.1002/adhm.201700470.

(171) Liu, F.; He, X.; Chen, H.; Zhang, J.; Zhang, H.; Wang, Z. Gram-scale synthesis of coordination polymer nanodots with renal clearance properties for cancer theranostic applications. *Nature Communications* **2015,** *6* (1), 8003, DOI: 10.1038/ncomms9003.

(172) Yang, Y.; Liu, J.; Liang, C.; Feng, L.; Fu, T.; Dong, Z.; Chao, Y.; Li, Y.; Lu, G.; Chen, M.; Liu, Z. Nanoscale metal–organic particles with rapid clearance for magnetic resonance imaging-guided photothermal therapy. *ACS Nano* **2016,** *10* (2), 2774-2781, DOI: 10.1021/acsnano.5b07882.

(173) Jin, Q.; Zhu, W.; Jiang, D.; Zhang, R.; Kutyreff, C. J.; Engle, J. W.; Huang, P.; Cai, W.; Liu, Z.; Cheng, L. Ultra-small iron-gallic acid coordination polymer nanoparticles for chelator-free labeling of ^{64}Cu and multimodal imaging-guided photothermal therapy. *Nanoscale* **2017,** *9* (34), 12609-12617, DOI: 10.1039/C7NR03086J.

(174) Dai, Y.; Guo, J.; Wang, T.-Y.; Ju, Y.; Mitchell, A. J.; Bonnard, T.; Cui, J.; Richardson, J. J.; Hagemeyer, C. E.; Alt, K.; Caruso, F. Self-assembled nanoparticles from phenolic derivatives for cancer therapy. *Advanced Healthcare Materials* **2017,** *6* (16), 1700467, DOI: 10.1002/adhm.201700467.

Chapter 2

Instrumentation

2.1. Aim

This chapter briefly describes the underlying principles behind the major instruments used for the materials characterization in this thesis. Details of instrument parameters, settings and experimental protocols will be presented in the relevant chapters.

2.2. Instruments

2.2.1. Differential Interference Contrast Microscopy

Bright field microscopy usually suffers from the relatively low resolution and low contrast that yields poor images, especially when viewing living or transparent specimens. To cope with this issue, differential interference contrast (DIC) microscopy is an optic microscopy that was developed by Polish physicist Georges Nomarski.[1-3] By taking use of the interferometry of the optical path length in the sample, DIC can greatly enhance the contrast and allow visualization of some invisible features in unstained and transparent samples.

The Figure 2.1 illustrates the typical component of a DIC microscope set-up. The light passes through a standard polarizing filter and a Wollaston prism, and are then split into two separate polarized beams by a distance called the shear distance.[4] These two separate polarized beams are perpendicular to each other and pass through the specimen, and encounter altered paths due to the difference in specimen properties including thickness, refractive index and surface properties. These two beams are collected and combined in a second Wollaston prism and polarizing filter, which generate interference patterns and various contrast based on the variations in their optical path. Finally, the images of specimen can be observed and acquired by a camera that is installed to the microscopy. In this thesis, DIC microscopy was applied to image the morphology of Euc/Fe(III) capsules formed from a complex multicomponent mixture (Chapter 3) and metal-phenolic crystals (Chapter 5).

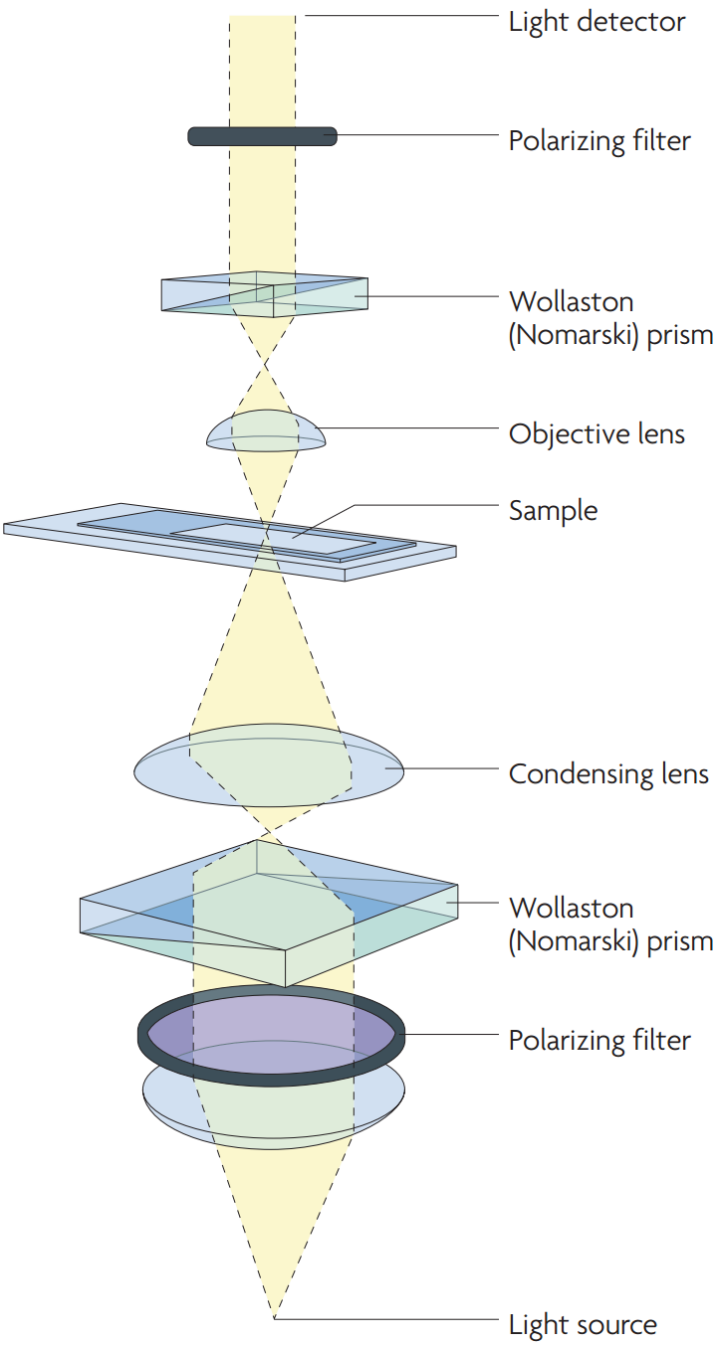

Figure 2.1. Illustration of the components of the differential interference contrast microscope (reproduced from reference 4).[4]

2.2.2. Fluorescence Microscopy

A fluorescence microscope uses the fluorescent indicator to generate an image, including typical epifluorescence microscopes and those with additional features, including three

dimensional imaging, deconvolution microscopy and confocal microscopy.[5-6] As shown in Figure 2.2,[7] a typical fluorescence microscope consists of a light source (e.g. xenon arc lamp or a mercury-vapor lamp, high-power LEDs and lasers), the excitation filter for blocking other wavelengths, the dichroic mirror and the emission filter. In principle, the illuminated light with a specific wavelength is collected by blocking other wavelengths of the excited light using a spectral emission filter. When they pass through the specimens, they can activate the fluorophores in the specimen that emit light with longer wavelengths. During this process, the illuminated light activates the electron of fluorophores in the specimen which jump to higher energy levels. After the electron returns to its normal state, the energy stored in the excited electrons in fluorophores will be emitted and generate fluorescence. The generated fluorescence is separated from the illuminated light and then focused on the detector. In this thesis, fluorescence microscopy was used to image the movement of metal-phenolic crystals by taking virtue of intrinsic fluorescence of ellagic acid (Chapter 5).

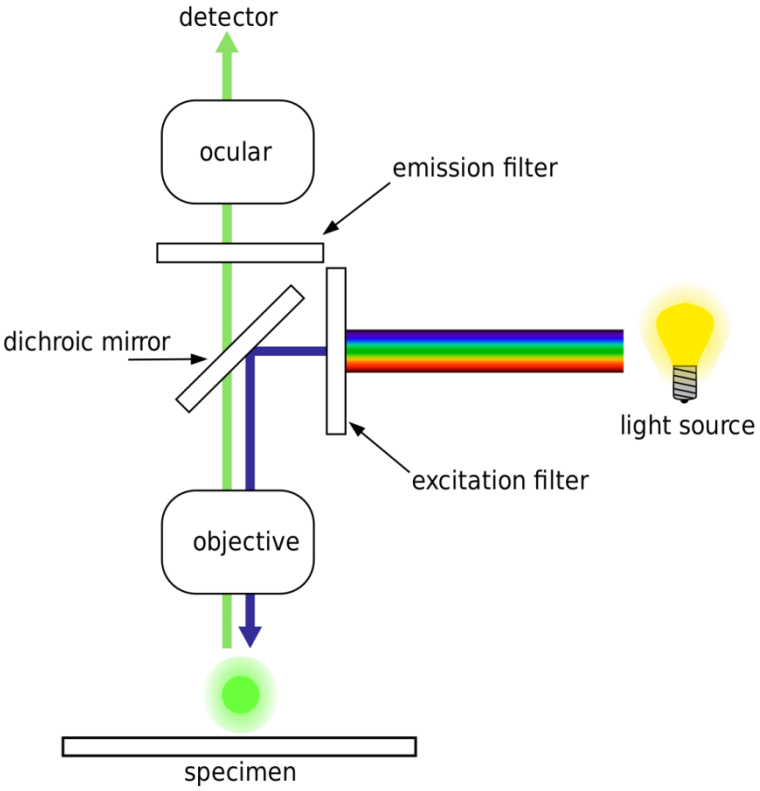

Figure 2.2. Schematic illustration of a fluorescence microscope set-up (reproduced from

reference 7).[7]

2.2.3. Transmission Electron Microscopy

Transmission electron microscopy (TEM) uses an electron beam to transmit through the specimen to acquire an image. Unlike optical light microscopy, TEM uses the smaller de Broglie wavelength of the electrons, thus image resolution is significantly higher than that of light microscopes, enabling TEM to capture fine detail at the nanoscale.[8] TEM is a powerful tool and has great applications in diverse fields including the physical, materials, chemical and biological sciences.[9-11]

Figure 2.3 shows the instrumental setup of a typical TEM, including an electron emission source (the electron gun), a vacuum system, a series of electromagnetic lenses, as well as electrostatic plates, specimen stage and imaging devices.[9] Briefly, the electron gun generates the electron stream by thermionic emission or field emission. Then the electron stream travels through the electromagnetic lenses that controls the beam states, and apertures which exclude the electrons that are out of a fixed distance from the optic axis. After passing through the specimen, the electrons are focused at a fluorescent screen for imaging. The electron beam travels through the specimen and apertures where the electron beam is focused to generate a magnified image. Finally, the image is further magnified by the projector lens and then focused onto a viewing screen. In general, if some electrons are absorbed or scattered by the samples when the electrons go through the sample, fewer electrons are collected by the camera, which results in a darker TEM image. Conversely, if the electrons go through some areas easily, the color of these areas will appear brighter in TEM image.

In this thesis, TEM was used to image the morphology of MPN capsules formed from complex multicomponent systems (Chapter 3) and PEG particles crosslinked by metal-phenolic coordination (Chapter 4), and determine the elemental distribution of metal-phenolic crystals (Chapter 5).

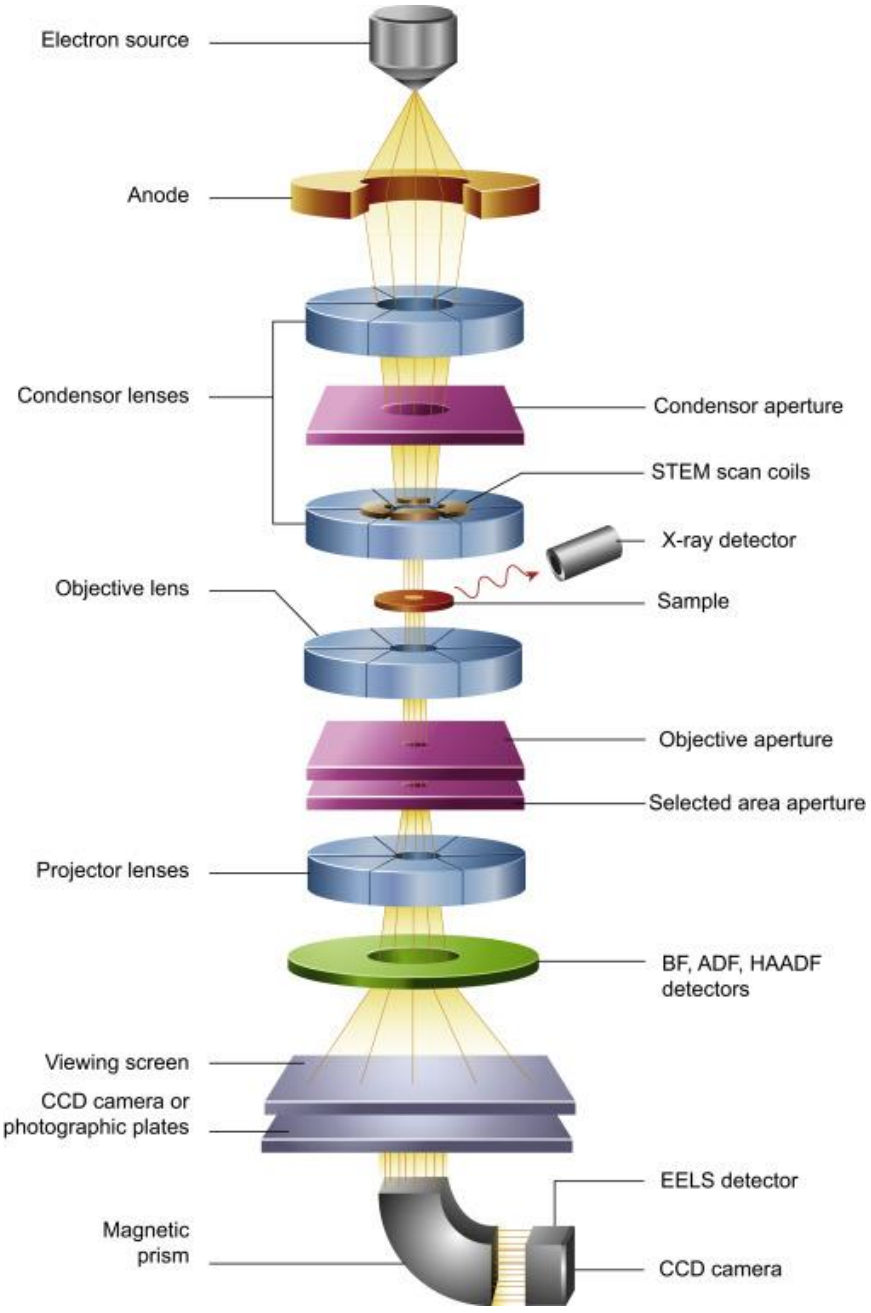

Figure 2.3. Illustration of the composition of TEM set-up (reproduced from reference 9).[9]

2.2.4. Scanning Electron Microscope

A scanning electron microscope (SEM) is another type of an electron microscope. Unlike TEM, SEM generates images by scanning the surface of a sample with an electron beam.[12-13] The typical set-up of an SEM is shown in Figure 2.4.[9] Similar to the TEM set-up, the electron stream emitted from the electron gun travels through an electromagnetic field that is critical for

controlling the beam states. When the electrons reach the specimen, some electrons are scattered in the sample. These scattered electrons are collected to produce images. To get a high quality image, a gold cast is usually coated on the specimen surface to create a conductive layer of metal during SEM sample preparation,[14] which is beneficial for charging inhibition, thermal damage reduction and secondary electron signal improvement. In this thesis, high resolution SEM was used to characterize the morphology of metal-phenolic crystals (Chapter 5).

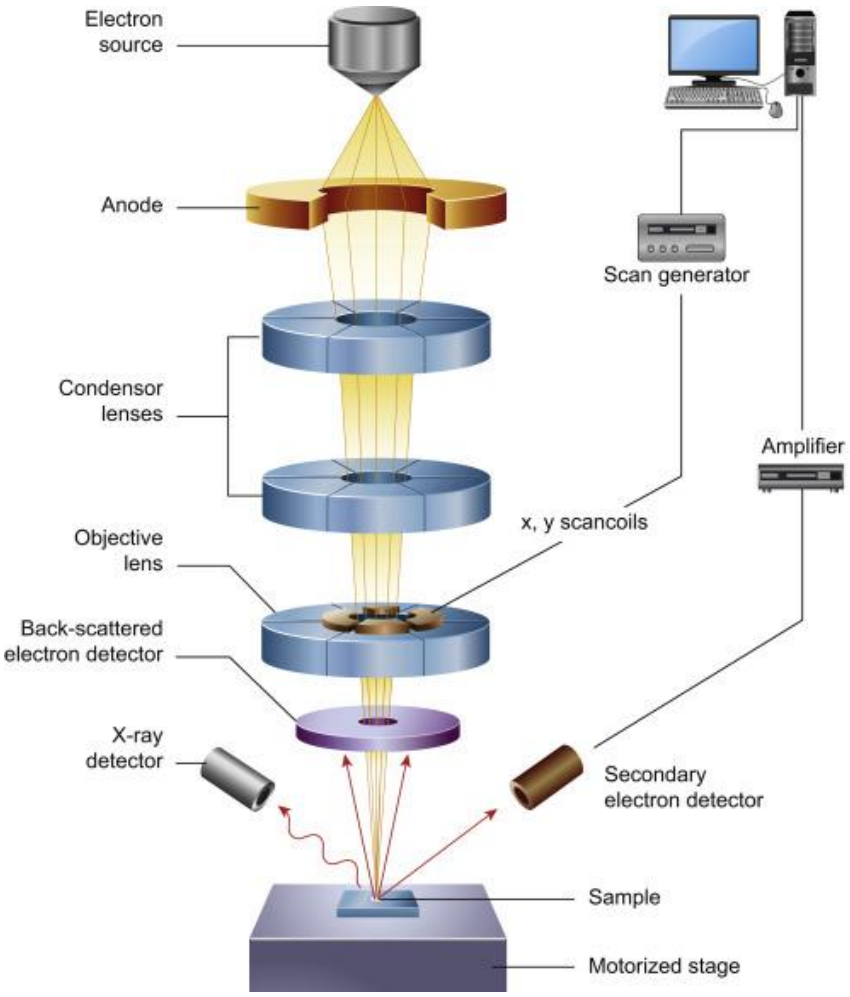

Figure 2.4. Illustration of the SEM components and set-up (reproduced from reference 9).[9]

2.2.5. Ultraviolet–visible Absorption Spectroscopy

Ultraviolet–visible (UV-Vis) absorption spectroscopy is a commonly used spectroscopy technique for the qualitative and quantitative determination of different compounds, including transition metal ions and highly conjugated organic molecules.[15-16] The principle behind UV-Vis absorption spectroscopy is that molecules and atoms contain bonding and non-bonding electrons[17], which could be activated by UV-Vis light illumination, and then jump to anti-bonding states. Possible low-to-high energy level transitions are shown below:

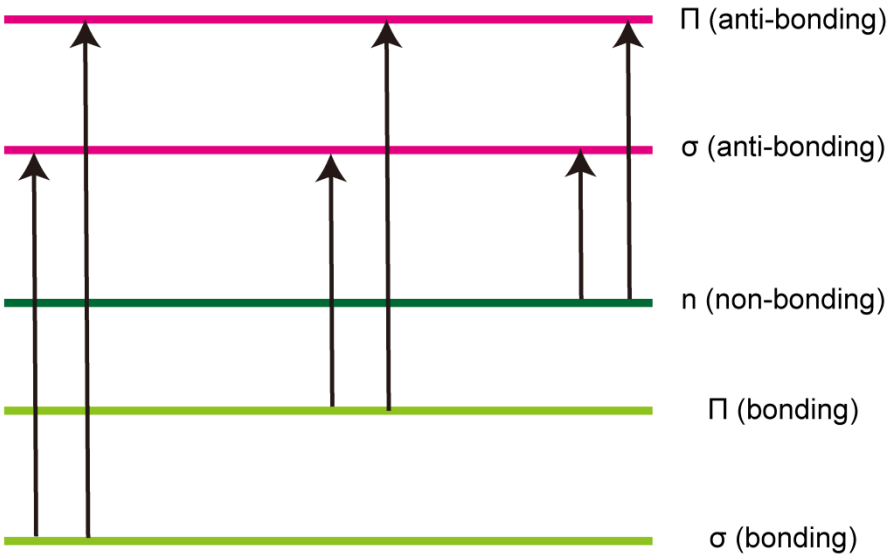

Figure 2.5. Possible light-induced electronic transitions.

The electrons in the molecule or compound can receive the light energy, are excited and then jump from the ground state to an empty anti-bonding orbital. The larger gap above corresponds to the greater energy required for the electronic activation. When the light energy, which is associated with its wavelength, meets the gap of any electronic transitions, the molecule or compound will absorb these light (Figure 2.5). Since each molecule contains different structural groups that absorb light at specific wavelengths, the UV-Vis absorption spectroscopy can be employed to determine the structural groups in the measured materials.

The UV-Vis absorption spectroscopy can also be used for quantitative measurements according to the Beer–Lambert law[15, 18]:

$$A = \log_{10} I/I_0 = \varepsilon c L \quad \text{..... (Equation 2.1)}$$

where, A is the absorbance of compound, I (W/m^2) and I_0 (W/m^2) is the transmitted and incident light intensity at a given wavelength, ε (m^2/mol) is a constant-the extinction coefficient, L (m) is the path length through the sample, c (mol/m^3) presents the concentration of the measured absorbing compounds.

Figure 2.6 shows a typical composition of double beam spectrophotometer for measuring UV-Vis absorption: a light source, filter, the monochromator, the sample cells and the detector. The light source is usually made of deuterium arc lamps and tungsten lamps; the former is for UV wavelengths and the latter is for visible wavelengths. During measurement, the light passes through the monochromator which acts as a wavelength selector and it splits the beam into two: one that reaches the sample cuvette and one that reaches the reference cuvette. Then, the passed light reaches the detector such as photodiode, which measures the wavelength of the absorbed light as well as the extent of absorption. In this thesis, UV-Vis absorption spectroscopy was used to characterize Euc/Fe^{III} complexes formed from multicomponent mixtures in Chapter 3, and metal-PEG phenolic complexes in Chapter 4.

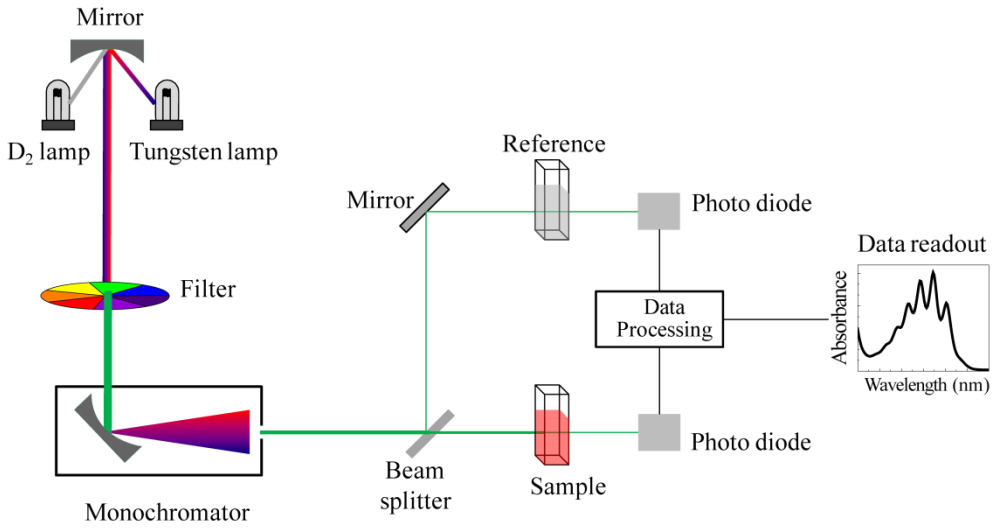

Figure 2.6. Schematic illustration of a double-beam UV-Vis spectrophotometer.

2.2.6. Raman Microscopy

Raman spectroscopy is an analysis technique used to detect vibrations in molecules.[19-20] It relies on the Raman scattering that refers to a small fraction of the scattered light that change their frequency due to inelastic scattering when the light encounters the molecule.[21] These Raman scattered light can be categorized into two different types: anti-Stokes line with shorter wavelength than the wavelength of incident radiation, and Stokes line with longer wavelength than the incident radiation. As the frequency variation is usually specific to phonon in crystal and molecular vibration, Raman spectroscopy could be used for measuring material composition and crystal lattice information, and detect small differences between similar molecules and chemical species, such as vibrational and/or rotational, and bending forces within the chemical bonds.[22-23]

Confocal Raman microscopy is a standard optical microscope that is coupled with a Raman spectrometer.[24-25] Figure 2.7 shows the general set-up of a typical confocal Raman microscopy, including an excitation laser, filters, a monochromator, and an optically sensitive detector such as a charge-coupled device (CCD). The confocal Raman microscope can analyze a small region (a point) of a specimen, such as individual particles with dimensions (size below 1 μm).

Moreover, recent advances in 3D techniques have enabled direct 3D Raman imaging of the chemical composition in three dimensions. The advantages of confocal Raman microscopy include non-destructive imaging, user friendliness, and sample versatility, i.e., it can be done in both solid samples and in aqueous environments. In this thesis, confocal Raman microscopy was used to characterize the chemical composition of metal-phenolic particles in Chapter 5.

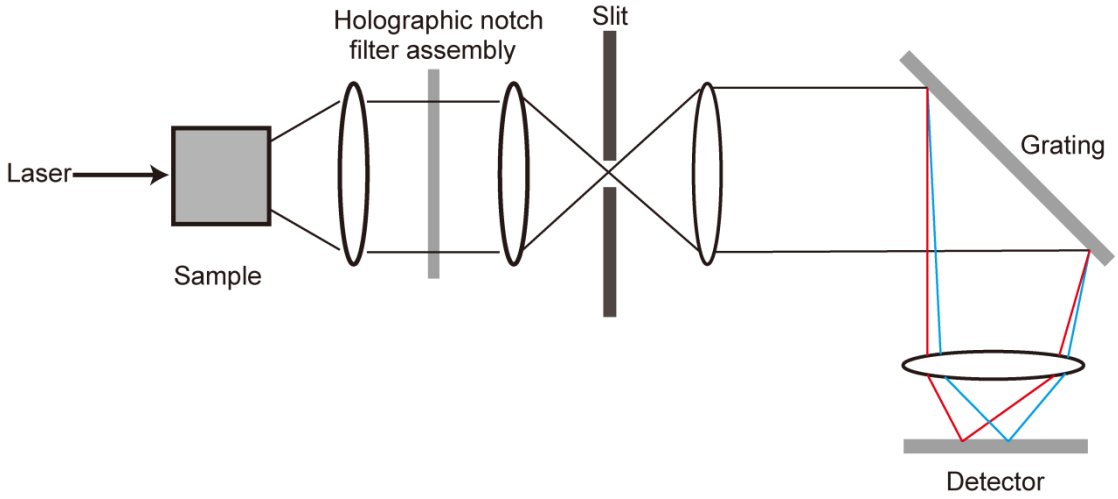

Figure 2.7. Illustration of the composition of confocal Raman microscopy set-up.

2.2.7. X-ray Photoelectron Spectroscopy

X-ray Photoelectron Spectroscopy (XPS) is one most commonly used analysis technique for surface chemistry. It is able to provide the information of the elemental composition as well as their chemical and electronic state within a sample in a qualitative and quantitative way.[26-27] The principle behind XPS is based on the photoelectric effect,[28] which involves the emission of electrons from an X-ray beam- irradiated solid surface. The photoelectric effect was firstly discovered by the great physicist Heinrich Rudolfd Hertz in 1887, and was then explained theoretically by the famous physicist Albert Einstein in 1905. As shown in Figure 2.8, when the material surface is irradiated with a X-ray light beam, the material will absorb the light and emit electrons. These emitted electronsm which have kinetic energy (E_{kin}) are called photoelectrons. Measuring these emitted electrons and the kinetic energy give the XPS

spectrum of the sample.

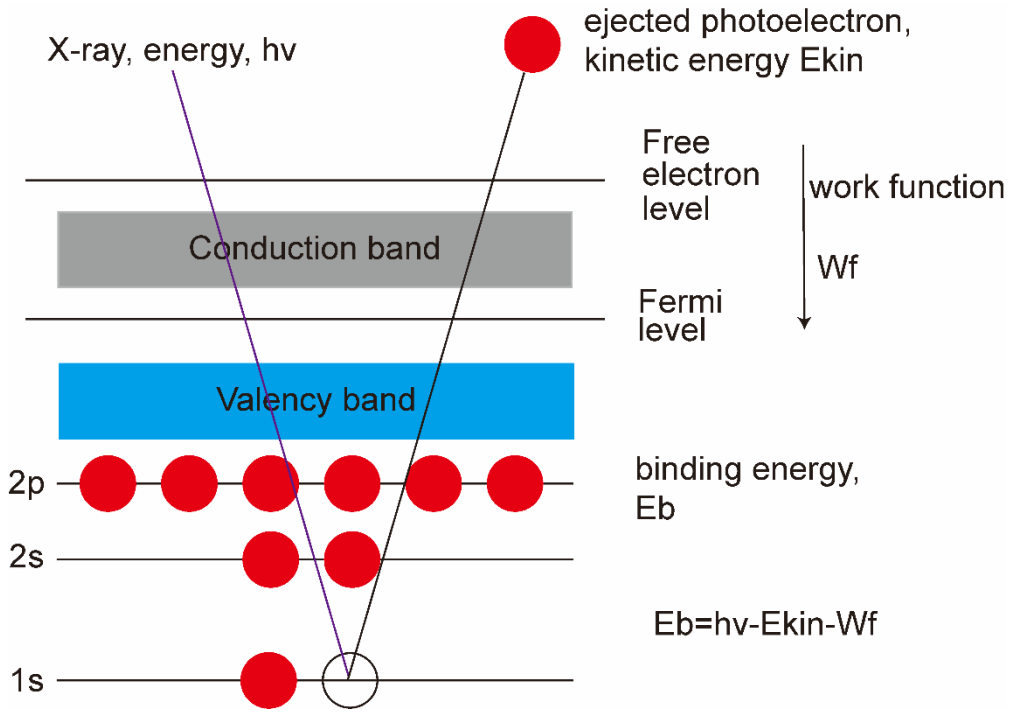

Figure 2. 8. Illustration of the photo-induced emission of photoelectron.

The Figure 2.9 shows the typical component of an XPS instrument, consisting of a sample stage, an X-ray source, an ultra-high vacuum (UHV) stainless steel chamber with pumps and electron energy analyzer and detector.[29] When the samples are illuminated with X-ray beams, they emit electrons with a range of energies. The electron collection lens collect a part of these emitted electrons, and then transfer and focus them onto the analyzer. These processes are performed under ultra-high vacuum conditions to count the electrons and minimize errors, as the electron analyzer is usually one meter away from the sample stage. The XPS spectrum is expressed by plotting the number of the detected electrons versus the binding energy of the detected electrons. As every element has its characteristic binding energy range, XPS can be used to detect almost all elements except hydrogen and helium in the periodic table. Moreover, as the characteristic binding energy is quite sensitive to the chemical environment of the element, small variation in the binding energy of the element in the XPS spectrum termed as

"chemical shift" can be employed to determine the chemical state (e.g. M^0, M^{+1}, M^{+2}) of elements.

In this thesis, XPS was used to characterize the elemental analysis of Euc/Fe^{III} capsules in Chapter 3, PEG-MPN nanoparticles in Chapter 4 and EA-Zn crystals in Chapter 5.

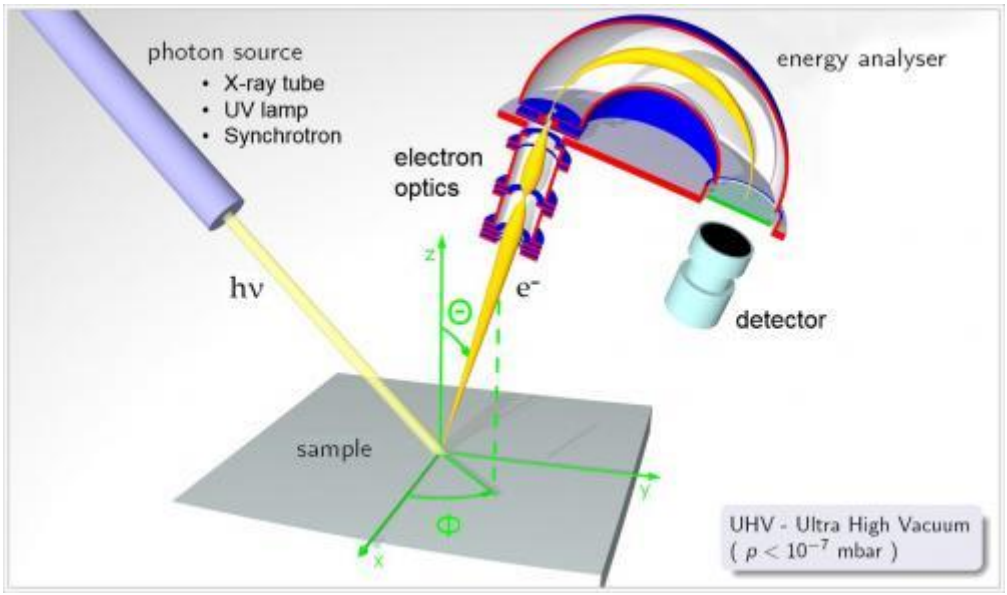

Figure 2.9. Cartoon illustration of the composition and set-up of an XPS (adapted from reference 29).[29] X-ray beams irradiate the samples, which emits electrons with a range of energies. The generated electron is collocated and transferred to the energy analyser for detecting the measuring the kinetic energy of the photoelectrons.

2.2.8. X-ray Powder Diffraction

X-ray powder diffraction (XRD) is an analytical technique that is primarily used for determining the crystallographic structure of a material.[30-31] The basic principle behind XRD is based on the constructive interference between the monochromatic X-ray and the crystalline sample. When the conditions of X-ray and crystalline parameters meet Bragg's Law ($n\lambda=2d \sin \theta$), it will cause a diffraction pattern as shown in Figure 2.10. As the diffraction usually requires the material to have a highly regular structure, only crystalline

materials will diffract the X-ray. Scanning the specimen with a range of 2θ angles can give every possible diffraction direction of the crystalline lattice in the measured material, which allows the identification of the crystallographic structure by comparing them with standard reference patterns.

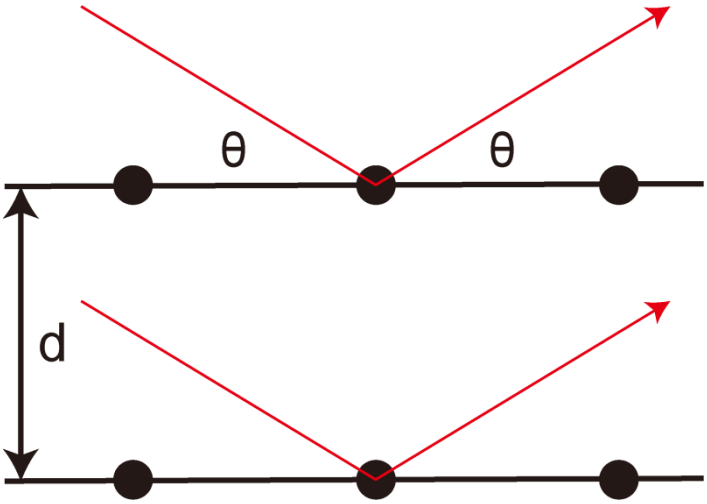

Figure 2.10. Illustration of photoemission process.

A typical XRD instrument set-up consists of three major parts: an X-ray beam, the sample stage and an X-ray detector. The X-ray beam is emitted by impinging the target materials in the tube using the accelerating electrons generated by a heated filament. These X-ray beams are directed to focus onto the samples to give the reflected X-rays. By rotating the samples and detectors, a peak in intensity will occur when the condition meets the Bragg Equation. The detector is used to record and process these X-ray and output them to an external device (e.g. computer monitor). So far, XRD is the most commonly used techniques to identify the crystalline structures of unknown materials. In this thesis, XRD was used to determine the crystallographic structure of EA-Zn crystals in Chapter 5.

2.2.9. Liquid Chromatography–Mass Spectrometry (LC-MS)

Liquid chromatography–mass spectrometry (LC-MS), which is a combination of liquid

chromatography (LC) and mass spectrometry (MS), is an analytical technique used for identifying components in a complex mixture.[32-33] While LC provides the capability to physically separate the components in a complex mixture, MS offers high sensitivity.

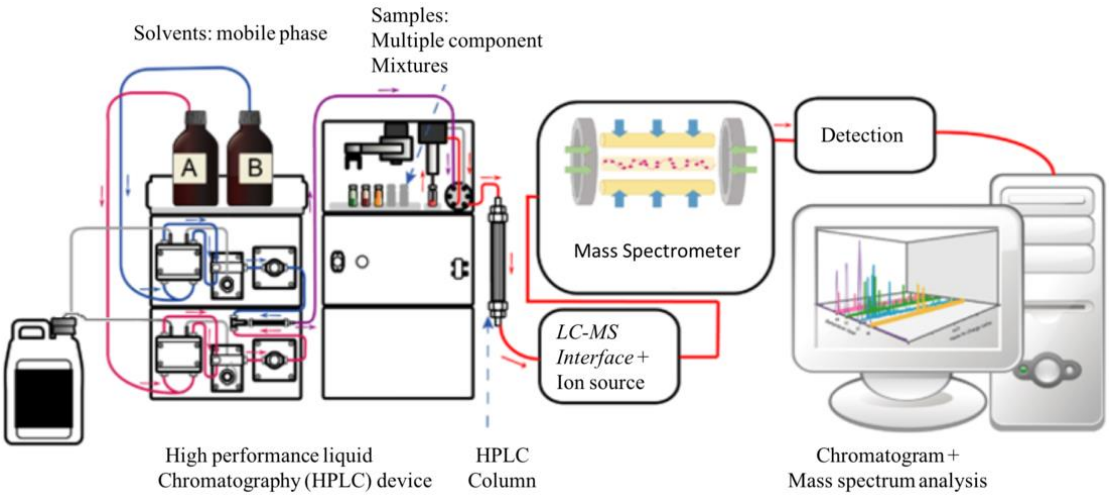

Figure 2.11. Illustration of LC-MS set-up. (reproduced from reference 34).[34]

Figure 2.11 shows the general components of a LC-MS set-up.[34] The typical process of LC-MS analysis consist of the following stages: first, the samples are injected into the HPLC column, in which different component are separated between the mobile phase and the stationary phase. The retention and separation of molecules in the column are greatly affected by the chromatography mode but may also be influenced by factors, including hydrophobic interaction, ion-pair, ion exchange and surface localization within the column. The separated components are then castrated into an atmospheric pressure ion source that convert theseparated components into ions in the gas phase in the mass spectrometer. These ions are subjected to analysis by the mass analyser based on their mass/charge (m/z) ratio. Finally, the ions emerging from the mass analyser are counted by the detector that could also amplify the signals from the ions. In this thesis, the LC-MS was used to determine the phenolic compounds present in complex multicomponent solutions.

In this thesis, LC-MS was used to identify the phenolic ligands in the eucalyptus (Euc) leaf extracts and that in disassembled Euc/Fe^{III} capsules in Chapter 3.

2.2.10. Solvation Model based on Density

Solvation model is a computational method in computational chemistry that aims at explaining the behavior of a solute in a solvent. The solvation model allows the simulation and thermodynamic calculations for understanding and predicting the physical and chemical processes occurring in a solution. There are several different types of solvation models. Among them, solvation model based on density (SMD) is one widely used model that is based on the charge density of a solute in a quantum mechanical scale, which is in interaction with its surrounding solvent. SMD is a universal method that is applicable to a great variety of solutes (charged or uncharged) in many solvents with a few key known parameters (e.g. dielectric constant and refractive index).

In this thesis, quantum mechanics (QM) calculations in were performed using Gaussian 16[35] on charge-neutral ellagic acid in different solvents using the SMD in the density functional theory.

2.3. References

(1) Rosenberger, H. E. Differential interference contrast microscopy. *Interpretive Techniques for Microstructural Analysis*; McCall, J. L.; French, P. M., Eds.; Springer US: Boston, MA, 1977; pp 79-104.

(2) Hartman, J. S.; Gordon, R. L.; Lessor, D. L. Nomarski differential interference contrast microscopy for surface slope measurements: An examination of techniques. *Appl. Opt.* **1981,** *20* (15), 2665-2669, DOI: 10.1364/AO.20.002665.

(3) Padawer, J. The Nomarski interference-contrast microscope. An experimental basis for image interpretation*. *Journal of the Royal Microscopical Society* **1968,** *88* (3), 305-349, DOI: 10.1111/j.1365-2818.1968.tb00616.x.

(4) Rosenthal, C. K. Differential interference contrast. Video-enhanced differential interference contrast. *Nature Cell Biology* **2009**, DOI: doi:10.1038/ncb1943.

(5) Sanderson, M. J.; Smith, I.; Parker, I.; Bootman, M. D. Fluorescence microscopy. *Cold Spring Harb Protoc* **2014,** *2014* (10), pdb.top071795-pdb.top071795, DOI: 10.1101/pdb.top071795.

(6) Masters, B. R. The development of fluorescence microscopy. *eLS* **2010**, DOI: doi:10.1002/9780470015902.a0022093

(7) https://en.wikipedia.org/wiki/Fluorescence_microscope.

(8) Williams, D. B.; Carter, C. B. The transmission electron microscope. *Transmission Electron Microscopy: A Textbook for Materials Science*; Williams, D. B.; Carter, C. B., Eds.; Springer US: Boston, MA, 1996; pp 3-17.

(9) Inkson, B. J. 2 - Scanning electron microscopy (SEM) and transmission electron microscopy (TEM) for materials characterization. *Materials Characterization Using Nondestructive Evaluation (NDE) Methods*; Hübschen, G.; Altpeter, I.; Tschuncky, R.; Herrmann, H.-G., Eds.; Woodhead Publishing: 2016; pp 17-43.

(10) Tang, C. Y.; Yang, Z. Chapter 8 - Transmission electron microscopy (TEM). In *Membrane Characterization*; Hilal, N.; Ismail, A. F.; Matsuura, T.; Oatley-Radcliffe, D., Eds.; Elsevier: 2017; pp 145-159.

(11) Koster, A. J.; Ziese, U.; Verkleij, A. J.; Janssen, A. H.; de Jong, K. P. Three-dimensional transmission electron microscopy: A novel imaging and characterization technique with nanometer scale resolution for materials science. *The Journal of Physical Chemistry B* **2000,** *104* (40), 9368-9370, DOI: 10.1021/jp0015628.

(12) Smith, K. C. A.; Oatley, C. W. The scanning electron microscope and its fields of application. *British Journal of Applied Physics* **1955,** *6* (11), 391-399, DOI: 10.1088/0508-3443/6/11/304.

(13) Paddock, S. W. Principles and practices of laser scanning confocal microscopy. *Molecular Biotechnology* **2000,** *16* (2), 127-149, DOI: 10.1385/MB:16:2:127.

(14) Kral, M. J. a. R. Sample preparations for scanning electron microscopy-life science. *IntechOpen* **2016**, DOI: 10.5772/61720.

(15) Perkampus, H.-H. UV-VIS spectroscopy and its applications. **1992**, DOI: https://doi.org/10.1007/978-3-642-77477-5.

(16) Upstone, S. L. Ultraviolet/visible light absorption spectrophotometry in clinical chemistry update based on the original article by Stephen L. Upstone, Encyclopedia of Analytical Chemistry, © 2000, John Wiley & Sons, Ltd. *Encyclopedia of Analytical Chemistry* **2013**, DOI: doi:10.1002/9780470027318.a0547.pub2

(17) *Principles and Techniques of Biochemistry and Molecular Biology*, 7 ed.; Cambridge University Press: Cambridge, 2010.

(18) Ingle, J. D., Jr.; Crouch, S. R. *Spectrochemical analysis*, Prentice Hall College Book Division: United States, 1988.

(19) Book Reviews. *J. Opt. Soc. Am.* **1978,** *68* (5), 719-719, DOI: 10.1364/JOSA.68.000719.

(20) Lord, R. C. Introduction to infrared and Raman spectroscopy. *Journal of the American Chemical Society* **1965,** *87* (5), 1155-1156, DOI: 10.1021/ja01083a063.

(21) Cantarero, A. Raman scattering applied to materials science. *Procedia Materials Science* **2015,** *9*, 113-122, DOI: https://doi.org/10.1016/j.mspro.2015.04.014.

(22) Bell, I. M.; Clark, R. J. H.; Gibbs, P. J. Raman spectroscopic library of natural and synthetic pigments (pre- ≈ 1850 AD). *Spectrochimica Acta Part A: Molecular and Biomolecular Spectroscopy* **1997,** *53* (12), 2159-2179, DOI: https://doi.org/10.1016/S1386-1425(97)00140-6.

(23) De Gelder, J.; De Gussem, K.; Vandenabeele, P.; Moens, L. Reference database of Raman spectra of biological molecules. *Journal of Raman Spectroscopy* **2007,** *38* (9), 1133-1147, DOI: 10.1002/jrs.1734.

(24) Gomes da Costa, S.; Richter, A.; Schmidt, U.; Breuninger, S.; Hollricher, O. Confocal Raman microscopy in life sciences. *Morphologie* **2019,** *103* (341), 11-16, DOI: 10.1016/j.morpho.2018.12.003.

(25) Houlne, M. P.; Sjostrom, C. M.; Uibel, R. H.; Kleimeyer, J. A.; Harris, J. M. Confocal Raman microscopy for monitoring chemical reactions on single optically trapped, solid-phase support particles. *Analytical Chemistry* **2002,** *74* (17), 4311-4319, DOI: 10.1021/ac020325t.

(26) Jenkins, R. Q. X.-R. S. B. R. C. P., Quantitative X-ray spectrometry. CRC Press: Boca Raton 1995. https://doi.org/10.1201/9781482273380.

(27) Biesinger, M. C.; Payne, B. P.; Lau, L. W. M.; Gerson, A.; Smart, R. S. C. X-ray photoelectron spectroscopic chemical state quantification of mixed nickel metal, oxide and hydroxide systems. *Surface and Interface Analysis* **2009,** *41* (4), 324-332, DOI: 10.1002/sia.3026.

(28) Buckingham, M. J. The surface photoelectric effect. *Physical Review* **1950,** *80* (4), 704-708, DOI: 10.1103/PhysRev.80.704.

(29) X-ray Photoelectron Spectroscopy (XPS). https://ywcmatsci.yale.edu/xps.

(30) Lavina, B.; Dera, P.; Downs, R. T. Modern X-ray diffraction methods in mineralogy and geosciences. *Reviews in Mineralogy and Geochemistry* **2014,** *78* (1), 1-31, DOI: 10.2138/rmg.2014.78.1.

(31) Smith, D. K.; Johnson, G. G.; Scheible, A.; Wims, A. M.; Johnson, J. L.; Ullmann, G. Quantitative X-ray powder diffraction method using the full diffraction pattern. *Powder Diffraction* **2013,** *2* (2), 73-77, DOI: 10.1017/S0885715600012409.

(32) Allwood, J. W.; Goodacre, R. An introduction to liquid chromatography–mass spectrometry instrumentation applied in plant metabolomic analyses. *Phytochemical Analysis* **2010,** *21* (1), 33-47, DOI: 10.1002/pca.1187.

(33) Stachniuk, A.; Fornal, E. Liquid chromatography-mass spectrometry in the analysis of pesticide residues in food. *Food Analytical Methods* **2016,** *9* (6), 1654-1665, DOI: 10.1007/s12161-015-0342-0.

(34) https://en.wikipedia.org/wiki/Liquid_chromatography–mass_spectrometry.

(35) Frisch, M. J.; Trucks, G. W.; Schlegel, H. B.; Scuseria, G. E.; Robb, M. A.; Cheeseman, J. R.; Scalmani, G.; Barone, V.; Petersson, G. A.; Nakatsuji, H.; Li, X.; Caricato, M.; Marenich, A. V.; Bloino, J.; Janesko, B. G.; Gomperts, R.; Mennucci, B.; Hratchian, H. P.; Ortiz, J. V.; Izmaylov, A. F.; Sonnenberg, J. L.; Williams; Ding, F.; Lipparini, F.; Egidi, F.; Goings, J.; Peng, B.; Petrone, A.; Henderson, T.; Ranasinghe, D.; Zakrzewski, V. G.; Gao, J.; Rega, N.; Zheng, G.; Liang, W.; Hada, M.; Ehara, M.; Toyota, K.; Fukuda, R.; Hasegawa, J.; Ishida, M.; Nakajima, T.; Honda, Y.; Kitao, O.; Nakai, H.; Vreven, T.; Throssell, K.; Montgomery Jr., J. A.; Peralta, J. E.; Ogliaro, F.; Bearpark, M. J.; Heyd, J. J.; Brothers, E. N.; Kudin, K. N.; Staroverov, V. N.; Keith, T. A.; Kobayashi, R.; Normand, J.; Raghavachari, K.; Rendell, A. P.; Burant, J. C.; Iyengar, S. S.; Tomasi, J.; Cossi, M.; Millam, J. M.; Klene, M.; Adamo, C.; Cammi, R.; Ochterski, J. W.; Martin, R. L.; Morokuma, K.; Farkas, O.; Foresman, J. B.; Fox,

D. J. *Gaussian 16 Rev. B.01*, Wallingford, CT, 2016.

Chapter 3

Selective Metal-Phenolic Assembly from Complex Multicomponent Mixtures

3.1. Abstract

Selective self-assembly in multicomponent mixtures offers a method for isolating desired components from complex systems for the rapid production of functional materials. Developing approaches capable of selective assembly of "target" components into intended three-dimensional structures is challenging because of the intrinsically high complexity of multicomponent systems. Herein, I report the selective coordination-driven self-assembly of metal–phenolic networks (MPNs) from a series of complex multicomponent systems (including crude plant extracts) into thin films via metal chelation with phenolic ligands. The metal (Fe^{III}) selectively assembles low abundant phenolic components (e.g., myricetrin and quercetrin) from plant extracts into thin films. This selective metal–phenolic assembly is independent of the substrate properties (e.g., size, surface charge and shape). Moreover, the high selectivity of my method is consistent across different target phenolic ligands in model mixtures, even though each individual component can form thin films from single component systems. A computational simulation of film formation suggests that the driving force for the selective behavior stems from differences in the number of chelating sites in the phenolic structures. The MPN films are shown to demonstrate improved antioxidant properties compared with the corresponding phenolic compounds in their free form, therefore exhibiting potential as free-standing antioxidant films.

3.2. Introduction

Self-assembly in nature affords the formation of complex biological systems from multicomponent mixtures, in which individual components specifically assemble into ordered hierarchical structures.[1–4] For example, a wide variety of natural protein nanocages (e.g., ferritin, heat shock proteins, virus-like particles) are formed from the selective self-assembly of more than 20 subunits of precursors in complex multicomponent systems in living organisms.[5,6] These examples in nature have inspired the development of biomimetic approaches using self-assembly as a tool to construct functional synthetic materials for applications including drug delivery, sensing, and catalysis.[7-13] However, unlike nature, most of these approaches are limited to single-component systems,[9,11] as control over the self-assembly process in a multicomponent environment has remained challenging owing to the competing interactions of multiple building blocks.[14]

Selective self-assembly from complex multicomponent systems has the potential to provide new ways to engineer materials with unique properties, and has thus drawn widespread interest in recent years.[15,16] However, the development of selective approaches that can assemble “target” components into defined structures by negating competing interactions with other components within multicomponent systems is challenging.[17] Several selective assembly techniques have been developed (e.g., orthogonal self-assembly, dynamic imine chemistry).[18,19] Nitschke and Lehn combined imine chemistry and metal ion coordination to selectively generate metallo-supramolecular grid architectures in a mixture of different aminophenol and carbonyl components.[20] In another study, Yang and co-workers reported the selective assembly of complex tris[2]pseudorotaxanes based on orthogonal metal–ligand coordination and host–guest interactions.[21] However, these methods generally focused

on assembling complexes into nanoscale structures. To my knowledge, approaches for fabricating materials with higher order structures are rare.

Metal–phenolic assembly has been reported as a universal approach for the formation of hybrid films on diverse substrates.[22] A prominent feature of this assembly approach is its versatility in terms of phenolic ligands that can be used as building blocks, including tannic acid,[22] flavonoids,[23] small phenolic ligands,[24] synthetic polyphenols,[25–27] and tea infusions.[28] Herein, the metal–phenolic assembly technique is used to selectively assemble target phenolic compounds into higher order structures (e.g., thin films) from complex multicomponent systems of phenolic species. The results showed that iron ions (Fe^{III}) could produce thin films on particle templates via selective assembly of the target phenolic ligands of low abundance (<2%) from complex multicomponent systems (Scheme 3.1b), although both target and competitor phenolic ligands separately can be assembled into films via Fe^{III} coordination. The selectivity has been demonstrated using natural eucalyptus (Euc) leaf extracts and a model mixture of phenolic ligands, and was independent of the properties of the substrate examined (size, shape, and surface charge). A computational model suggests that the driving force of this selective behavior stems from differences in the number of chelating sites between the target and competitor phenolic ligands. Finally, the antioxidant properties of the metal–phenolic films is demonstrated. The selective MPN assembly thus provides a promising technique for isolating desired phenolic components from complex systems to rapidly prepare antioxidant films.

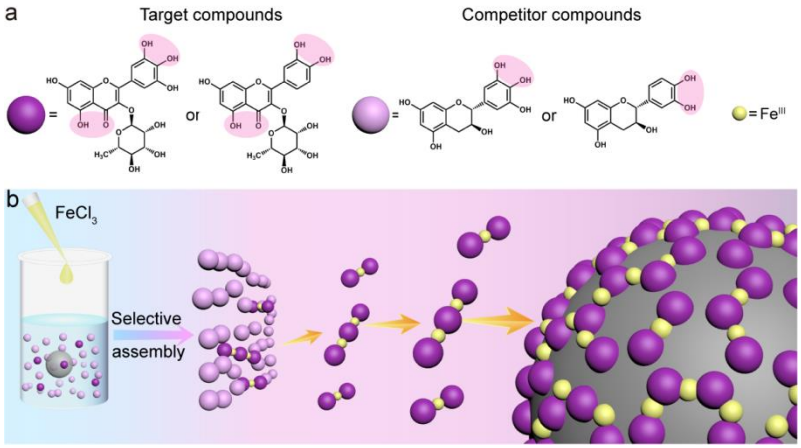

Scheme 3.1. (a) Molecular structures of target compounds (Myr and Quer) and competitor compounds (Cat and Gal); possible chelating sites for FeIII are highlighted in pink. (b) Schematic illustration of selective metal–phenolic assembly on a particle template in a complex multicomponent system.

3.3. Results and Discussion

Metal–phenolic assembly within a complex multicomponent system was first investigated using natural Euc leaf extracts. Euc extracts were chosen as the multicomponent system in the present study, as they are a rich source of different phenolic compounds including Myr, Quer, Gal, Cat, and chlorogenic acid (CA).[29,30] The extract was prepared from Euc leaves (specie: *Eucalyptus citriodora* or Lemon eucalyptus) by a conventional infusion method,[22] i.e., by incubating cut and washed leaves in Milli-Q water in an oven (85 ℃) for 12 h, as shown in Figure SI3.1. Over time, the original colorless suspension turned slightly yellow, indicating successful extraction of the phenolic compounds from the Euc leaves. LC–MS experiments were performed on the Euc extracts to identify the phenolic compounds present in the system. As shown in Figure 3.1a, the extract consisted of seven major phenolic compounds CA, Cat, apigenin-7-glucoside (AG), Gal, Myr, Quer, and isorhamnetin-3-O-glucoside (Isg). The chemical structures of these compounds are shown in Figure SI3.2, and Table SI3.1 summarizes their retention times, *m/z*, and

literature references for their identification.[29,31–33] Among the compounds identified, Gal was the most abundant (~50% area), whereas Myr and Quer were present in relatively smaller amounts in the Euc extract, as shown in Table SI3.1.

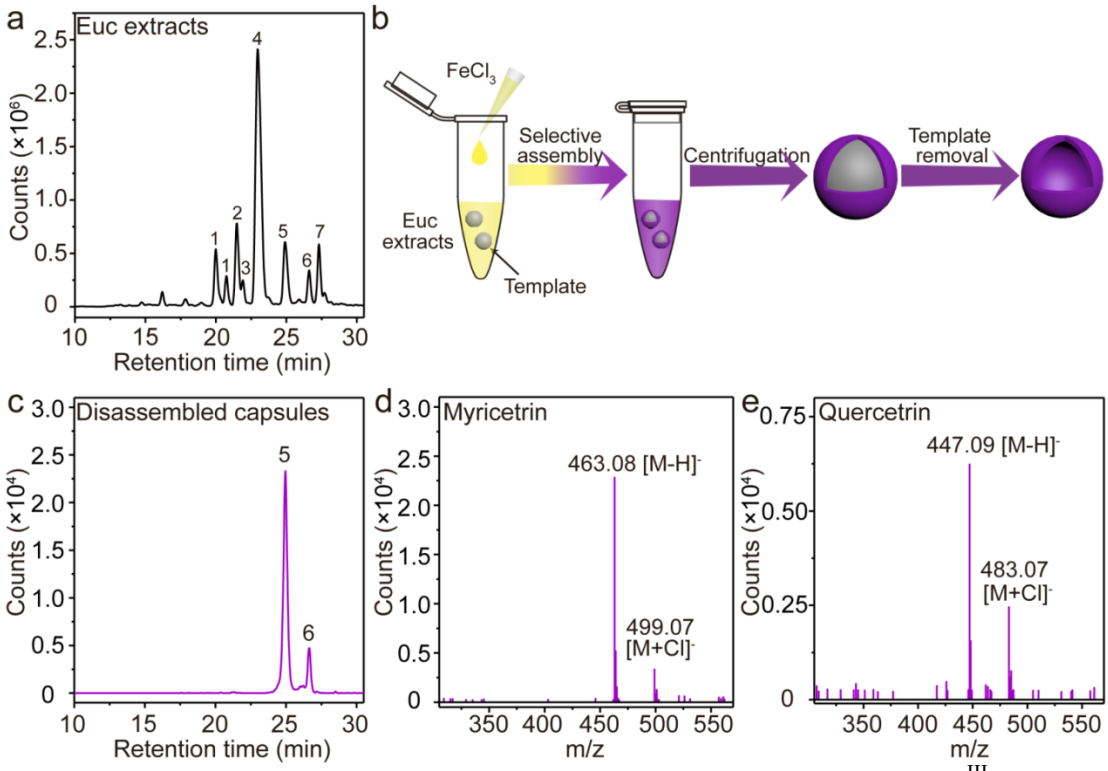

Figure 3.1. Preparation and characterization of Euc extracts and Euc/Fe^{III} capsules obtained by selective MPN assembly. (a) Combined extracted ion chromatograms (EICs) of the Euc extract showing retention times of the major compounds: (1) chlorogenic acid (CA); (2) catechin (Cat); (3) apigenin-7-glucoside (AG); (4) gallocatechin (Gal); (5) myricetrin (Myr); (6) quercetrin (Quer); and (7) isorhamnetin 3-O-glucoside (Isg). (b) Schematic illustration of capsule preparation from Euc extracts by selective assembly. (c) Combined EICs of CA (*m/z* 353.09), Cat (*m/z* 289.07), AG (*m/z* 431.19), Gal (*m/z* 305.07), Myr (*m/z* 463.09), Quer (*m/z* 447.09), Isg (*m/z* 477.23) in the disassembled capsules. Mass spectra of the detected compounds: (d) Myr and (e) Quer.

Using the Euc extract as a mixed phenolic source, MPN film formation was then investigated by a discrete assembly method (i.e., mixing phenolic ligands with an iron salt solution in the presence of template particles).[22] As shown in Figure 3.1b, Fe^{III} solution was added to the Euc extract solution containing PMMA particles (D = ~3.7 μm), and the pH of the mixture was adjusted to 5 (see *Experimental Section* for details). After mixing and subsequent washing in water, MPN film formation was

observed by the color darkening with template coating (Figure SI3.3). The templates were removed by using a mixed solution of NMP/acetone (1:1 v/v), resulting in stable and monodisperse Euc/Fe^{III} capsules, as observed in the DIC microscopy image in Figure 3.2a. The morphology of the monodisperse capsules was further examined by TEM analysis (Figure 3.2b). AFM analysis revealed monodisperse capsules with folds and creases that are typical features of collapsed capsules (Figure 3.2c).[28] Figure 3.2d compares the UV–vis spectra of the capsule suspension and the pure extract; a ligand-to-metal charge-transfer (LMCT) band was observed at 565 nm for the capsules, which corresponds to catechol/Fe^{III} coordination. EDX analysis (Figure 3.2e) confirmed the presence of Fe in the films. The oxidation state of iron in the capsules was further investigated by XPS. As shown in Figure 3.2f, the core-level spectra of Fe showed Fe $2p_{3/2}$ and Fe $2p_{1/2}$ signals at ~712 and ~725 eV respectively, suggesting that Fe^{III} was the dominant species in the capsules.

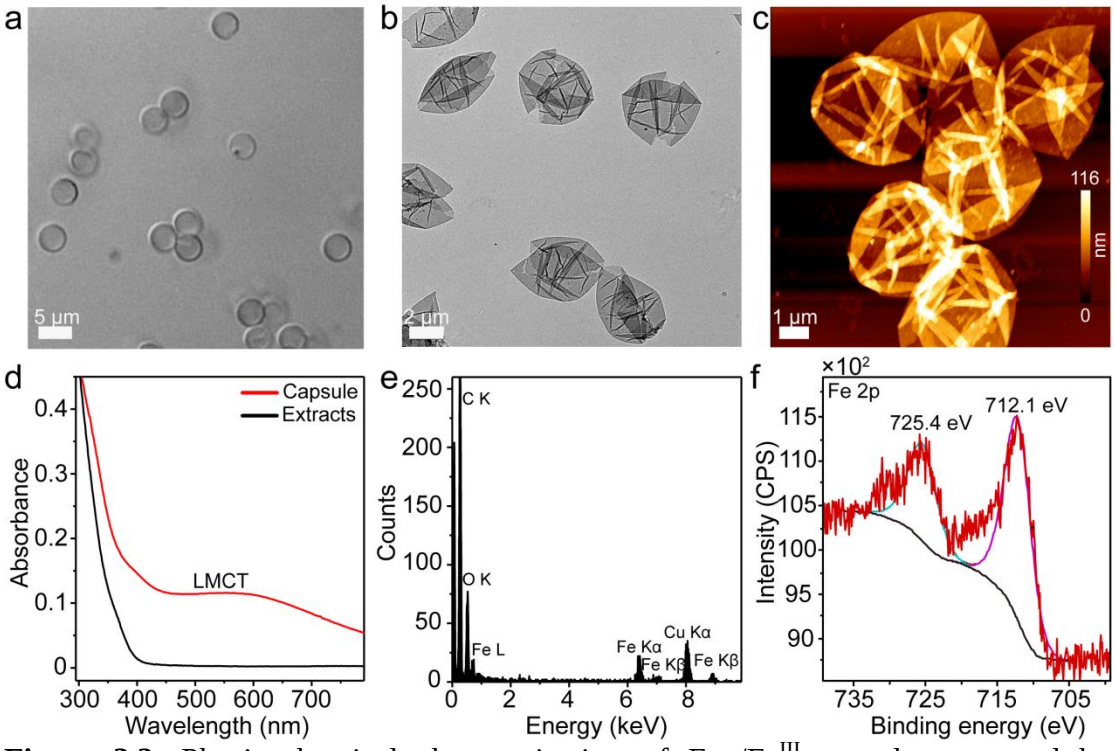

Figure 3.2. Physicochemical characterization of Euc/Fe^{III} capsules prepared by selective metal–phenolic assembly from Euc extracts. (a) DIC microscopy, (b) TEM, and (c) AFM images of the Euc/Fe^{III} capsules. (d) UV−Vis absorption spectra of the Euc extracts and Euc/Fe^{III} capsule suspension. (e) EDX and (f) XPS spectra of the

Euc/Fe^{III} capsules.

To investigate the molecular composition of the Euc/Fe^{III} film, the capsules were disassembled and the components were subjected to LC–MS analyses. Figure 3.1c shows a combined EICs of the disassembled capsules, where the retention times for the two major peaks were found to be 24.9 and 26.7 min. These peaks were assigned to Myr and Quer respectively by comparing their retention times and MS signals (Figure 3.1d, e) with their commercial standards (Figure SI3.4). Thus, despite their relatively low abundance, Myr and Quer were found to be the major components of the capsules, suggesting the selective behavior of the metal–phenolic assembly in the Euc leaf extract into thin films. The concentrations of Myr and Quer in the extracts were 67.4 and 20.3 μg mL^{-1}, respectively, using the LC–MS standard curves in Figure SI3.5, whereas their concentrations in the capsules were determined to be 0.33 and 0.04 pg per capsule. The Myr-to-Quer mass ratio in the capsules was higher than that in the starting extract (8.2 vs 3.3).

The versatility of the present selective assembly method to form MPN films on various substrates with different sizes, structures, surface charge, and shapes (Figure 3.3a) was also examined. Metal–phenolic film formation was observed on PMMA particles (~100 nm), mesoporous silica particles (~800 nm, negatively charged, synthesized by the reported method[29]), aminated silica particles (~2.8 μm, positively charged), and planar quartz substrates (1 cm × 3 cm), as indicated by the color darkening with substrate coating (Figure 3.3b). When the Euc/Fe^{III} films on these substrates were disassembled and analyzed by LC–MS, two major peaks corresponding to Myr and Quer (Figure SI3.6) were observed in the spectra, indicating that the selective metal–phenolic assembly for film formulation was independent of substrate properties. The Myr-to-Quer ratio in the films depended on

the substrates (Table SI3.2), possibly because the substrate surface properties impact the adsorption of different MPN complexes. The versatility of the selective MPN assembly is probably due to the high affinity of catechol-functionalized molecules and derivatives towards various substrates with different surface properties.[22]

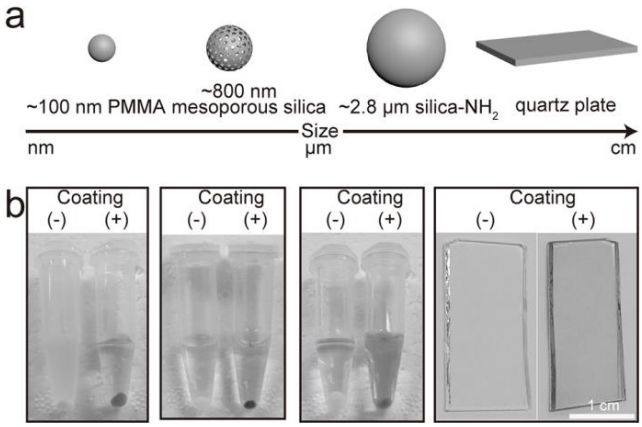

Figure 3.3. (a) Types of substrates investigated for selective MPN assembly: ~100 nm PMMA particles, ~800 nm mesoporous silica particles, ~2.8 μm aminated silica particles, and 1 cm × 3 cm quartz plate. (b) Photographs of the substrates (–) and MPN-coated substrates (+) obtained by selective MPN assembly.

To gain further insight into this selective metal–phenolic assembly, the assembly experiments were performed using a model phenolic mixture containing Myr, Gal, and Cat (molar ratio of 1:1:1) that mimicked the Euc extract. Myr was the major phenolic component in the assembled films, whereas Gal and Cat were the major components of the starting Euc extract. Note that these three ligands could form MPN films from single-component systems (i.e., where only one type of phenolic ligand is present in the system) as shown in Figure SI3.7, which was in agreement with the previous finding that phenolic compounds possessing at least one catechol group are capable of forming metal–phenolic films.[24] Fe^{III} solution was added to the model multicomponent mixture containing the above three ligands to prepare the MPN films on PMMA particles (D = ~3.7 μm). The obtained films on PMMA particles were then disassembled and analyzed by LC–MS. Figure 3.4a shows a combined EICs of the disassembled capsules prepared from the model phenolic mixture. The major peak

observed at a retention time of 24.9 min corresponds to Myr (Figure 3.4b), and no trace signals of Cal and Cat were observed. Thus, Fe^{III} can selectively assemble Myr in the model mixture into thin films similar to that observed in the natural Euc extract. To confirm the selectivity further, the concentration of the competing phenolic ligands in the mixture was increased (Myr/Ca/Gal = 1:25:25) such that the Myr molar composition was <2%. Likewise, the resulting films featured Myr as the dominant phenolic component (Figures SI3.8 and SI3.9), demonstrating selectivity of the assembly even with a low abundant target ligand.

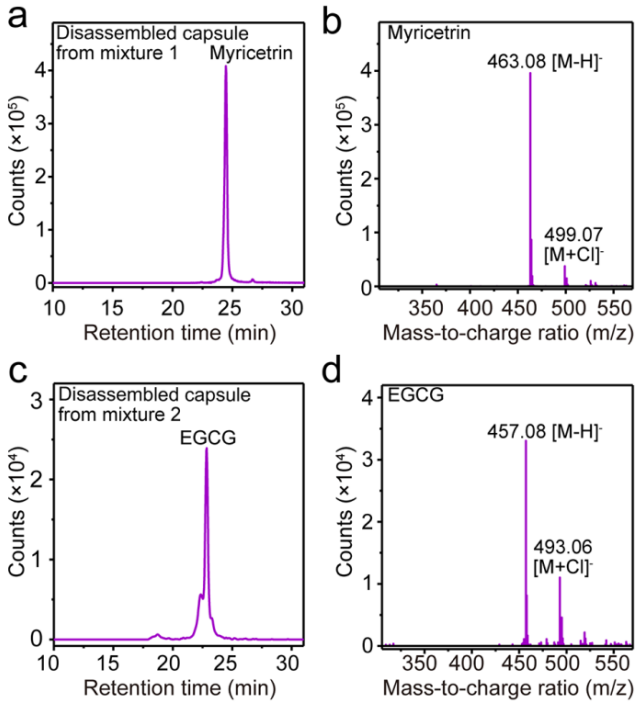

Figure 3.4. Selective metal–phenolic assembly in model phenolic mixtures. (a) Combined EICs of Cat (*m/z* 289.07), Gal (*m/z* 305.07), Myr (*m/z* 463.09) in disassembled capsules formed by selective assembly from a mixture containing Myr, Cat, and Gal (Mixture 1). (b) Mass spectra of the detected compound (Myr) in capsules obtained from Mixture 1. (c) Combined EICs of Cat (*m/z* 289.07), Gal (*m/z* 305.07), EGCG (*m/z* 457.08) in disassembled capsules formed by selective assembly from a mixture containing, Cat, Gal, and EGCG (Mixture 2). (d) Mass spectra of the detected compound (EGCG) in capsules obtained from Mixture 2.

Previous studies have shown that the number of chelating sites on ligands can impact on the ability of the ligand to form coordination-driven materials.[34,35] For example, conventional coordination polymer particles are generally synthesized using

bifunctional ligand precursors.[34] In the present case, the most significant difference between the structure of the target and competitor phenolic compounds was the number of possible Fe^{III} chelating sites (shaded in pink in Scheme 3.1a and Figure SI3.2). From this information, I hypothesize that the number of chelating sites on the phenolic compound is a possible reason for the selective assembly observed in complex multicomponent systems. Both the target and competitor ligands can form metal–phenolic complexes at the early stages of the reaction (Figure 3.5a). As the reaction proceeds, the target ligands with two chelating sites can grow and form large extendable networks. Owing to the higher number of sites in such networks, surface adsorption and simultaneous cross-linking is more favored than in smaller-sized competitor complexes obtained from compounds with fewer chelating sites.

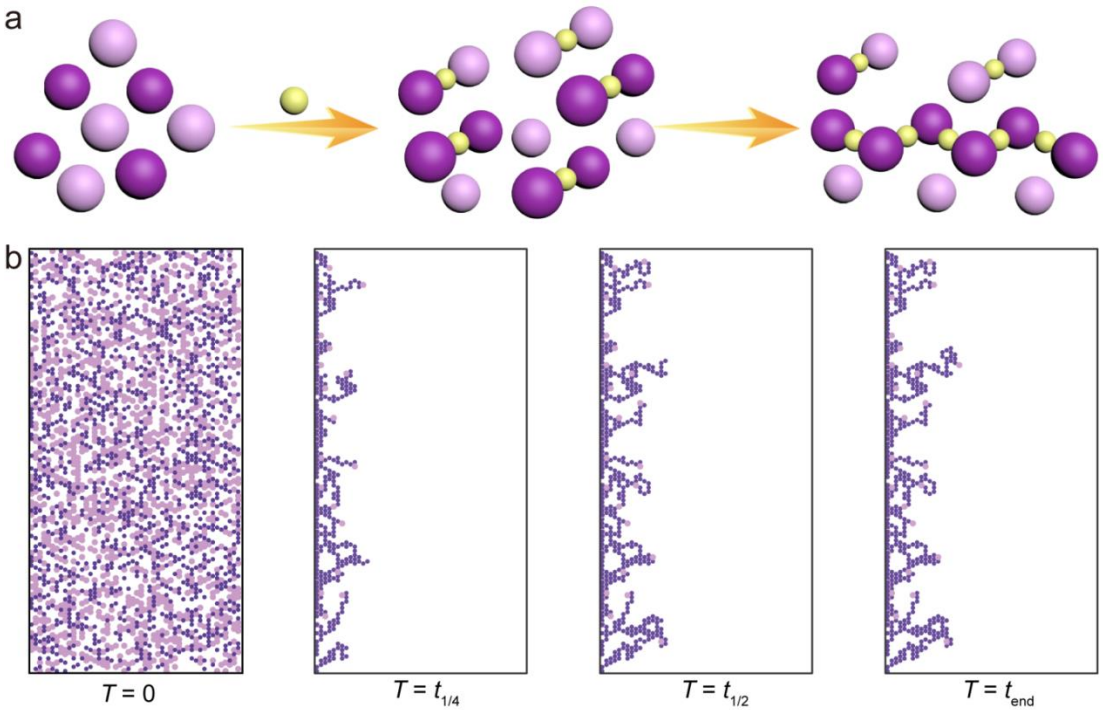

Figure 3.5. Proposed mechanism and computer modeling of selective MPN assembly. (a) Schematic illustration of the formation of large extendable target compound/Fe^{III} complexes in the presence of small competitor/Fe^{III} complexes. (b) Computer modeling of selective MPN assembly, in which target compounds with two chelating sites (purple) and competitor compounds with one chelating site (pink) randomly chelate Fe^{III} and deposit onto the substrate. At the start of the assembly (T = 0), the system contains an equal number of unbound (free) target compound and competitor. At different time points ($T = t_{1/4}$, $t_{1/2}$, and t_{end}), free compounds that are not bound to the left boundary (template) are removed, resulting in the film, which preferably

grows with the extendable target compounds that bear a higher number of chelating sites.

To further examine this hypothesis, a computational model simulating the interaction between target phenolic (purple) compounds with two chelating sites or competitor compounds with a single chelating site (pink) and Fe^{III} ions was constructed. All three species in the model undergo random motion. The left boundary of the lattice sites represents the template. The target and competitor phenolic compounds share a similar binding affinity to Fe^{III}. The target phenolic compounds can chelate two Fe^{III} ions and further bind to other target phenolic compounds or competitors from two sites, provided that a free chelating site remains for both compounds. In comparison, competitors can only chelate one Fe^{III} ion, which then binds to target phenolic compounds or other competitors. The model simulation revealed that the film grew with time and that the target phenolic compounds (purple) were the dominant component of the growing film. This selective assembly was time-independent, as observed at points $t_{1/4}$, $t_{1/2}$, and t_{end} (Figure 3.5b). This result agrees with my experimental data and the above hypothesis, indicating that despite target and competitor phenolic compounds having similar binding affinities to Fe^{III}, the difference in the number of Fe^{III} chelating sites likely contributes to selective metal–phenolic assembly into thin films. I infer this as the ligands with a higher number of chelation sites are more likely to form the extendable complexes to promote ligand-surface interactions and simultaneous coordination cross-linking for MPN film formation.

To confirm whether this selective assembly is generic or case-specific, the target phenolic ligand was changed from Myr to EGCG (structure shown in Figure SI3.10), as it also possesses two chelation sites but a different structure. Thus, the phenolic mixture contained EGCG, Cat, and Gal at a molar ratio of EGCG/Cat/Gal 1:1:1.

When the resulting films were disassembled and analyzed by LC–MS, the major phenolic component in the films was found to be EGCG, as shown in Figure 3.4c and d. This result also supports the hypothesis that the difference in the number of chelating sites likely determines the selective assembly of the phenolic ligands into thin films from a complex multicomponent system. The selective assembly reported herein can provide several benefits: it offers a route for forming thin films, comprising one or two components with unique properties, from a complex multicomponent system, irrespective of substrate properties, and it allows the utilization of low-cost (or freely available) crude natural mixtures to fabricate functional materials with defined composition.

Finally, the antioxidant properties of the selectively assembled films (from Euc extract) were examined on the basis of their radical scavenging ability. DPPH assays were used, which measure the reduction in the absorbance of the radical DPPH at 515 nm or a color change from purple to yellow in the presence of an antioxidant compound.[23,36] When the Euc/Fe^{III}-coated PMMA particles were added to ethanolic DPPH solution, a color change from purple to yellow was observed (Figure SI3.11), indicating the reduction of the DPPH radicals (Figure SI3.12). Figure 3.6a shows that the characteristic absorption peak of DPPH at 515 nm significantly decreased upon addition of the film to the ethanolic DPPH solution, indicating that the film can scavenge the free radicals. EC50 (i.e., antioxidant concentration at which 50% radical DPPH scavenging occurs) was measured for the films as well as for an equivalent mixture of free Myr and Quer (Myr/Quer at mass ratio of 8.3:1) by plotting radical scavenging activity against concentration (Figure SI3.13).[37] As observed in Figure 3.6b, the equivalent mixture of free Myr and Quer displayed an EC50 of 17.5 μM, whereas the films featured a lower EC50 of 16.4 μM, indicating the slightly improved

antioxidant behavior obtained in the presence of capsules when compared with the corresponding free phenolic compounds. The improvement could possibly be due to the iron center that can stabilize the semiquinone radical intermediate (Figure SI3.14).[23,38] In addition, the Euc/Fe^{III}-coated PMMA particles could be used in consecutive cycles as investigated by subjecting the particles to three DPPH scavenging cycles. The first cycle resulted in almost complete DPPH depletion. After washing the particles in ethanol, the Euc/Fe^{III}–coated PMMA particles could still scavenge ~70% DPPH, and after the third cycle, 50% DPPH radical depletion was observed (Figure 3.6c). In summary, the selectively assembled MPN films displayed enhanced and antioxidant capacity in consecutive cycles, and thus may be applied as particle- or film-based radical scavenging agents.

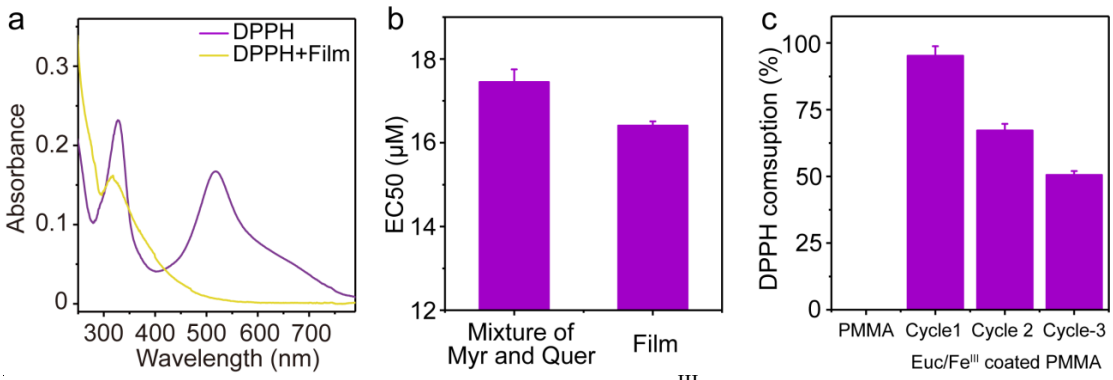

Figure 3.6. Radical scavenging ability of Euc/Fe^{III} films. (a) UV–Vis spectra of DPPH (30 μM in ethanol) and the supernatant collected from DPPH treated with films. (b) EC50 of Euc/Fe^{III}-coated PMMA particles and equivalent mixture of Myr and Quer. (c) Repeated radical scavenging activity of the Euc/Fe^{III}-coated PMMA particles over three cycles of incubation (20 min) with intermediate washing steps; bare PMMA particles were also tested as a control.

3.4. Conclusion

I have shown the selective self-assembly between Fe^{III} and phenolic ligands on various substrates from complex plant polyphenol mixtures. The present selective metal–phenolic assembly can recognize small variations in the number of possible

chelating sites between different phenolic compounds. The assembly is robust and versatile—the same phenomenon was observed in model mixtures of commercial phenolic compounds and crude natural extracts such as Euc leaf extracts and the assembly could be performed on various substrates with different size, shape, and surface properties. The high selectivity of this approach and its applicability to various phenolic mixtures make it a potentially powerful tool for pharmaceutical separation, whereby specific compounds need to be isolated from complex mixtures. Finally, the films obtained from selective metal–phenolic assembly exhibit improved radical scavenging properties in consecutive cycles (when compared with free phenolic compounds), rendering them a potential candidate for antioxidant application.

3.5. References

1. Whitesides, G. M.; Grzybowski, B. Self-Assembly at All Scales. *Science* **2002**, *295*, 2418–2421.

2. Mattia, E.; Otto, S. Supramolecular Systems Chemistry. *Nat. Nanotechnol*. **2015**, *10*, 111–119.

3. Ariga, K.; Nishikawa, M.; Mori, T.; Takeya, J.; Shrestha, L. K.; Hill, J. P. Self-Assembly as a Key Player for Materials Nanoarchitectonics. *Sci. Technol. Adv. Mater*. **2019**, *20*, 51–95.

4. Hiraoka, S. Unresolved Issues that Remain in Molecular Self-Assembly. *Bull. Chem. Soc. Jpn*. **2018**, *91*, 957–978.

5. Lee, E. J.; Lee, N. K.; Kim, I.-S. Bioengineered Protein-Based Nanocage for Drug Delivery. *Adv. Drug Delivery Rev.* **2016**, *106*, 157–171.

6. Murata, S.; Yashiroda, H.; Tanaka, K. Molecular Mechanisms of Proteasome Assembly. *Nat. Rev. Mol. Cell Biol.* **2009**, *10*, 104–115.

7. Pattni, B. S.; Chupin, V. V.; Torchilin, V. P. New Developments in Liposomal Drug Delivery. *Chem. Rev.* **2015**, *115*, 10938–10966.

8. Cabral, H.; Miyata, K.; Osada, K.; Kataoka, K. Block Copolymer Micelles in Nanomedicine Applications. *Chem. Rev.* **2018**, *118*, 6844–6892.

9. Yan, X.; Zhu, P.; Li, J. Self-Assembly and Application of Diphenylalanine-Based Nanostructures. *Chem. Soc. Rev.* **2010**, *39*, 1877–1890.

10. Zhu, L.; Liu, X.-Q.; Jiang, H.-L.; Sun, L.-B. Metal–Organic Frameworks for Heterogeneous Basic Catalysis. *Chem. Rev.* **2017**, *117*, 8129–8176.

11. Bucknall, D. G.; Anderson, H. L. Polymers Get Organized. *Science* **2003**, *302*, 1904–1905.

12. Furukawa, H.; Cordova, K. E.; O'Keeffe, M.; Yaghi, O. M. The Chemistry and

Applications of Metal-Organic Frameworks. *Science* **2013**, *341*, 1230444.

13. Liu, S.; Tang, Z. Nanoparticle Assemblies for Biological and Chemical Sensing. *J. Mater. Chem.* **2010**, *20*, 24–35.

14. Pappas, C. G.; Shafi, R.; Sasselli, I. R.; Siccardi, H.; Wang, T.; Narang, V.; Abzalimov, R.; Wijerathne, N.; Ulijn, R. V. Dynamic Peptide Libraries for the Discovery of Supramolecular Nanomaterials. *Nat. Nanotechnol.* **2016**, *11*, 960–967.

15. Okesola, B. O.; Mata, A. Multicomponent Self-Assembly as a Tool to Harness New Properties from Peptides and Proteins in Material Design. *Chem. Soc. Rev.* **2018**, *47*, 3721–3736.

16. Liu, Y.; Liu, B.; Nie, Z. Concurrent Self-Assembly of Amphiphiles into Nanoarchitectures with Increasing Complexity. *Nano Today* **2015**, *10*, 278–300.

17. Jacobs, W. M.; Frenkel, D. Self-Assembly of Structures with Addressable Complexity. *J. Am. Chem. Soc.* **2016**, *138*, 2457–2467.

18. Hu, X.-Y.; Xiao, T.; Lin, C.; Huang, F.; Wang, L. Dynamic Supramolecular Complexes Constructed by Orthogonal Self-Assembly. *Acc. Chem. Res.* **2014**, *47*, 2041–2051.

19. Belowich, M. E.; Stoddart, J. F. Dynamic Imine Chemistry. *Chem. Soc. Rev.* **2012**, *41*, 2003–2024.

20. Nitschke, J. R.; Lehn, J.-M. Self-Organization by Selection: Generation of a Metallosupramolecular Grid Architecture by Selection of Components in a Dynamic Library of Ligands. *Proc. Natl. Acad. Sci. U. S. A.* **2003**, *100*, 11970–11974.

21. Wang, W.; Zhang, Y.; Sun, B.; Chen, L.-J.; Xu, X.-D.; Wang, M.; Li, X.; Yu, Y.; Jiang, W.; Yang, H.-B. The Construction of Complex Multicomponent Supramolecular Systems via the Combination of Orthogonal Self-Assembly and the Self-Sorting Approach. *Chem. Sci.* **2014**, *5*, 4554–4560.

22. Ejima, H.; Richardson, J. J.; Liang, K.; Best, J. P.; van Koeverden, M. P.; Such, G. K.; Cui, J.; Caruso, F. One-Step Assembly of Coordination Complexes for Versatile Film and Particle Engineering. *Science* **2013**, *341*, 154–157.

23. Bertleff-Zieschang, N.; Rahim, M. A.; Ju, Y.; Braunger, J. A.; Suma, T.; Dai, Y.; Pan, S.; Cavalieri, F.; Caruso, F. Biofunctional Metal–Phenolic Films from Dietary Flavonoids. *Chem. Commun.* **2017**, *53*, 1068–1071.

24. Rahim, M. A.; Kempe, K.; Müllner, M.; Ejima, H.; Ju, Y.; van Koeverden, M. P.; Suma, T.; Braunger, J. A.; Leeming, M. G.; Abrahams, B. F.; Caruso, F. Surface-Confined Amorphous Films from Metal-Coordinated Simple Phenolic Ligands. *Chem. Mater.* **2015**, *27*, 5825–5832.

25. Ju, Y.; Cui, J.; Müllner, M.; Suma, T.; Hu, M.; Caruso, F. Engineering Low-Fouling and pH-Degradable Capsules through the Assembly of Metal-Phenolic Networks. *Biomacromolecules* **2015**, *16*, 807–814.

26. Ju, Y.; Cui, J.; Sun, H.; Müllner, M.; Dai, Y.; Guo, J.; Bertleff-Zieschang, N.; Suma, T.; Richardson, J. J.; Caruso, F. Engineered Metal-Phenolic Capsules Show Tunable Targeted Delivery to Cancer Cells. *Biomacromolecules* **2016**, *17*, 2268–2276.

27. Besford, Q. A.; Ju, Y.; Wang, T.-Y.; Yun, G.; Cherepanov, P.; Hagemeyer, C. E.; Cavalieri, F.; Caruso, F. Self-Assembled Metal–Phenolic Networks on Emulsions as Low-Fouling and pH-Responsive Particles. *Small* **2018**, *14*, 1802342.

28. Rahim, M. A.; Björnmalm, M.; Bertleff-Zieschang, N.; Ju, Y.; Mettu, S.; Leeming, M. G.; Caruso, F. Multiligand Metal–Phenolic Assembly from Green Tea Infusions. *ACS Appl. Mater. Interfaces* **2018**, *10*, 7632–7639.

29. Santos, S. A. O.; Freire, C. S. R.; Domingues, M. R. M.; Silvestre, A. J. D.; Neto, C. P. Characterization of Phenolic Components in Polar Extracts of *Eucalyptus globulus* Labill. Bark by High-Performance Liquid Chromatography–Mass

Spectrometry. *J. Agric. Food Chem.* **2011**, *59*, 9386–9393.

30. Mota, I.; Rodrigues Pinto, P. C.; Novo, C.; Sousa, G.; Guerreiro, O.; Guerra, Â. R.; Duarte, M. F.; Rodrigues, A. E. Extraction of Polyphenolic Compounds from *Eucalyptus globulus* Bark: Process Optimization and Screening for Biological Activity. *Ind. Eng. Chem. Res.* **2012**, *51*, 6991–7000.

31. Hossain, M. B.; Rai, D. K.; Brunton, N. P.; Martin-Diana, A. B.; Barry-Ryan, C. Characterization of Phenolic Composition in Lamiaceae Spices by LC-ESI-MS/MS. *J. Agric. Food Chem.* **2010**, *58*, 10576–10581.

32. de Brito, E. S.; Pessanha de Araújo, M. C.; Lin, L.-Z.; Harnly, J. Determination of the Flavonoid Components of Cashew Apple (*Anacardium occidentale*) by LC-DAD-ESI/MS. *Food Chem.* **2007**, *105*, 1112–1118.

33. Chen, Y.; Yu, H.; Wu, H.; Pan, Y.; Wang, K.; Jin, Y.; Zhang, C. Characterization and Quantification by LC-MS/MS of the Chemical Components of the Heating Products of the Flavonoids Extract in Pollen Typhae for Transformation Rule Exploration. *Molecules* **2015**, *20*, 18352–18366.

34. Spokoyny, A. M.; Kim, D.; Sumrein, A.; Mirkin, C. A. Infinite Coordination Polymer Nano- and Microparticle Structures. *Chem. Soc. Rev.* **2009**, *38*, 1218–1227.

35. Novio, F.; Simmchen, J.; Vázquez-Mera, N.; Amorín-Ferré, L.; Ruiz-Molina, D. Coordination Polymer Nanoparticles in Medicine. *Coord. Chem. Rev.* **2013**, *257*, 2839–2847.

36. Deligiannakis, Y.; Sotiriou, G. A.; Pratsinis, S. E. Antioxidant and Antiradical SiO_2 Nanoparticles Covalently Functionalized with Gallic Acid. *ACS Appl. Mater. Interfaces* **2012**, *4*, 6609–6617.

37. Cherrak, S. A.; Mokhtari-Soulimane, N.; Berroukeche, F.; Bensenane, B.; Cherbonnel, A.; Merzouk, H.; Elhabiri, M. In Vitro Antioxidant versus Metal Ion

Chelating Properties of Flavonoids: A Structure–Activity Investigation. *PLoS One* **2016**, *11*, e0165575.

38. Moridani, M. Y.; Pourahmad, J.; Bui, H.; Siraki, A.; O'Brien, P. J. Dietary Flavonoid Iron Complexes as Cytoprotective Superoxide Radical Scavengers. *Free Radical Biol. Med.* **2003**, *34*, 243–253.

3.6. Supporting Information

Materials

Myricetrin (Myr), quercetrin (Quer), and gallocatechin (Gal) were purchased from Carbosynth Pty Ltd (United Kingdom). Catechin (Cat), epigallocatechin gallate (EGCG), iron(III) chloride hexahydrate, poly(diallyldimethylammonium chloride) (PDAC), 2,2′-diphenyl-picrylhydrazyl (DPPH), and *N*-methyl-2-pyrrolidone (NMP) were obtained from Sigma-Aldrich (USA). Poly(methyl methacrylate) (PMMA) particles (D = 105 ± 4 nm and 3.69 ± 0.08 μm) and aminated silica microparticles (2.79 ± 0.12 μm) were purchased from microParticles GmbH (Germany). Quartz plates were purchased from ProSciTech (Australia). Sodium hydroxide (NaOH) and acetone were obtained from Chem-Supply (Australia). Mature Euc leaves were collected from an Eucalyptus tree on The University of Melbourne, Parkville campus, Australia.

Preparation of Euc Leaf Extracts

Mature Euc leaves (35 pieces, weight: 25–30 g) were washed with tap water and then with Milli-Q water at least three times to remove dust. The washed leaves were cut into small pieces (approximately 1 cm × 2 cm), placed in 400 mL Milli-Q water, and incubated in an oven at 85 ℃ for 12 h. After cooling to room temperature (20–25 ℃), the extract suspension (Euc extract) was filtered through a membrane filter (pore size: 0.8 μm) and stored at 4 °C until further use.

Metal–Phenolic Assembly onto Various Substrates Using Euc Extracts

The preparation of capsules from Euc extracts and iron solution was performed using ~3.7 μm PMMA colloidal templates following a previously reported method.[1] Briefly, 500 μL Euc extract was pipetted into a 1.5 mL tube, followed by the addition of 50 μL of 10% w/v PMMA particle templates. After vortex mixing for 15 s, 50 μL

$FeCl_3$ $6H_2O$ solution (24 mM) was added to the tube, and the mixture was vortexed for another 15 s. Subsequently, the pH of the mixture was adjusted to 5 by the addition of NaOH solution (0.5 M), followed by vortex mixing for 30 s. Finally, the PMMA templates were removed by washing with 500 μL NMP/acetone (1:1 v/v) four times. The Euc/Fe^{III} capsules were resuspended in 100 μL Milli-Q water for further use.

Coating of the ~100 nm PMMA particles was carried out using the same protocol as that described above but without template removal.

Coating on ~800 nm mesoporous silica particles (synthesized by the reported method[2]) and ~2.8 μm aminated silica were also performed as described above but without template removal and using 2 mg (in 50 μL water) of silica particles as templates.

Quartz substrates were also examined as planar substrates. Firstly, a quartz plate (1 cm × 3 cm) was cleaned by Piranha solution (3:1 H_2SO_4/H_2O_2) for 20 min. *Caution! Piranha solution is highly corrosive. Extreme care should be taken when handling Piranha solution and only small quantities should be prepared.* After drying in a stream of nitrogen, the quartz plate was incubated with PDAC/NaCl solution (2 mg mL^{-1}) for 10–20 min at room temperature (20–25 ℃) to obtain a positively charged substrate, and then rinsed with Milli-Q water. The precoated quartz plate was placed in a 50 mL tube, into which 10 mL Euc extract was introduced. After vortexing for 30 s, 1 mL $FeCl_3$ $6H_2O$ solution (24 mM) was added and the tube was vortexed for 30 s. The pH of the mixture was then adjusted to 5 by adding NaOH solution (0.5 M), and the tube was vortexed for 30 s. The coating process was repeated three times. Finally, the coated plate was rinsed and stored in Milli-Q water for characterization.

Preparation of Capsules Using Single-Component Systems

The preparation of capsules using the phenolic ligands Cat or Gal (Cat/Fe^{III} or Gal/Fe^{III}) was performed as previously reported.[3] Cat or Gal solution (500 μL, 15 mM) was added to a 1.5 mL tube containing 50 μL of PMMA particles (~3.7 μm, 10% w/v) in water. Then, 200 μL $FeCl_3$ $6H_2O$ (30 mM) was added to the mixture, followed by gentle vortex mixing for 15 s. Subsequently, the pH of the mixture was adjusted to 5 by the addition of NaOH solution (0.5 M), followed by vortex mixing for 30 s. Finally, the PMMA templates were removed by washing with 500 μL NMP/acetone (1:1 v/v) four times. The capsules were resuspended in 100 μL Milli-Q water for further use.

The preparation of Myr/Fe^{III} capsules was performed using the above method with minor modifications. Briefly, 500 μL Myr solution (0.2 mM) was added to a 1.5 mL tube containing 50 μL of PMMA particles (~3.7 μm, 10% w/v) in water. Then, 50 μL $FeCl_3$ $6H_2O$ (2 mM) was added to the mixture, followed by gentle vortex mixing for 15 s. Subsequently, the pH of mixture pH was adjusted to 5 by the addition of NaOH solution (0.1 M). The coating cycle was repeated four times before template removal.

Characterization

Differential interference contrast (DIC) microscopy images of Euc/Fe^{III} capsules were taken on an inverted Olympus IX71 microscope. Ultraviolet−visible (UV−vis) absorption spectra were recorded on a SPECORD 250 PLUS UV−vis spectrophotometer. Atomic force microscopy (AFM) measurements were performed on a JPK NanoWizard II BioAFM. Scans were recorded in tapping mode using MikroMasch silicon cantilevers (NSC/CSC). Morphology and element distribution determination were performed by transmission electron microscopy (TEM) and energy-dispersive X-ray spectroscopy (EDX) on a FEI Tecnai TF20 instrument at an operation voltage of 200 kV. For the sample preparation for the AFM and TEM/EDX experiments, 5 μL capsule suspensions were allowed to air dry on glass slides

(pretreated with Piranha solution) and Formvar carbon-coated copper grids, respectively. X-ray photoelectron spectroscopy (XPS) analysis was conducted on a VG ESCALAB220i-XL spectrometer equipped with a hemispherical analyzer. The energy calibration of XPS was referenced to the C 1s peak at 285.0 eV.

Liquid Chromatography−Mass Spectrometry (LC–MS) Studies

The organic components of the MPN films were analyzed by LC–MS after disassembling the films. The disassembly process was as follows:[1] 100 μL of concentrated Euc/Fe^{III}-coated particle suspensions (3×10^7 particles mL^{-1}, determined by flow cytometry) was mixed with 500 μL HCl (6 M), vortexed for 1 min, and kept on a rotating mixer for 10 min. After centrifugation of the HCl-treated suspensions, the supernatants were collected and diluted with 1 mL of Milli-Q water and lyophilized to remove excess HCl. The lyophilized samples were resuspended in 800 μL acidified methanol (1 mM) and filtered using a membrane filter (0.8 μm) before LC–MS analyses.

LC–MS analyses were performed on a liquid chromatography system (Agilent 1200 series) with an Agilent 6520 quadrupole time-of-flight mass spectrometer. For each analysis, 5 μL of sample (i.e., diluted Euc extracts, Myr (2 μg mL^{-1} in H_2O), Quer (2 μg mL^{-1} in H_2O), or disassembled capsules) was injected into the system, in which each compound was separated on a reverse phase column (150 mm (length) × 4.6 nm (internal diameter); 5 μm silica particles; Agilent ZORBAX Eclipse XDB C18), with 100% Milli-Q water as mobile phase A and 70% acetonitrile in 0.1% formic acid (v/v) as mobile phase B. Detailed parameters can be obtained from our previously reported work.[1] Electrospray mass spectra were recorded in negative ionization mode over a mass range *m/z* 100–1000.

A base peak chromatogram of *m/z* 200–1000 was employed to identify compounds

in the Euc leaf extracts and disassembled capsules, as the *m/z* ratios of many phenolic compounds are in that range. Combined extracted ion chromatograms (EICs) were used to compare the phenolic compounds detected in disassembled capsules with those in the Euc leaf extracts and model phenolic mixtures.

Modeling

We developed a simulation to mimic the MPN film formation process, according to our published lattice-based random walk model.[4] Rather than considering a single type of phenolic compound, in the simulation mimicking the experiments in this work, we include both a target phenolic compound (purple) and a competitor compound with a single chelating site (pink). In the model, it is assumed that the target phenolic compound has a similar binding constant to that of the competitor compound. Both the target phenolic compound and the competitor compound move randomly and may occupy a particular site in the lattice. Compounds in the simulation undergo random motion on a hexagonal lattice and can undergo binding events with other compounds upon contact, provided there are free chelating sites on both compounds and Fe^{III} is present in between the two compounds. Once a compound in the simulation binds to another one (pink) or two (purple) compounds, it is unable to undergo further binding events. We consider an Fe^{III}/purple/pink ratio of 1:1:1 to observe film growth in the mixture containing equal amounts of target and competitor compounds. During the assembly process, any compound that has reached the left boundary of the lattice sites is bound to the substrate and can no longer move. Fe^{III} ions will move and bind to available chelating sites randomly and participate in further binding events. The thickness of the film as a function of time was monitored during the simulation.

DPPH Assays

A DPPH assay was performed to evaluate the radical scavenging ability

(antioxidant property) of the Euc/Fe^{III} films. DPPH was freshly prepared before the experiments. Different amounts of Euc/Fe^{III}-coated PMMA particles (~3.7 μm) as well as a phenolic mixture containing equivalent amounts of Myr and Quer were added to 1 mL DPPH ethanolic solution (125 μM). After incubation for 20 min and centrifugation (2000 *g*, 1 min), 200 μL supernatant was withdrawn and introduced into a 96-well plate for analysis. The absorbance at 515 nm was measured. The percentage of remaining DPPH was determined and plotted against the concentration of capsules or Myr/Quer mixture to determine EC50 (concentration of the antioxidant agent required to deplete 50% of the initial amount of DPPH).

To study the antioxidant properties of the capsules at repeated use or cycles, the final concentration of DPPH was fixed at 60 μM by mixing 90 μL DPPH ethanolic solution (700 μM), 780 μL ethanol, and 30 μL Euc/Fe^{III}-coated PMMA particles (~3.7 μm). The number of Euc/Fe^{III}-coated particles was fixed at 6×10^6 in all DPPH assays. Samples were protected from light and kept on a rotating mixer for 20 min at 25 ℃. Then, 200 μL of the particle suspension was placed in a fresh tube and centrifuged (2000 *g*, 1 min). The supernatant (150 μL) was withdrawn and introduced into a 96-well plate and the absorbance at 515 nm was measured.

Table SI3.1. Summary of liquid chromatography−mass analyses of eucalyptus (Euc) extracts

Compound	R_t (min)[a]	[M-H]$^-$	Identification	Area (%)
Chlorogenic acid[b]	20	353.09	Ref. 5	10.3
	20.7	353.09		
Catechin[b,c]	21.2	289.07	Ref. 5	9.4
Apigenin-7-glucoside[b]	21.9	431.19	Ref. 6	2.35
Gallocatechin[b]	22.9	305.07	Ref. 6	54
Myricetrin[b,c]	24.9	463.09	Ref. 7	10.3
Quercetrin[b,c]	26.6	447.09	Ref. 7	4.76
Isorhamnetin 3-O-glucoside[b]	27.3	477.23	Ref. 8	8.9

[a]R_t, retention time.
[b]Identified by retention time and mass according to references.
[c]Identified by comparison to standard chemicals.

Table SI3.2. Myricetrin (Myr)-to-quercetrin (Quer) mass ratios in the metal–phenolic network films assembled on various substrates

Substrate	Myr-to-Quer ratio (mass)
~100 nm PMMA particles[a]	9.0
~800 nm mesoporous silica particles	5.4
~2.8 μm aminated silica particles	7.3
planar quartz	6.8

[a]PMMA, poly(methyl methacrylate).

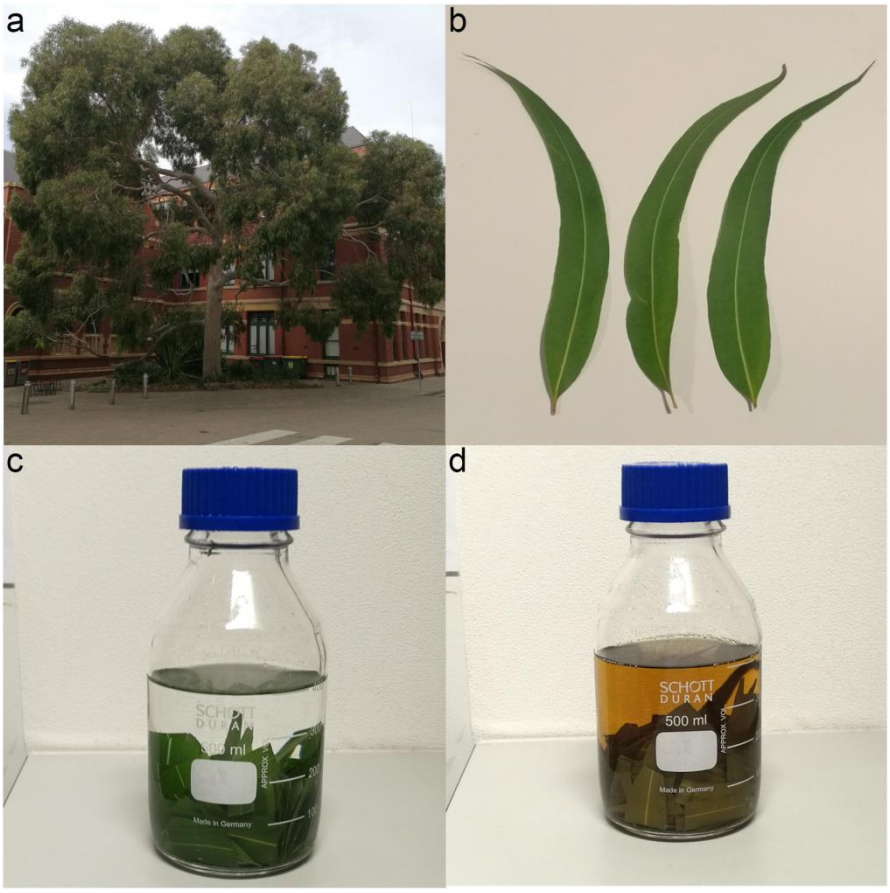

Figure SI3.1. Preparation of eucalyptus (Euc) extracts. Mature Euc leaves were collected from (a) a Euc tree. (b) The leaves were rinsed, cleaned, cut into smaller pieces and (c) placed in 400 mL Milli-Q water. After incubation of the leaves in an 85 ℃ oven for 12 h, (d) the Euc extracts were obtained.

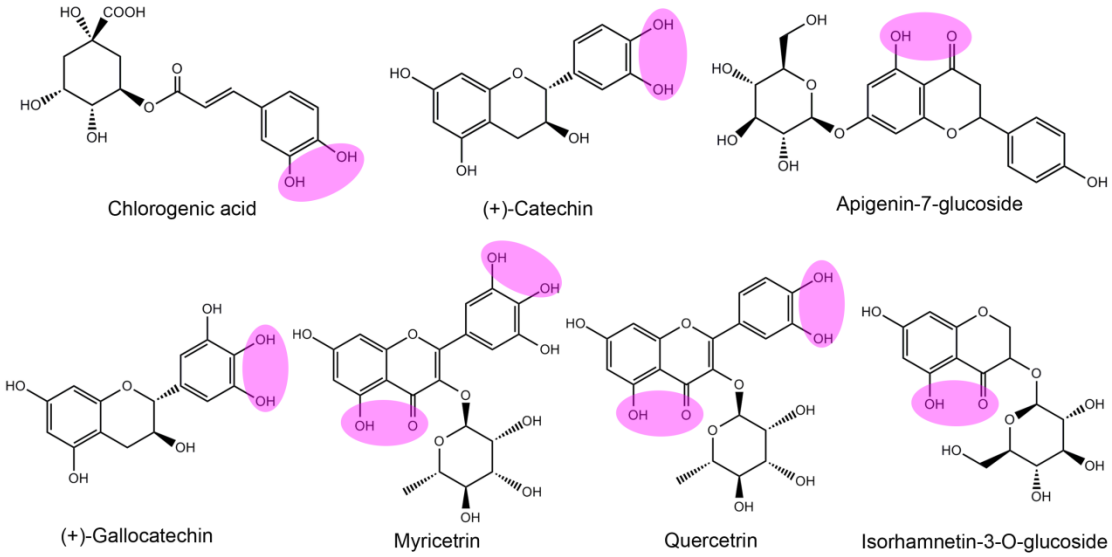

Figure SI3.2. Chemical structures of major phenolic compounds in Euc extract: chlorogenic acid (CA), (+)-catechin (Cat), apigenin-7-glucoside (AG), (+)-gallocatechin (Gal), myricetrin (Myr), quercetrin (Quer), and isorhamnetin-3-O-glucoside (Isg). Possible chelating sites for Fe^{III} are highlighted in pink.

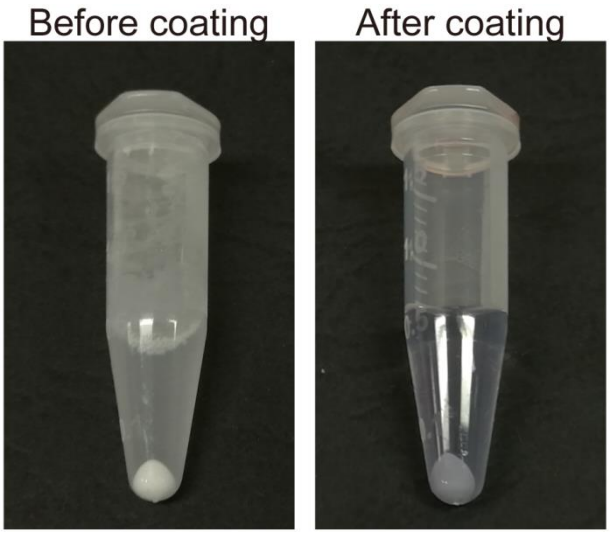

Figure SI3.3. Photographs of poly(methyl methacrylate) (PMMA) particles (~3.7 μm) before and after metal–phenolic network (MPN) coating by selective metal–phenolic assembly.

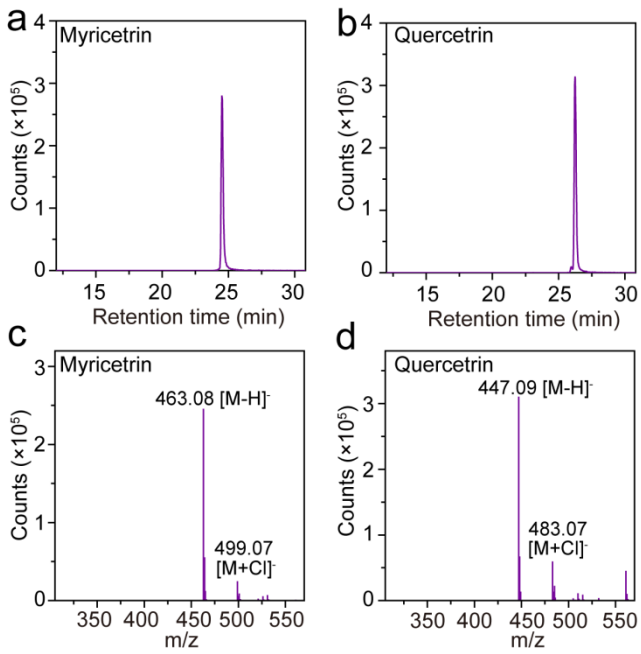

Figure SI3.4. Total ion chromatograms showing the retention times of (a) pure myricetrin (*m*/*z* 463.08) and (b) quercetrin (*m*/*z* 447.09). Mass spectra of (c) myricetrin and (d) quercetrin.

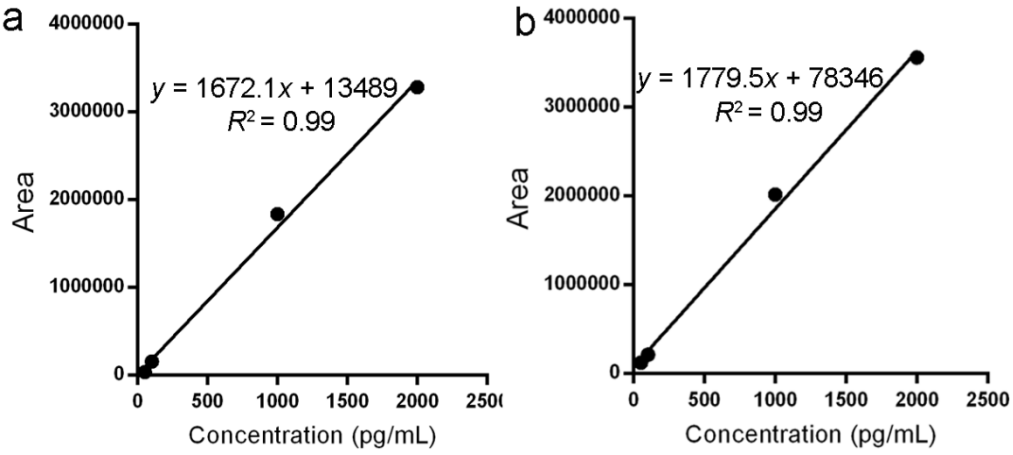

Figure SI3.5. Liquid chromatography−mass spectrometry standard curves of myricetrin and quercetrin in water.

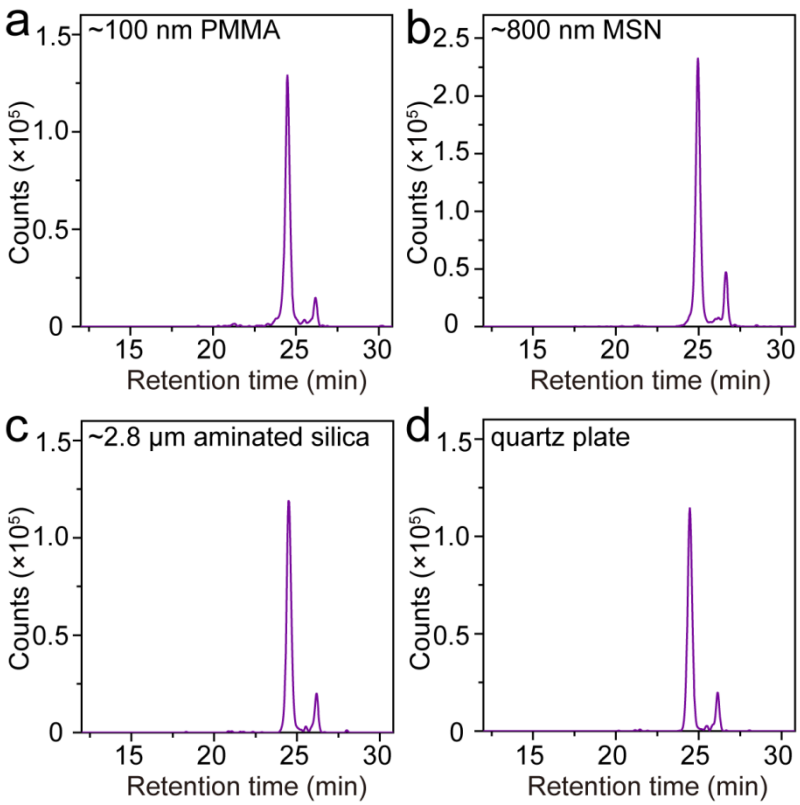

Figure SI3.6. Combined extracted ion chromatograms (EICs) of CA (*m*/*z* 353.09), Cat (*m*/*z* 289.07), AG (*m*/*z* 431.19), Gal (*m*/*z* 305.07), Myr (*m*/*z* 463.08), Quer (*m*/*z* 447.09), and Isg (*m*/*z* 477.23) in disassembled films formed by selective metal–phenolic assembly on various substrates: (a) ~100 nm PMMA particles, (b) ~800 nm mesoporous silica (MSN) particles, (c) ~2.8 μm aminated silica particles, and (d) 1 cm × 3 cm quartz plate.

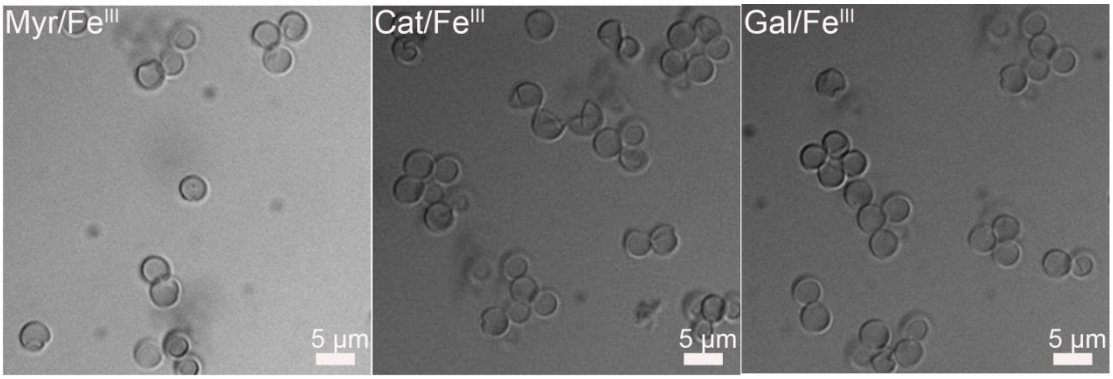

Figure SI3.7. Differential interference contrast microscopy images of Myr/Fe^{III}, Cat/Fe^{III}, and Gal/Fe^{III} capsules.

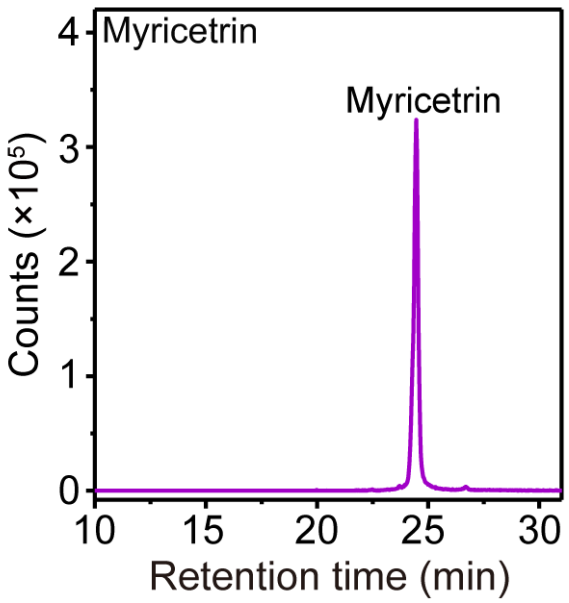

Figure SI3.8. Combined EICs of Myr (*m*/*z* 463.08), Cat (*m*/*z* 289.07), and Gal (*m*/*z* 305.07) in disassembled capsules prepared using a model phenolic mixture of Myr/Cat/Gal at a molar ratio of 1:25:25.

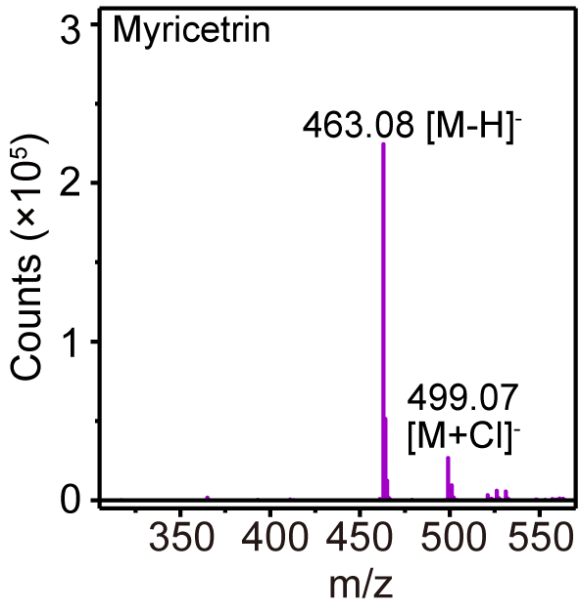

Figure SI3.9. Mass spectrometry pattern of myricetrin from disassembled capsules prepared from a model phenolic mixture of Myr/Cat/Gal at a molar ratio of 1:25:25.

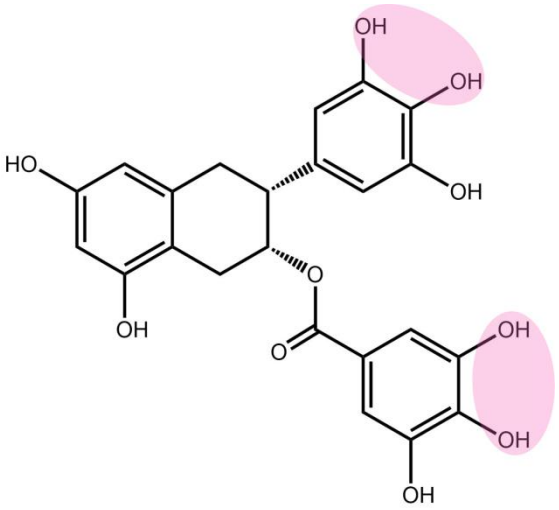

Figure SI3.10. Chemical structure of epigallocatechin gallate (EGCG). Possible chelating sites for Fe^{III} are highlighted in pink.

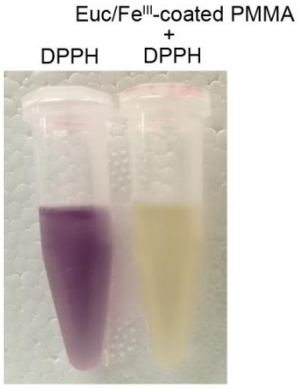

Figure SI3.11. Photograph of ethanolic 2,2′-diphenyl-picrylhydrazyl (DPPH) solution before and after exposure to Euc/Fe^{III}-coated PMMA particles.

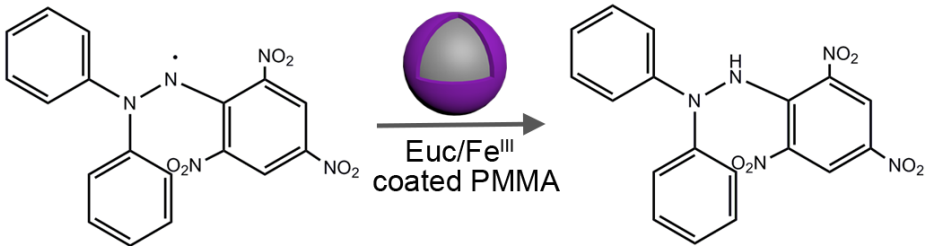

Figure SI3.12. Schematic of the reduction of DPPH radical to DPPHH by Euc/Fe^{III}-coated PMMA particles.

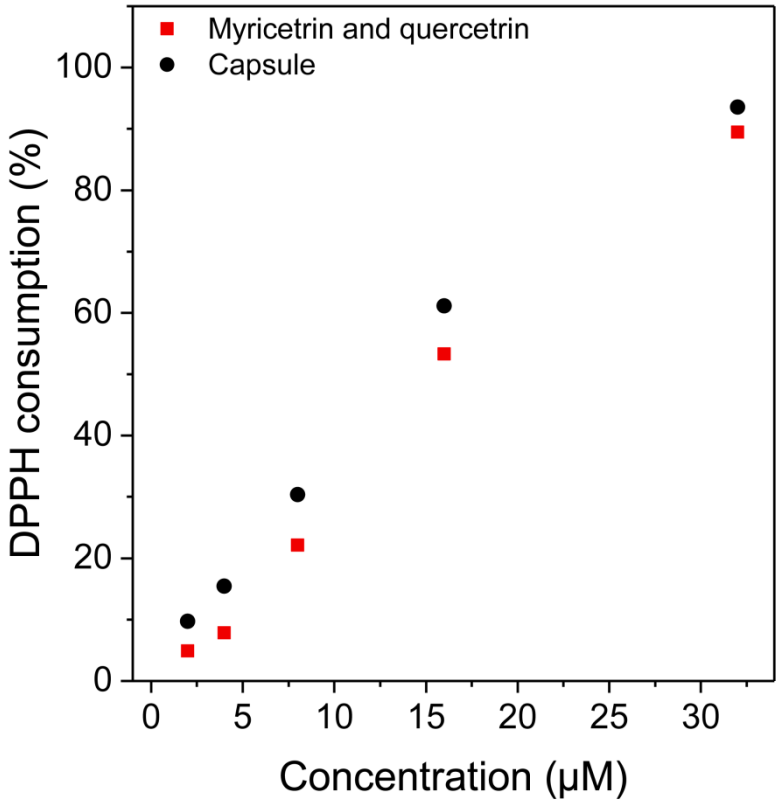

Figure SI3.13. DPPH scavenging activity of Euc/Fe^{III} capsules and equivalent mixture of myricetrin and quercetrin at different concentrations.

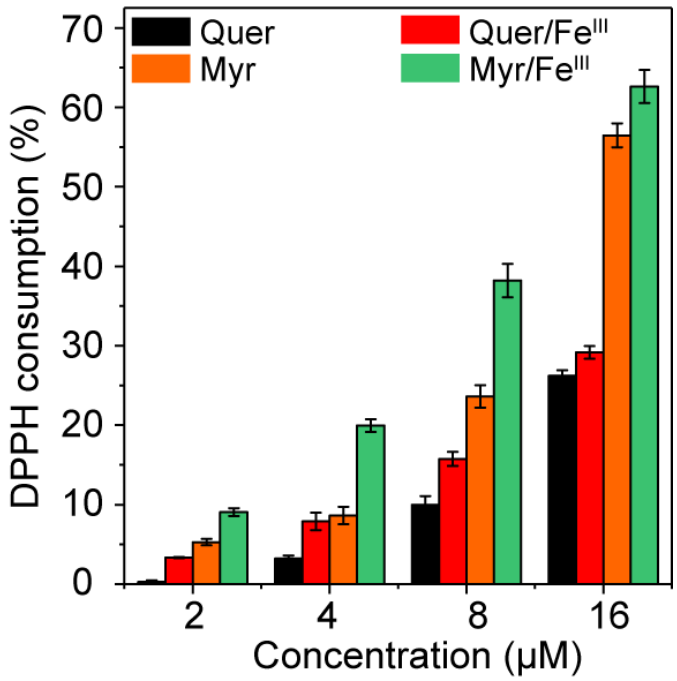

Figure SI3.14. DPPH consumption of Quer, Quer/Fe^{III} (molar ratio = 1:1), Myr and Myr/Fe^{III} (molar ratio = 1:1) at different concentrations.

References

1. Rahim, M. A.; Björnmalm, M.; Bertleff-Zieschang, N.; Ju, Y.; Mettu, S.; Leeming, M. G.; Caruso, F. Multiligand Metal–Phenolic Assembly from Green Tea Infusions. *ACS Appl. Mater. Interfaces* **2018**, *10*, 7632–7639.
2. Wang, J.-G.; Zhou, H.-J.; Sun, P.-C.; Ding, D.-T.; Chen, T.-H. Hollow Carved Single-Crystal Mesoporous Silica Templated by Mesomorphous Polyelectrolyte−Surfactant Complexes. *Chem. Mater.* **2010**, *22*, 3829–3831.
3. Rahim, M. A.; Kempe, K.; Müllner, M.; Ejima, H.; Ju, Y.; van Koeverden, M. P.; Suma, T.; Braunger, J. A.; Leeming, M. G.; Abrahams, B. F.; Caruso, F. Surface-Confined Amorphous Films from Metal-Coordinated Simple Phenolic Ligands. *Chem. Mater.* **2015**, *27*, 5825–5832.
4. Yun, G.; Besford, Q. A.; Johnston, S. T.; Richardson, J. J.; Pan, S.; Biviano, M.; Caruso, F. Self-Assembly of Nano- to Macroscopic Metal–Phenolic Materials. *Chem. Mater.* **2018**, *30*, 5750-5758.
5. Santos, S. A. O.; Freire, C. S. R.; Domingues, M. R. M.; Silvestre, A. J. D.; Neto, C. P. Characterization of phenolic components in polar extracts of *Eucalyptus globulus* labill. bark by high-performance liquid chromatography–mass spectrometry. *J. Agric. Food Chem.* **2011**, *59*, 9386–9393.
6. Hossain, M. B.; Rai, D. K.; Brunton, N. P.; Martin-Diana, A. B.; Barry-Ryan, C. Characterization of phenolic composition in lamiaceae spices by LC-ESI-MS/MS. *J. Agric. Food Chem.* **2010**, *58*, 10576–10581.

7. de Brito, E. S.; Pessanha de Araújo, M. C.; Lin, L.-Z.; Harnly, J. Determination of the flavonoid components of cashew apple (*Anacardium occidentale*) by LC-DAD-ESI/MS. *Food Chem.* **2007**, *105*, 1112–1118.
8. Chen, Y.; Yu, H.; Wu, H.; Pan, Y.; Wang, K.; Jin, Y.; Zhang, C. Characterization and quantification by LC-MS/MS of the chemical components of the heating products of the flavonoids extract in pollen typhae for transformation rule exploration. *Molecules* **2015**, *20*, 18352–18366.

Chapter 4

Poly(ethylene glycol) Nanoparticles with Tunable Sizes and Morphologies via Adjusting Metal-Phenolic Crosslinking in Microemulsions

4.1. Abstract

Poly(ethylene glycol) (PEG) nanoparticles are a powerful platform for overcoming biological barriers in drug delivery. However, it is challenging to make sub-100 nm nanoparticles composed primarily of PEG with varying size and morphology using current techniques. Herein, I developed a facile approach to engineer PEG particles with tunable size and morphology by controlling the metal-phenolic coordination of multi-arm PEG-gallol in microemulsions. The complexation between Mn^{II} and PEG-gallol in the microemulsions gave rise to a series of PEG nanoparticles, from 30 nm solid spherical nanoparticles to 50 nm solid and hollow nanoparticles, depending on the metal to PEG-gallol ratio. Ultraviolet–visible (UV-vis) absorbance spectroscopy and X-ray diffraction data indicated the PEG particle self-assembly process was driven by metal-phenolic coordination. The variations in size and morphology likely resulted from the variation in PEG-gallol/Mn^{II} complexes amphiphilicity under different Mn-to-gallol ratios, as evidenced by contact angle measurements. Small angle X-ray scattering (SAXS) was employed to monitor intermolecular interaction during the particles evolution, where fitting analysis showed that ionic charges were the dominant driving force in converting free PEG-gallol/Mn^{II} into the different PEG particles. Finally, I explored the potential of the PEG nanoparticle as delivery systems by a systemic investigation on their pH sensitivity, cytotoxicity, and low-fouling properties. Taken together, these results demonstrate a facile technique to construct different PEG particles with promise in nanomedicine.

4.2. Introduction

In recent years, a variety of nanocarriers with fascinating properties have been developed to encapsulate therapeutic and/or imaging agents and deliver them to targeted disease sites.[1-3] However, their success has been greatly limited by a series of biological barriers.[4] Among them, one major barrier is the clearance by the mononuclear phagocyte system (MPS), which greatly lowers their chance of reaching the intended destination.[5] Poly(ethylene glycol) (PEG) particles are one of the most promising options,[6-7] as they can avoid uptake by the MPS and achieve an enhanced circulation time, which finally results in an increased accumulation in the intended disease sites.[6, 8]

So far, several impressive methods have been developed to construct PEG particles.[9] For instance, the Doyle group reported a high-throughput method by combining photolithography and microfluidics to produce micrometer PEG particles with precise control over size, shape and aspect ratio.[10] Additionally, the DeSimone group developed a particle replication in nonwetting templates (PRINT) technique for preparing PEG hydrogel particles with controlled shape, size, and surface chemistry.[11] Moreover, our group recently developed a mesoporous silica (MS) templating method to engineer super-soft hydrogel PEG particles.[12-13] However, most of these techniques are limited to making larger sized particles, and it has proven to be difficult to prepare smaller nanoparticles below 100 nm, which is considered an ideal size for many intravenous drug delivery applications.[14] Besides, they generally need different templates or devices to achieve a size control on resultant particles. Thus, there is a need to develop a facile method to prepare sub-100 nm PEG particles with varying sizes.

Recently, our group reported several novel methods using soft templates, including emulsions and microemulsions for the preparation of PEG-based nanoparticles by metal-phenolic assembly.[15,16] However, even with these methods, the fabrication of sub-100 nm PEG-based particles remains challenging. Herein, I report an optimized approach to precisely control the size (20-60 nm) and morphology (hollow *vs* solid) of PEG nanoparticles by tuning the metal-phenolic coordination within an emulsion system. Two different metal ions (Fe^{III}, Mn^{II}) were used in this study to control the metal-phenolic coordination in this microemulsion system. As shown in Scheme 4.1, Mn^{II} can give rise to different PEG-gallol/Mn^{II} nanoparticles with different sizes and morphologies dependent on the Mn^{II}-gallol ratio. This likely resulted from the difference in amphiphilicity of the PEG-gallol/Mn^{II} complexes under different Mn-to-gallol ratios, as confirmed by contact angle measurements. In situ SAXS was employed to monitor the structural evolution of PEG-gallol/Mn^{II} nanoparticles in the microemulsions and demonstrated that small PEG-gallol/Mn^{II} complexes transition into PEG-gallol/Mn^{II} particles after the pH rises. Further fitting suggested that ionic screening was the major driving force for structural evolution, which matched the experimental data as determined by TEM. Finally, these PEG-gallol/Mn^{II} particles were low-fouling and showed good biocompatibility and pH-sensitive release properties, which make the PEG-gallol/Mn^{II} particles a promising potential delivery system to avoid recognition by the MPS followed by subsequent release of the loaded cargo in the specific disease site.

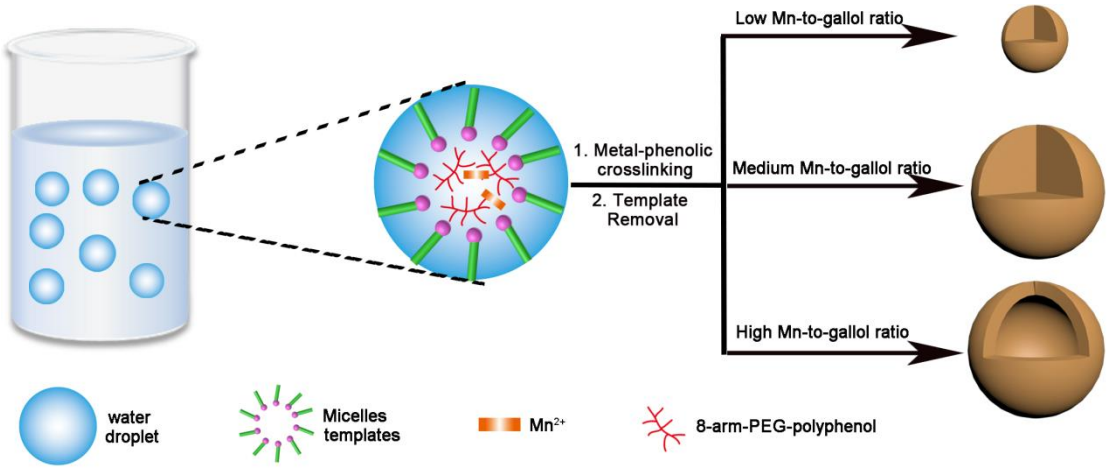

Scheme 4.1. Facile synthesis of poly(ethylene glycol) nanoparticles with tunable size and morphology by controlling metal-phenolic coordination.

4.3. Results and Discussion

The PEG-gallol was synthesized by conjugating gallol groups onto the terminus of 8-arm-PEG (10 kDa) according to the previously reported method with minor modification (Figure SI4.1).[17] Then, PEG-gallol was mixed with $FeCl_3$ or $MnCl_2$ solution, and then added into an oil phase containing cyclohexane, hexanol, and Triton X-100 to prepare one microemulsion containing PEG-gallol/Fe^{III} or PEG-gallol/Mn^{II} complexes. Subsequently, another microemulsion containing Tris buffer (pH 8.0) was added to raise the pH and initiate metal-phenolic coordination for PEG polymerization inside the microemulsions. After 1 h of stirring, PEG-gallol/Fe^{III} or PEG-gallol/Mn^{II} nanoparticles were obtained after 3 washing steps with ethanol and water. The resultant PEG nanoparticles were characterized by dynamic light scattering (DLS) and transmission electron microscopy (TEM), where it was found that Fe^{III} only gave rise to small (30 nm) solid PEG-gallol/Fe^{III} nanoparticles regardless of the feed ratios (Figure SI4.2). This is likely due to the stronger gallol/Fe^{III} affinity that resulted in instantaneous crosslinking of the PEG-gallol/Fe^{III} complexes inside the droplet. Interestingly, Mn^{II} gave rise to different

PEG-gallol/Mn^{II} nanoparticles with varying sizes and morphologies, under different feed ratios of Mn^{II}-to-gallol. Figure 4.1a shows TEM images of the resultant PEG-gallol/Mn^{II} nanoparticles from different Mn^{II}-to-gallol ratios (0.25:1, 1:1, 4: 1). It was found that when the amount of PEG-gallol greatly exceed the amount of Mn^{II} (Mn^{II}: gallol= 0.25: 1), small sized solid PEG-gallol/Mn^{II} nanoparticles (30 nm) were obtained. Increasing the feed ratio to 1:1 gave rise to larger sized solid PEG nanoparticles (50 nm); further increasing the feed ratio to 1:4 resulted in larger hollow nanoparticles (50 nm).

UV-vis absorbance spectroscopy was employed to investigate the interaction between the metal and PEG ligands in the PEG nanoparticles. A new broad absorption emerged from 350 to 600 nm, compared with the free PEG-gallol (Figure 4.1b), corresponding to the ligand-to-metal charge-transfer (LMCT) band of gallol/Mn^{II}. This indicated the presence of gallol/Mn^{II} coordination in the resultant PEG nanoparticles. As PEG polymerization was initiated by metal-phenolic coordination under alkaline condition, X-ray diffraction studies were performed to detect whether there was any hydroxide materials in the resultant PEG-gallol/Mn^{II} nanoparticles. Figure 4.1c shows that the PEG nanoparticles had a X-ray diffraction pattern similar to that of pure water and no crystalline peaks associated with manganese hydroxide were observed. These data indicated the PEG nanoparticles were composed of amorphous metal-phenolic driven PEG crosslinking without manganese hydroxide.

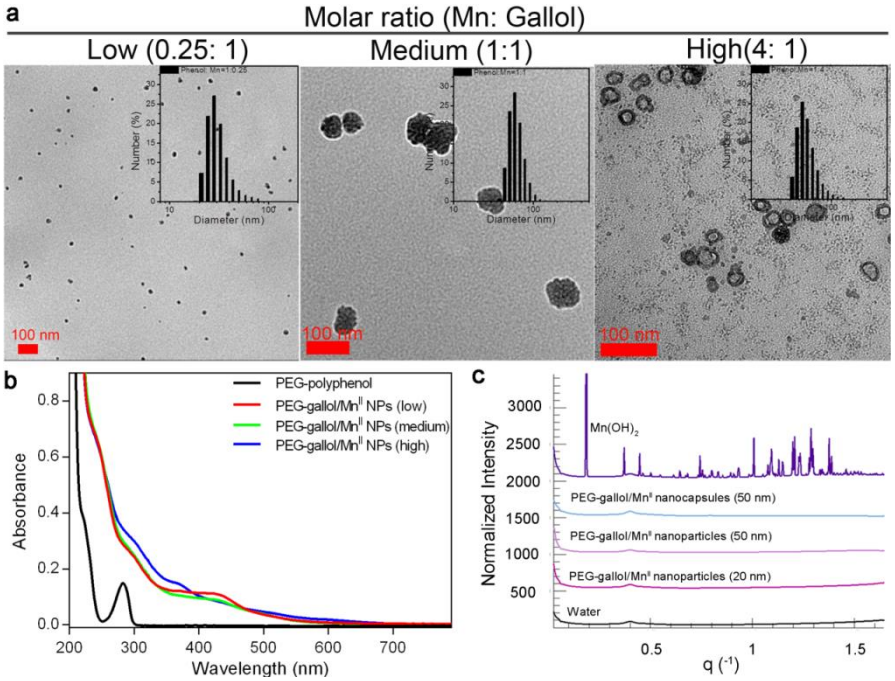

Figure 4.1. Characterization of different PEG-gallol/Mn^{II} nanoparticles under different Mn-to-gallol ratios (0.25: 1, 1:1, 4:1); (a) TEM images of different PEG-gallol/Mn^{II} nanoparticles (inset: DLS data of PEG-MPN-Mn NPs); (b) UV-vis spectrum of different PEG-gallol/Mn^{II} nanoparticles; (c) X-ray diffraction of water, different PEG-gallol/Mn^{II} nanoparticles from different Mn-to-gallol ratios and manganese hydroxide.

Recent literature reported that the amphiphilicity of the precursor greatly affects the location of the monomer during the microemulsion reactions, which further influences the final particles morphology.[18] To determine the amphiphilicity of the PEG-gallol/Mn^{II} complexes under different ratios, contact angle measurements were performed. As indicated in Figure 4.2a, the contact angles increased when the molar ratio increased; the contact angle was only 12 ° at low Mn^{II}-to-gallol (1:0.25), but increased to 18.9 ° and 43.6 ° at 1:1 and 4:1, respectively (Figure SI4.3). This indicated an increase in amphiphilicity of PEG-gallol/Mn^{II} complexes with the increasd Mn^{II} concentration, which suggests that different feed ratios resulted in varying crosslinking degrees in the PEG-gallol/Mn^{II} complexes as shown in Figure 4.2b. Under low Mn concentrations, gallol-to-Mn (1:0.25), the metal-phenolic crosslinking was low so the PEG-gallol/Mn^{II} complexes remained hydrophilic and the major

complexes remained inside the water droplet. However, with increased Mn^{II} concentration (gallo-to-Mn=1:1, 1:4), metal-phenolic crosslinking increased, resulting in an increase in PEG crosslinking, which further brought an increase in the amphiphilicity of PEG-gallol/Mn^{II}. This allowed PEG-gallol/Mn^{II} to diffuse to the interface between the water and oil phases, leading to larger particles. A further increase in Mn^{II} brought another increase in amphiphilicity to the PEG-gallol/Mn^{II}, confining those complexes within the interface and thereby leading to capsules.

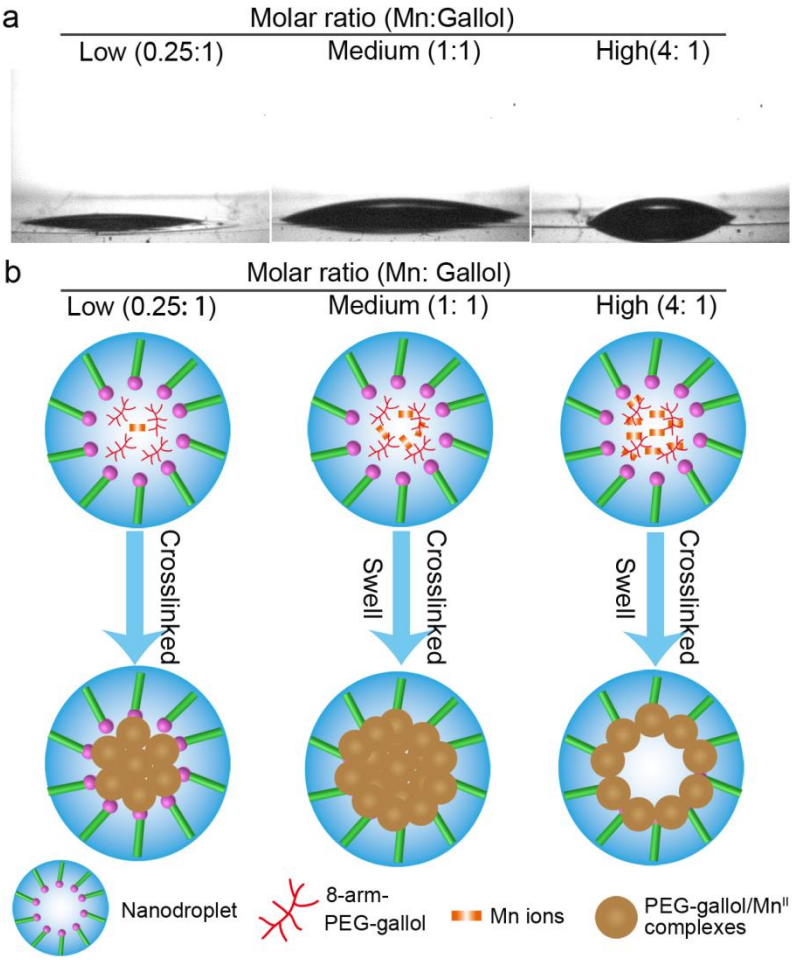

Figure 4.2. Contact angles of PEG-gallol/Mn^{II} complexes and suggested mechanism of PEG-gallol/Mn^{II} formulation. (a) Contact angles of MPN complexes increase with the increase in concentration of Mn^{II}. (b) Scheme illustrating the mechanism of different PEG-gallol/Mn^{II} nanoparticles: with the increase in Mn^{II} concentration, the

degree of crosslinking increases, which make MPN complex become amphiphilic. This allows the complexes to diffuse to the interface between the water and oil phases.

Subsequently, in situ SAXS analysis was employed to monitor the structural evolution of the PEG nanoparticles in the microemulsions during the reaction. It was observed that the intensities at high q values (0.8-0.9), corresponding to small PEG-gallol or PEG-gallol/Mn^{II} species, decreased during the reaction suggesting the consumption of free small PEG-gallol/Mn^{II} complexes (Figure 4.3a). Meanwhile, at low q values (0.001), which was assigned to large PEG-gallol/Mn^{II} particles (50-100 nm), the signal increased with time, indicating an increase in large particle formation as the reaction progressed. These SAXS results suggested that the small free PEG-gallol/Mn^{II} complexes convert into PEG-gallol/Mn^{II} particles during the reaction. The SAXS data at the end-points (60 minutes) was fitted with Igor 6 analysis software. It was observed that an ionic screening model gave the best fitting, suggesting that ionic charge on the particles forces them to self-arrange in solution. As summarized in Table SI4.1, there was a significant increase in ion concentration from low to high Mn-gallol ratios, which matched the experiment data. The size of the small species in the three batches (low, medium, large) were around 5 nm (Figure 4.3b, c), which can be assigned to free PEG-gallol or PEG-gallol/Mn^{II} complexes. Meanwhile, the size of the large species was around 50-60 nm in the medium and high ratio batches (Figure 4.3b, d). This was in strong agreement with the TEM and DLS (Figure 4.2a), indicating some small PEG-gallol/Mn complex polymerized into large PEG-gallol/Mn^{II} nanoparticles over time. The large species in the low ratio batch were found to be 100 nm, which was significantly larger than the actual size of the resultant nanoparticles, possibly due to some undesirable aggregates during the reaction.

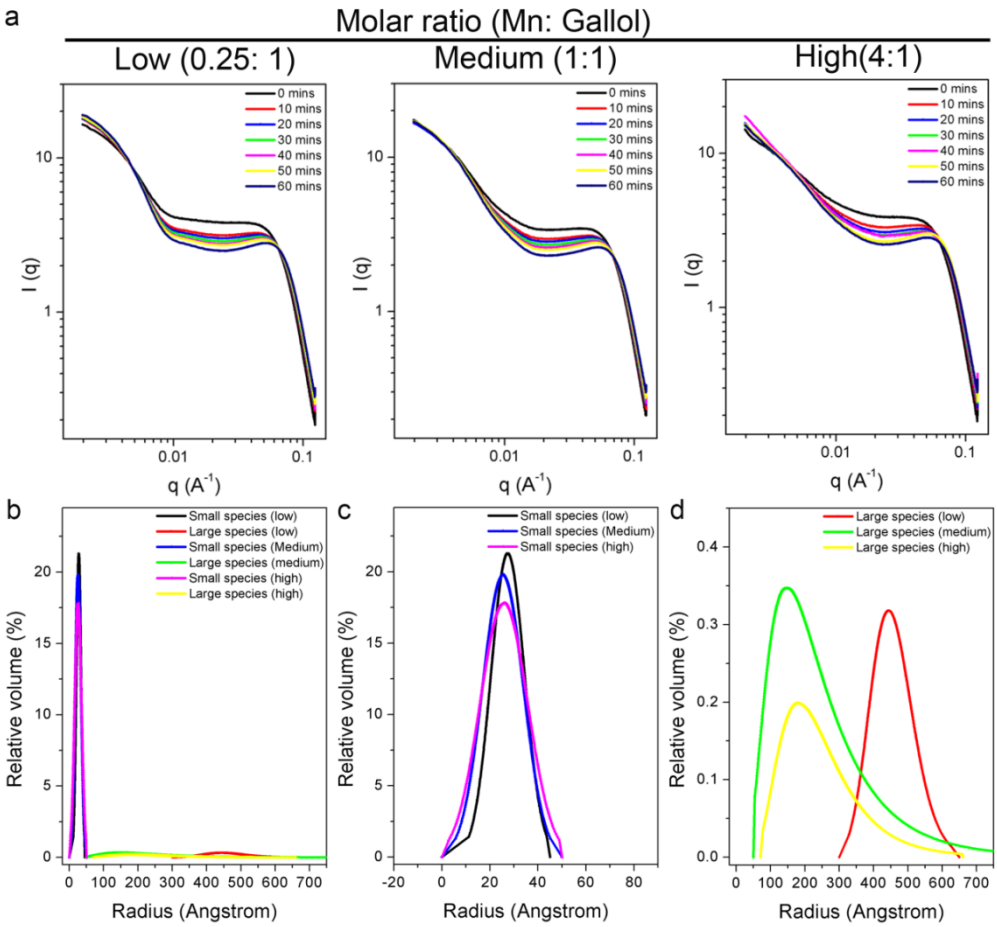

Figure 4.3. In situ small angle X-ray scattering (SAXS) studies for monitoring different PEG-gallol/Mn^{II} evolution under different Mn-to-gallol ratios, 0.25:1, 1:1, 1:4. (b) Igor6 fitting results showing the relative volume of small and large species in emulsion; (c) Relative volume of small species (PEG-gallol/Mn^{II} complexes) in the emulsion; (d) Relative volume of large species (PEG-gallol/Mn^{II} nanoparticles) in the emulsion.

Quality nanocarriers generally should possess great biocompatibility to prevent side effects to healthy organs, and should also guarantee a specific release of cargo at its target sites. Therefore, the PEG nanocapsules (50 nm) were selected to test the cytotoxicity and pH-sensitive properties of the materials, as particles in this size range have been reported to possess greater circulation as well as good uptake.[14, 19] Firstly, the stability of the PEG nanocapsules were investigated in different pH (7.4 and 5.5) PBS media. The release profile of the Mn^{II} ions were determined by ICP according to established standard curves (Figure SI4.4). Figure 4.4a shows that only 3% of the

Mn^{II} was released from the PEG capsule when incubated in neutral PBS (7.4) for 8 h, demonstrating a good stability of the PEG capsules. However, the capsule quickly decomposed under acid pH condition (Figure SI4.5), exhibiting significantly faster release properties. 38.6% of the Mn^{II} was released at 8 h, and a sustained release was subsequently achieved with a final release of 50 % Mn^{II} at 24 h. Such pH-sensitive properties render the PEG capsules a potentially promising drug delivery system that can prevent premature release during blood circulation, but release the loaded cargo upon exposure to acidic disease sites, such as cancer, inflammation, or after internalization into the endosome. Moreover, MTT assays demonstrated the cell viability of RAW 264.7 cells after 24 h incubation. As shown in Figure 4.4b, the PEG nanocapsules exhibited a great biocompatibility, which was in agreement with the previous report.[15] It was also noticed that they showed a slight cytoxicity, which may result from the release of Mn^{2+} when the PEG nanocapsules capsule internalized and degraded and released Mn^{II} ions in the acidic lysosome compartment, which could further induce an increased ROS.

So far, PEG based nanocarriers have been reported to be low fouling and avoid nonspecific interactions towards cells. To assess the low-fouling properties of the PEG nanoparticles, three different cell lines were treated with the three different PEG particles (Mn: 5 μM). After 24 h incubation, the cells were washed and harvested for ICP to calculate the cellular Mn^{II} concentration to determine the association of the three different nanoparticles. As indicated in Figure 4.4c, all three nanoparticles exhibited low fouling properties towards the three different cell lines. It was also noticed that the 50 nm nanoparticles and capsules presented slightly higher association than the 30 nm nanoparticles. This may be due to the ability of the larger nanoparticles to better occupy multiple receptor binding sites than smaller ones.[19]

Taken together, these results indicated the PEG nanoparticles are low-fouling, which can reduce nonspecific adsorption and thus could exhibit extended circulation in the blood stream.

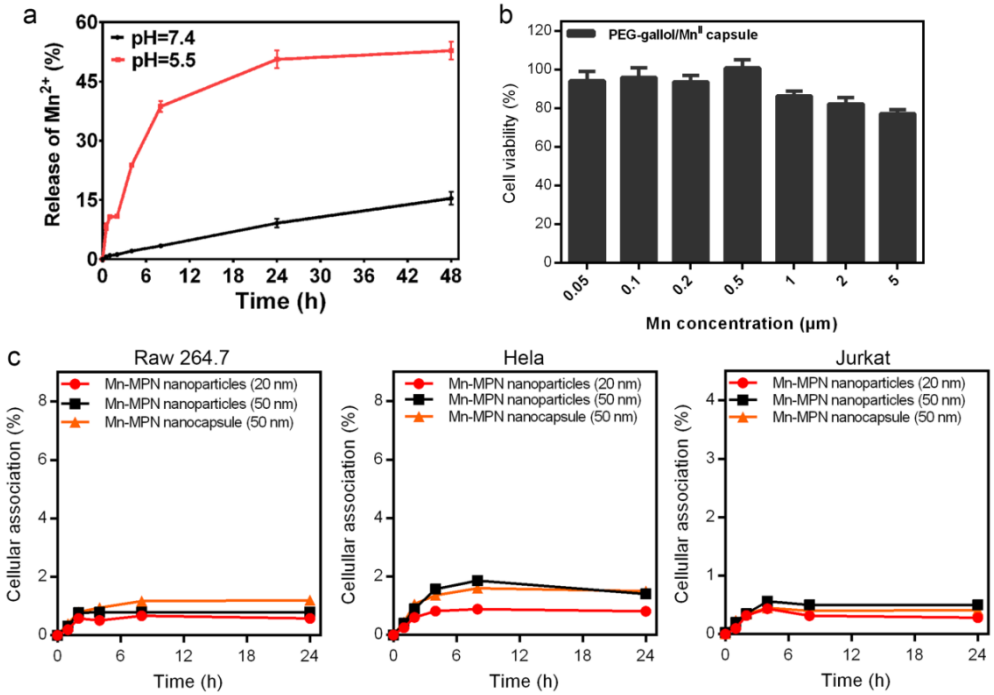

Figure 4.4. pH sensitivity, cytotoxicity, and low-fouling properties of PEG-gallol/Mn^{II} nanoparticles; (A) pH sensitive property of the PEG-gallol/Mn^{II} nanocapsules (50 nm): release profile of Mn^{II} from PEG-gallol/Mn^{II} nanocapsule; (b) Cell viabilities of RAW264.7 cells treated with different concentration of PEG-gallol/Mn^{II} nanocapsules. (c) Cellular association of different PEG-gallol/Mn^{II} nanoparticles after 24 h incubation in different cell lines, including RAW264.7, Hela and Jurkat cells.

4.4. Conclusion

I developed a facile method to tune the size and morphology of PEG particles by controlling the ratio of the metal to ligand in metal-phenolic interaction in microemulsions. The complexation of Mn^{II} and PEG-gallol within the microemulsions gave arise to a series of PEG nanoparticles with varying size and structure. UV-vis absorbance and XRD data indicated these different PEG particles were driven from metal-phenolic coordination. The difference in size and morphologies possibly arose

from the variation in PEG-gallol/Mn^{II} complex amphiphilicity under different ratios, evidenced by contact angle measurements. In situ SAXS was also performed to monitor intermolecular interaction during the particles evolution, showing the ionic charges was the dominant driving force to convert free PEG-gallol/Mn^{II} into different PEG particles. Finally, the potential of the PEG nanoparticles as delivery systems was confirmed by investigating their pH responsiveness, cytotoxicity, and low-fouling properties.

4.5. References

1. Cui, J.; Richardson, J. J.; Björnmalm, M.; Faria, M.; Caruso, F., Nanoengineered templated polymer particles: Navigating the biological realm. *Accounts of Chemical Research* **2016,** *49* (6), 1139-1148.

2. Torchilin, V. P., Multifunctional, stimuli-sensitive nanoparticulate systems for drug delivery. *Nature Reviews Drug Discovery* **2014,** *13*, 813.

3. Lin, G.; Mi, P.; Chu, C.; Zhang, J.; Liu, G., Inorganic nanocarriers overcoming multidrug resistance for cancer theranostics. *Advanced Science* **2016,** *3* (11), 1600134.

4. Blanco, E.; Shen, H.; Ferrari, M., Principles of nanoparticle design for overcoming biological barriers to drug delivery. *Nature Biotechnology* **2015,** *33*, 941.

5. Tsoi, K. M.; MacParland, S. A.; Ma, X.-Z.; Spetzler, V. N.; Echeverri, J.; Ouyang, B.; Fadel, S. M.; Sykes, E. A.; Goldaracena, N.; Kaths, J. M.; Conneely, J. B.; Alman, B. A.; Selzner, M.; Ostrowski, M. A.; Adeyi, O. A.; Zilman, A.; McGilvray, I. D.; Chan, W. C. W., Mechanism of hard-nanomaterial clearance by the liver. *Nature Materials* **2016,** *15*, 1212.

6. Suk, J. S.; Xu, Q.; Kim, N.; Hanes, J.; Ensign, L. M., PEGylation as a strategy for improving nanoparticle-based drug and gene delivery. *Advanced Drug Delivery Reviews* **2016,** *99*, 28-51.

7. Jokerst, J. V.; Lobovkina, T.; Zare, R. N.; Gambhir, S. S., Nanoparticle PEGylation for imaging and therapy. *Nanomedicine* **2011,** *6* (4), 715-728.

8. Bazile, D.; Prud'homme, C.; Bassoullet, M. T.; Marlard, M.; Spenlehauer, G.; Veillard, M., Stealth Me. PEG-PLA nanoparticles avoid uptake by the mononuclear phagocytes system. *Journal of Pharmaceutical Sciences* **1995,** *84* (4), 493-498.

9. Richardson, J. J.; Cui, J.; Björnmalm, M.; Braunger, J. A.; Ejima, H.; Caruso, F., Innovation in layer-by-layer assembly. *Chemical Reviews* **2016,** *116* (23),

14828-14867.

10. Dendukuri, D.; Pregibon, D. C.; Collins, J.; Hatton, T. A.; Doyle, P. S., Continuous-flow lithography for high-throughput microparticle synthesis. *Nature Materials* **2006,** *5*, 365.

11. Xu, J.; Wong, D. H. C.; Byrne, J. D.; Chen, K.; Bowerman, C.; DeSimone, J. M., Future of the particle replication in nonwetting templates (PRINT) technology. *Angewandte Chemie International Edition* **2013,** *52* (26), 6580-6589.

12. Cui, J.; Björnmalm, M.; Liang, K.; Xu, C.; Best, J. P.; Zhang, X.; Caruso, F., Super-soft hydrogel particles with tunable elasticity in a microfluidic blood capillary model. *Advanced Materials* **2014,** *26* (43), 7295-7299.

13. Cui, J.; De Rose, R.; Alt, K.; Alcantara, S.; Paterson, B. M.; Liang, K.; Hu, M.; Richardson, J. J.; Yan, Y.; Jeffery, C. M.; Price, R. I.; Peter, K.; Hagemeyer, C. E.; Donnelly, P. S.; Kent, S. J.; Caruso, F., Engineering poly(ethylene glycol) particles for improved biodistribution. *ACS Nano* **2015,** *9* (2), 1571-1580.

14. Pelaz, B.; Alexiou, C.; Alvarez-Puebla, R. A.; Alves, F.; Andrews, A. M.; Ashraf, S.; Balogh, L. P.; Ballerini, L.; Bestetti, A.; Brendel, C.; Bosi, S.; Carril, M.; Chan, W. C. W.; Chen, C.; Chen, X.; Chen, X.; Cheng, Z.; Cui, D.; Du, J.; Dullin, C.; Escudero, A.; Feliu, N.; Gao, M.; George, M.; Gogotsi, Y.; Grünweller, A.; Gu, Z.; Halas, N. J.; Hampp, N.; Hartmann, R. K.; Hersam, M. C.; Hunziker, P.; Jian, J.; Jiang, X.; Jungebluth, P.; Kadhiresan, P.; Kataoka, K.; Khademhosseini, A.; Kopeček, J.; Kotov, N. A.; Krug, H. F.; Lee, D. S.; Lehr, C.-M.; Leong, K. W.; Liang, X.-J.; Ling Lim, M.; Liz-Marzán, L. M.; Ma, X.; Macchiarini, P.; Meng, H.; Möhwald, H.; Mulvaney, P.; Nel, A. E.; Nie, S.; Nordlander, P.; Okano, T.; Oliveira, J.; Park, T. H.; Penner, R. M.; Prato, M.; Puntes, V.; Rotello, V. M.; Samarakoon, A.; Schaak, R. E.; Shen, Y.; Sjöqvist, S.; Skirtach, A. G.; Soliman, M. G.; Stevens, M. M.; Sung, H.-W.; Tang, B.

Z.; Tietze, R.; Udugama, B. N.; VanEpps, J. S.; Weil, T.; Weiss, P. S.; Willner, I.; Wu, Y.; Yang, L.; Yue, Z.; Zhang, Q.; Zhang, Q.; Zhang, X.-E.; Zhao, Y.; Zhou, X.; Parak, W. J., Diverse applications of nanomedicine. *ACS Nano* **2017,** *11* (3), 2313-2381.

15. Dai, Y.; Guo, J.; Wang, T.-Y.; Ju, Y.; Mitchell, A. J.; Bonnard, T.; Cui, J.; Richardson, J. J.; Hagemeyer, C. E.; Alt, K.; Caruso, F., Self-assembled nanoparticles from phenolic derivatives for cancer therapy. *Advanced Healthcare Materials* **2017,** *6* (16), 1700467.

16. Besford, Q. A.; Ju, Y.; Wang, T.-Y.; Yun, G.; Cherepanov, P.; Hagemeyer, C. E.; Cavalieri, F.; Caruso, F., Self-assembled metal–phenolic networks on emulsions as low-fouling and pH-responsive particles. *Small* **2018,** *14* (39), 1802342.

17. Ju, Y.; Cui, J.; Müllner, M.; Suma, T.; Hu, M.; Caruso, F., Engineering low-fouling and pH-degradable capsules through the assembly of metal-phenolic networks. *Biomacromolecules* **2015,** *16* (3), 807-814.

18. Wei, B.; Wang, S.; Song, H.; Liu, H.; Li, J.; Liu, N., A review of recent progress in preparation of hollow polymer microspheres. *Petroleum Science* **2009,** *6* (3), 306-312.

19. Behzadi, S.; Serpooshan, V.; Tao, W.; Hamaly, M. A.; Alkawareek, M. Y.; Dreaden, E. C.; Brown, D.; Alkilany, A. M.; Farokhzad, O. C.; Mahmoudi, M., Cellular uptake of nanoparticles: journey inside the cell. *Chemical Society Reviews* **2017,** *46* (14), 4218-4244.

4.6. Supporting Information

Materials

Manganese(II) chloride tetrahydrate ($MnCl_2 \cdot 4H_2O$), tris-(hydroxymethyl)aminomethane (TRIS), thiazolyl blue tetrazolium bromide (MTT), cyclohexane, Triton X-100, 1-hexanol were purchased from Sigma-Aldrich and used as received without further purification. 8-Arm-poly(ethylene glycol) succinimidyl succinate (Mw 10 kDa) was obtained from JenKem Technology (USA). Multiply elements ICP standard solution and nitric acid (ultrapure) were obtained from Meack KGaA (Germany). Dulbecco's Modified Eagle Medium (DMEM), Roswell Park Memorial Institute medium (RPMI), fetal bovine serum (FBS), Dulbecco's phosphate-buffered saline (DPBS) were provided by Life Technologies.

Synthesis of PEG-gallol/Fe^{III} and PEG-gallol/Mn^{II} nanoparticles by microemulsion

PEG-polyphenol was synthesized by Dr. Yi Ju according to our previous method.[1] Then, the MPN NPs was prepared by reverse microemulsions using a reported protocol with minor modification. Briefly, a 5 mL mixture of 0.3 M Triton X-100/1-hexanol in cyclohexane containing 200 μL of an aqueous phase of $FeCl_3 \cdot 6H_2O$ (or $MnCl_2 \cdot 4H_2O$) and PEG-gallol mixture was stirred vigorously at 25 ℃. Then, 5 mL microemulsion phase (Cyclohexane containing 0.3 M Triton X-100 and 1.5 M 1-hexanol) containing 100 μL TRIS buffer (pH 8.0) was added into to rise pH for crosslinking. After half an hour, PEG-gallol/Mn^{II} nanoparticles was obtained by adding into 10 mL ethanol and then washed ethanol and ethanol/cyclohexane (v/v=1:1), finally dispersed in Millipore water.

Characterization of PEG-gallol/Mn^{II} nanoparticles

The hydrodynamic diameter of the particles was measured using a Zetasizer Nano ZS instrument (Malvern Instruments, Malvern, UK). The transmission electron microscopy (TEM) images, element mapping and EDX of PEG-gallol/Mn^{II} nanoparticles were performed on FEI Tecnai F20 TEM instrument operating at an acceleration voltage of 200 kV. The Ultraviolet–visible spectroscopy (UV/Vis) was conducted on Cary 4000 UV/Vis Spectrophotometer (Agilent Technologies, USA). The PEG-gallol/Mn^{II} nanoparticles was decomposed in 1 M HCl solutions, and then the metal concentration was determined by ICP.

Contact angle measurements

The contact angle measurements were out on a on a Data Physics OCA 20 tensiometer. Briefly, 5 μL of water droplet containing PEG-gallol/Mn^{II} complexes (PEG-gallol: 1 mg/mL) with varying gallol-to-Mn ratios were pipetted onto a bare glass and allowed to air dry. Water was placed onto the PEG-gallol/Mn^{II} complexes coated glass and the contact angle of water was measured.

In situ small angle X-ray scattering (SAXS)

In situ SAXS experiments were performed to monitor metal-phenolic coordination driven PEG polymerization evolution at the Australian Synchrotron (SAXS beamline). The experiment was performed in a pulsed pumping mode to increase the statistics over a large volume of solution. Upon mixing two microemulsion solutions, a monomodal distribution of particles was formed within 180 s. After that, further evolution of the particle size distribution was detected every 10 minutes.

Release profiles of PEG-gallol/Mn^{II} Nanocapsules

The release study was carried out according to our previously established protocol.[2] Briefly, PEG-gallol/Mn^{II} nanocapsules (100 μL containing 26.4 μg Mn^{II}) were dialyzed against 10 mL phosphate buffer (10 mM, pH 5.5 or 7.4) using a dialysis

membrane (cutoff molecular weight: 3.5 kD). At pre-determined time points, a certain amount (5 mL) of solution outside the dialysis membrane was taken out. A equal amount (5 mL) of fresh buffer was added into to kept the total volume constant. The concentration of Mn^{2+} was determined using ICP.

Cell viability Assays

RAW264.7 cells were seeded on a 96-well plate (Corning, USA) with a cell density of 5000 cells/well in 100 μL media. After 12 h, PEG-gallol/Mn^{II} nanocapsules were added at varying concentrations. After 24 h of incubation, cell viability was evaluated by commercial MTT assay.

Cell association by ICP

Raw 264.7, Hela and Jurkat cells were seeded into 6-well plates (cell density: 5 × 10^5 cells/well), and incubated overnight at 37 ℃ with 5% CO2. A certain amount of PEG-gallol/Mn^{II} nanocapsules (Mn: 5 μM) were added and incubated for pre-determined time (1, 2, 4, 8, and 24 h). After removing cell culture medium, Raw 264.7, Hela and Jurkat cells were washed with PBS thrice and then collected by cell scraper, followed by centrifugation at 1000 g for 5 min. Cells were lysed in lysis buffer and then subjected to ICP measurement for metal concentration determination.

Table SI4.1. Structure factors in different microemulsion system under different Mn-to-gallol ratios at 60 minutes

	Low	Medium	High
Distance (Angstrom)	37.85	37.7	37.9
Volume fraction	0.122	0.1229	0.133
Ion concentration (M)	0.27	0.482	2.08

Table SI4.2. Large species proportion in microemulsion under different Mn-to-gallow ratios at 60 minutes

	Fraction of large species
Low	0.000000265
Medium	0.00000492
High	0.0000264

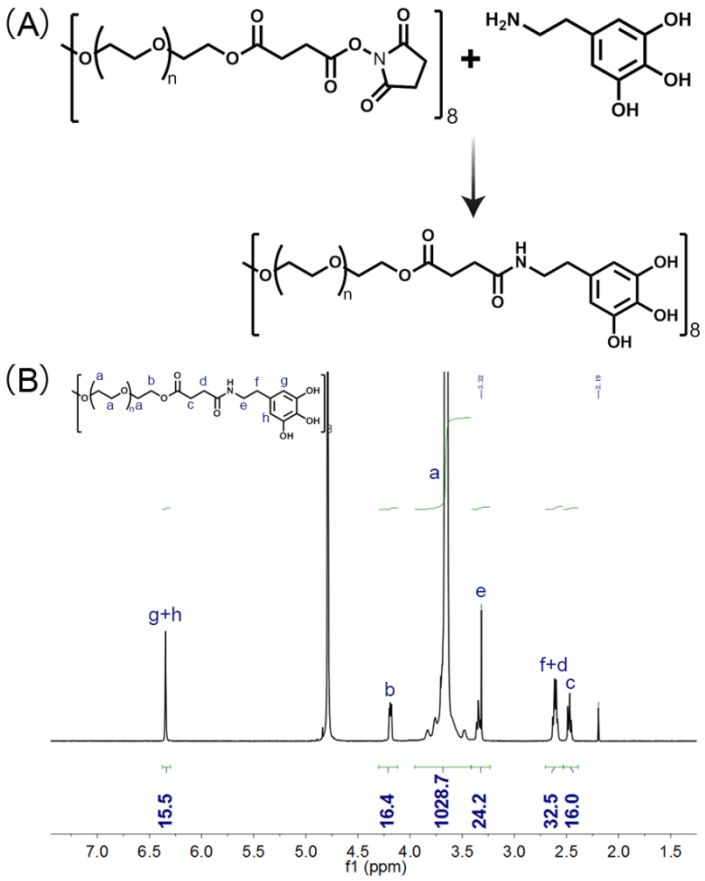

Figure SI4.1. (A) Scheme illustrating the synthesis of PEG-gallol; (B)^{1}H-NMR spectrum of PEG-gallol in D_2O.

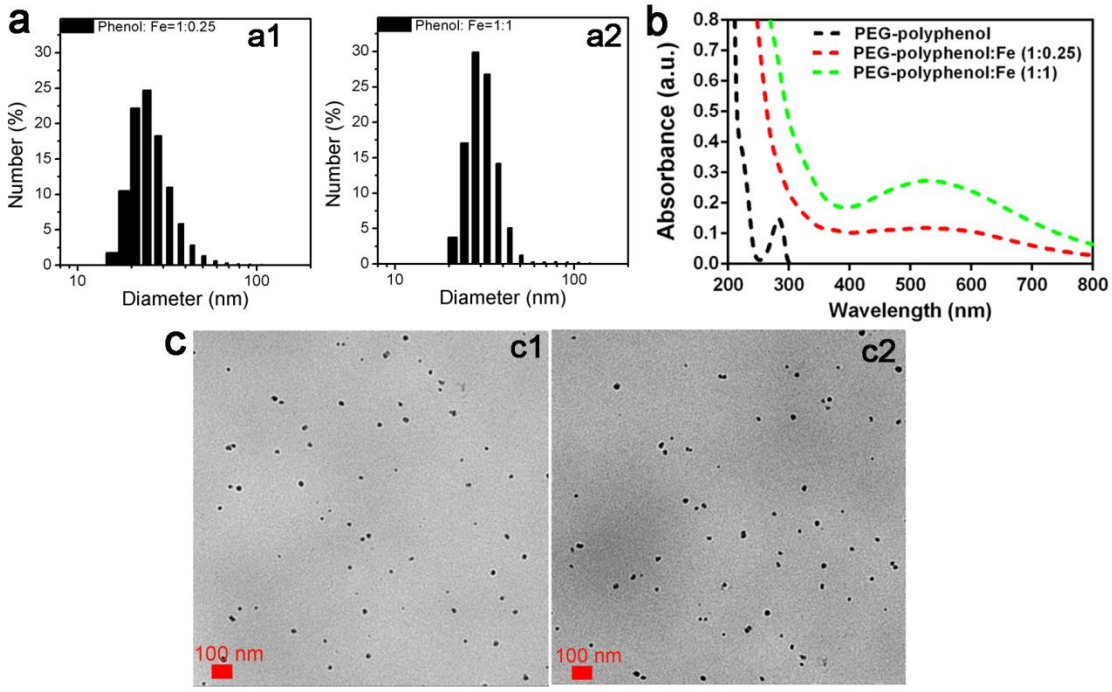

Figure SI4.2. (A) DLS analysis of PEG-gallol/Fe^{III} nanoparticles from different feed ratios, a1: gallol: Fe^{III} =1:0.25, b2: 1:1; (b) UV-vis spectrum of PEG-gallol/Fe^{III} nanoparticles; (c) TEM images of PEG-gallol/Fe^{III} nanoparticles from different feed ratios, c1: gallol: Fe^{III}=1:0.25, c2: 1:1.

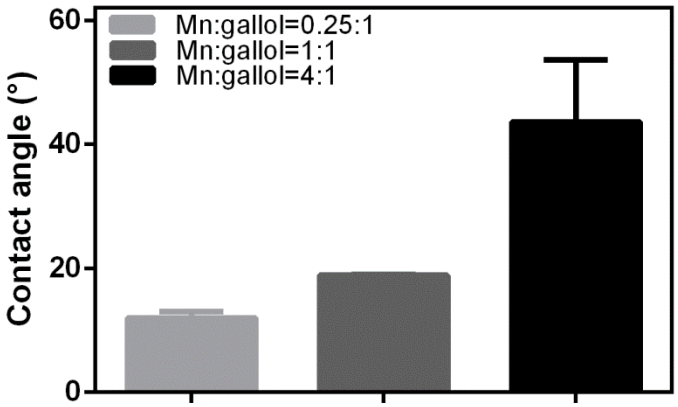

Figure SI4.3. Contact angle of different PEG-gallol/Mn^{II} complexes with different Mn^{II}-to-gallol ratios in Tris buffer (pH 8).

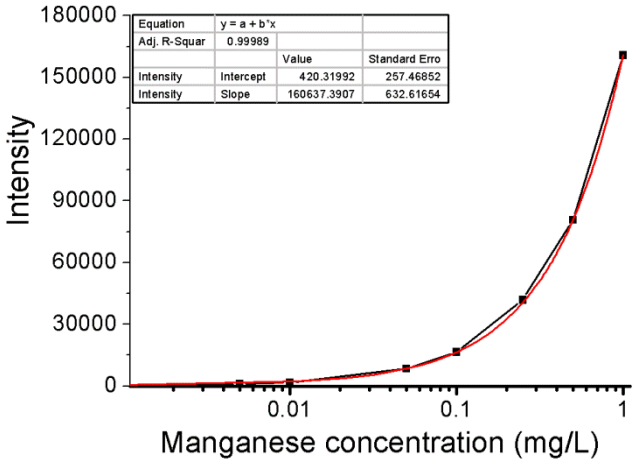

Figure SI4.4. ICP standard curve of manganese ions.

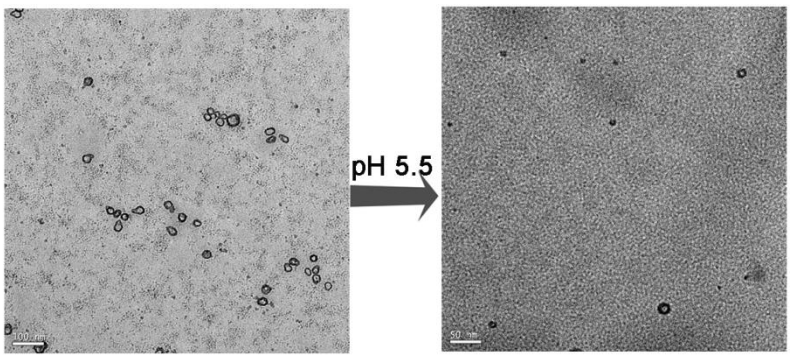

Figure SI4.5. TEM images of PEG-gallol/Mn^{II} nanocapsules in different pH PBS; left: 7.4, right: 5.5.

References

1. Y. Ju, J. Cui, M. Mullner, T. Suma, M. Hu and F. Caruso, Engineering low-Fouling and pH-degradable capsules through the assembly of metal-phenolic networks. *Biomacromolecules*, 2015, **16**, 807-814.
2. N. Bertleff-Zieschang, M. A. Rahim, Y. Ju, J. A. Braunger, T. Suma, Y. Dai, S. Pan, F. Cavalieri and F. Caruso, Biofunctional metal-phenolic films from dietary flavonoids. *Chem Commun (Camb)*, 2017, **53**, 1068-1071.

Chapter 5

Self-Assembled Metal-Phenolic Particles as Light-Steered Microswimmers

5.1. Abstract

Directional motion is commonly observed in organisms, e.g. green algae are able to migrate towards sunlight to receive more energy for photosynthesis. However, such directional motion remains a continuing challenge for synthetic materials. Herein, I report an artificial microswimmer based on metal-phenolic particles that can autonomously sense and swim towards an external light source, with speed delicately tuned by the light intensity. The experimental results and computational calculations offer insights into the detailed mechanism, suggesting the light-induced motion is likely caused by conformational changes of the phenolic ligand, generating a large twist (~55 °) in the planar molecule. The high controllability of motion establishes the metal-phenolic particles as a promising platform for robotics, drug delivery, and environmental applications.

5.2. Introduction

Motion is an essential process in many living organisms. Many living organisms possess the capacity to move towards the environmental stimuli.[1-3] For example, various marine microorganisms (e.g. green algae) can swim to the source of sunlight to optimize photosynthesis for growth.[4] Alternatively, some bacteria and cells present the capacity to migrate towards the sources of chemical gradients for food (e.g. glucose).[5] In all of these movements, the direction of motion is dependent on the direction of the environmental stimulus. However, such directional motion has still proven a daunting challenge for synthetic materials, although the rapid development of artificial micromotors based on different environmental stimuli, such as temperature[6], oxygen[7], H_2O_2[8], magnetic field and light is occurring.[9] For example, the direction and speed of catalyst-based micromotors, which is based on the decomposition of hydrogen peroxide to generate oxygen bubbles for propulsion, highly relies on the concentration of surrounding fuel and thus is difficult to control.[6, 10]

Herein, we report an artificial "phototaxis" based on a metal-phenolic particle consisting of metal ions (Zn^{2+}) and a natural phenolic ligand (ellagic acid, EA). These metal-phenolic particles are able to autonomously and instantaneously sense and swim towards the illumination of ultraviolet (UV) light, with the speed of the motion delicately controlled by the light intensity. This light-oriented movement is likely caused by a photo-excited conformational change in ellagic acid, resulting in a twist in the molecular structure that causes stress within the metal-phenolic particles. Due to its highly controllable movement and tunable size, these metal-phenolic particles could be a promising platform with potential impact in robotics, drug delivery, and environmental applications.

5.3. Results and Discussion

Light-Induced Motion of Metal-Phenolic Particles

Figure 5.1a shows a scheme illustrating the preparation of metal-phenolic particles (MPP). Simply mixing EA and zinc acetate in N-methyl-2-pyrrolidone (NMP) solution gave rise to the metal-phenolic particles. The successful coordination between EA and the Zn^{2+} ion was indicated by the significant decrease of the characteristic -OH vibration peaks (~3144 cm^{-1}) of the EA in the Fourier transform infrared spectra of the metal-phenolic particles (**Figure 5.1b**). The morphology of metal-phenolic particles was observed under scanning electron microscopy (SEM, **Figure 5.1c**), showing the diameter of metal-phenolic particles was around 3 μm (Figure SI5.1). Energy-dispersive X-ray (EDX) spectra (**Figure 1d**) presents the presence of C, O and Zn in the MPP particles, while powder X-ray diffraction (XRD) patterns shows the crystallinity of the metal-phenolic particles were distinct from that of its two precursors (EA and $Zn(OAc)_2$, Figure SI5.2). The nitrogen adsorption data revealed a surface area of 33.1 m^2 g^{-1} and a hierarchical nanopore architecture with a bimodal pore size of ~8 nm and ~12 nm (Figure SI5.3). It was also noticed that the size of metal-phenolic particles can be tuned from 1 to 4 μm, by the variation of the starting precursor concentration (Figure SI5.1, Table SI5.1).

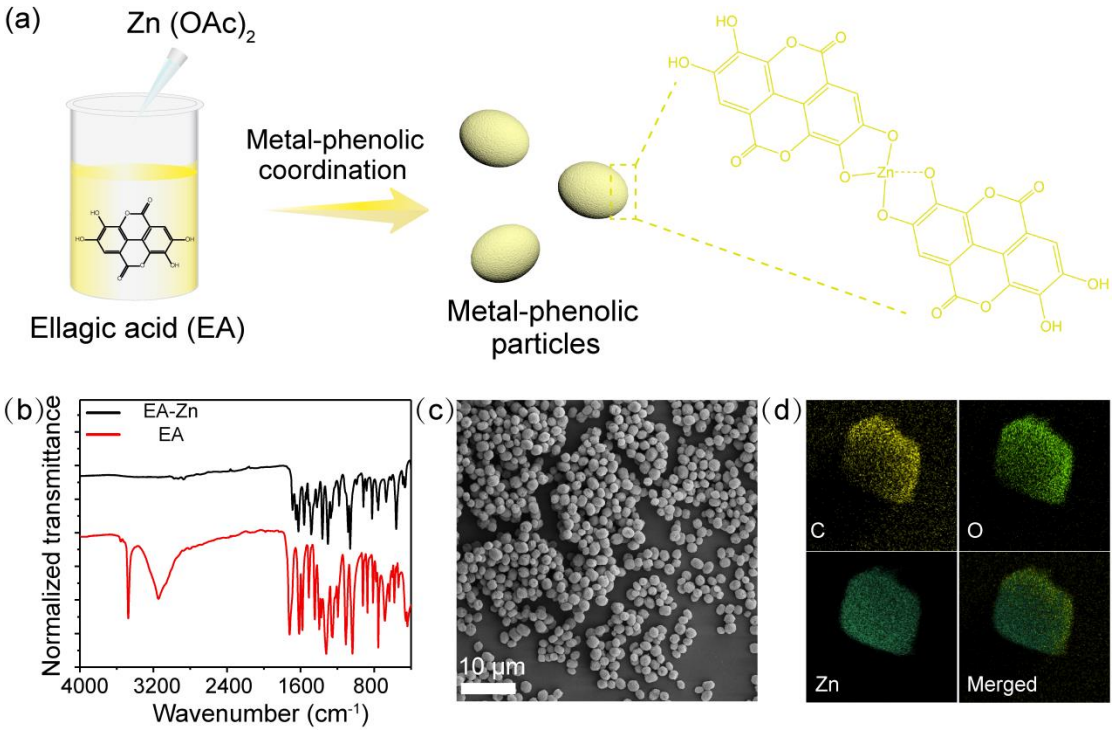

Figure 5.1. Preparation and characterization of the metal-phenolic particles. (a) Schematic illustration of the preparation of the metal-phenolic particles and its chemical composition. Fourier transform infrared (FT-IR) spectra (b), SEM and TEM elemental mapping of the metal-phenolic particles (~ 3 μm).

The positive "phototaxis" property of the metal-phenolic particles was observed at both a macroscopic scale and a microscopic scale (**Figure 5.2a**). A macroscopic scale observation of the three dimensional motion of the MPP particles (0.1 mg/mL) in aprotic solvent (*N*–methyl–2–pyrrolidone, NMP) was first observed by irradiating the metal-phenolic particles dispersion from different sides. The metal-phenolic particles demonstrated a positive "phototaxis" property (swimming towards light) similar to natural E. gracilis, as shown in **Figure 5.2b**. Then, the light-induced motion of the metal-phenolic particles on a microscopic scale was further studied with a fluorescence microscopy. The particle dispersion (0.1 mg/mL) was pipetted onto glass, followed by a UV light illumination. The particles showed a quick movement towards light and the velocity was quantified as 102 μm/s (**Figure 5.2c**), which was significantly higher than in one current report on light-induced micromotors.[11]

However white, green, orange, and red light all failed to activate the microswimmers (Figure SI5.4). Then, we irradiated the metal-phenolic particles dispersion with light "on-off-on" cycle using chopped light. The speed of MPP particles under UV light kept around ~60 μm/s at 0.3 mW/cm^2 illumination (**Figure 5.2d),** the particles only trembled without exposure to ultraviolet light. Then, the effect of the light intensity was also explored by irradiating the metal-phenolic particles with the UV illumination of different light intensity. The speed of metal-phenolic particles scaled linearly with the light intensity, suggesting a high controllability on speed by tuning the illumination intensity (**Figure 5.2e**).

The supernatant of the metal-phenolic particle was subjected to UV-vis and ICP measurement, and the UV-vis spectrum and Zn^{2+} concentration of the supernatant of dispersion with UV irradiation were close to that without UV irradiation (Figure SI5.5), suggesting there was little EA or Zn released during UV irradition. Meanwhile, SEM images shows the metal-phenolic particles maintained their morphologies well after a long time (12 h) of UV exposure (Figure SI5.6).

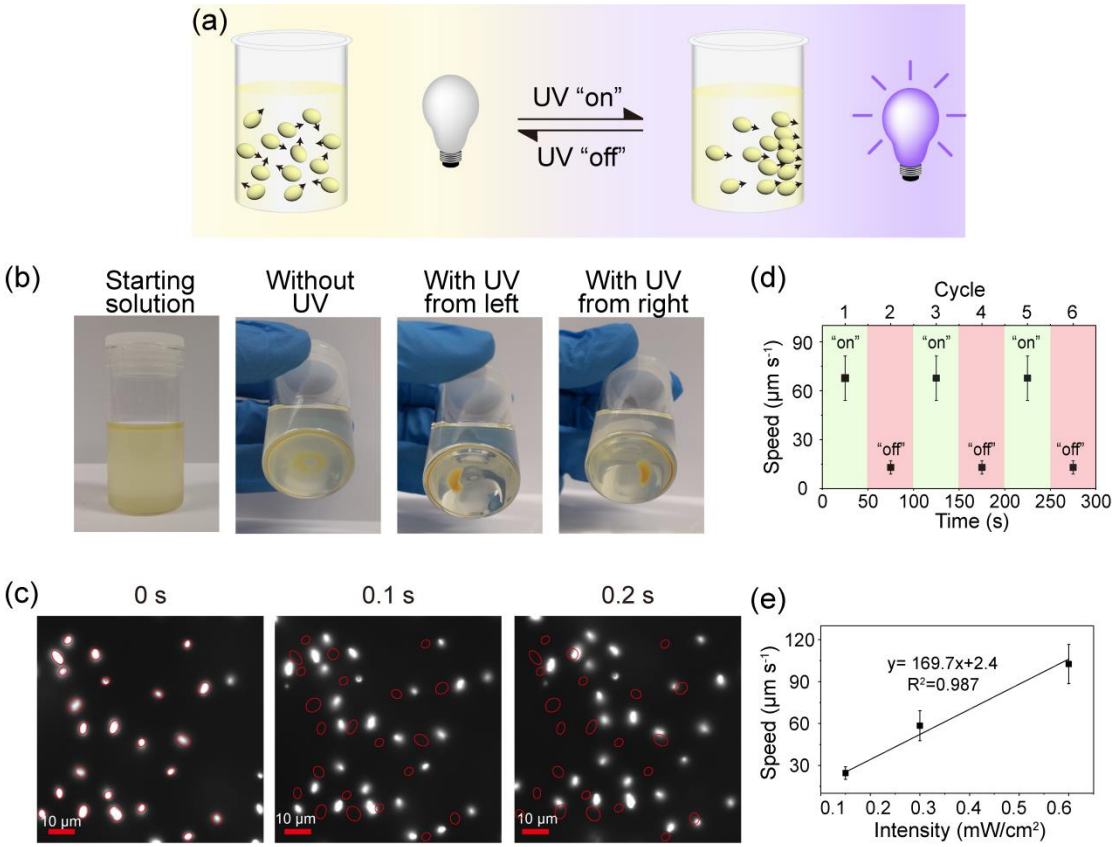

Figure 5.2. Light-steered motion of the metal-phenolic particles. (a) Schematic illustration of light-steered motion of the metal-phenolic particles; (b) Images of starting metal-phenolic particles dispersion, that without UV, with UV illumination from different sides (left and right side). (c) Microscope images of movement of EA-Zn particles upon ultraviolet light (light intensity: 0.6 mW/cm^{-2}). The red circles present the initial positions of the crystals. Scale bar: 10μm; (d) Speed of the metal-phenolic particles under chopped light exposure; (e) Speed of the metal-phenolic particles under different UV light intensities.

Mechanism of Light-Induced Motion

To explore the mechanism of movement, the silica microparticles, precursor materials (EA crystals) and metal-phenolic particles crystals (synthesized using a recent reported method[12]) with similar dimension were dispersed in the NMP, followed by a UV light exposure. The silica particles (~ 2.8 μm) only underwent random Brownian movement both with and without UV irradiation (Figure SI5.7), suggesting the movement of metal-phenolic particles was not caused by the heat from UV or solvent evaporation. However, EA crystals showed a slight movement (Figure

SI5.8), although the speed was significantly lower than that of metal-phenolic particles. These suggested the light-induced movement was likely caused by the chemical reaction in EA when upon the UV exposure in aprotic solvent, where zinc vastly facilitates this reaction.

Then, quantum mechanics (QM) calculations were performed using Gaussian 16[13] on charge-neutral EA to gain insight into the possible chemical reaction pathway of EA. As shown in **Figure 5.3a**, when receiving UV light at ~365 nm, EA (1) undergoes a photo-excited proton transition, resulting in an excited-state structure with a single proton transferred from the adjacent hydroxyl group to the ether oxygen. Interestingly, in the optimized structure the bond between the ether oxygen and carbonyl carbon is broken, forming a planar ketene. In the resultant photo-induced proton transfer structure (2), the distance between the remaining ether oxygen and the adjacent hydroxyl proton is reduced by ~0.15 Å compared to the initial structure. This provides a possible non-radiative structural relaxation pathway, where a second proton transfer is coupled to a twist in the structure as a diketene is formed (3). The diketene exhibits a dihedral angle between the two rings of ~56 °. This UV-induced twist in the molecular structure may cause the stress on the whole MPP particle that be responsible for the observed movement in the crystal under UV light illumination.

The Light-Induced Motion in Different Solvent

To confirm the above hypothesis, we did the same simulation to predict the EA chemical pathways in five different solvents with varying polarity, including water, 1-butanol, DMSO, DMF and 1,4-dioxane (**Table 5.1**). For the aprotic solvents DMSO, DMF, and 1,4-dioxane, both the photo-induced proton transfer and the double proton transfer ground state require much less energy than that in the polar protic solvents (water and 1-butanol). Moreover, there is a 56 ° twist in the resulting structure after

transition in the aprotic solvents, while there is little twist when the protic solvents was used, suggesting the light-induced movement was much easier to induce in the solvents with low polarity than those with high polarity.

Table 5.1. Energies and structural changes for ellagic acid in different solvents.

Solvent	Relative energy (eV)	Corresponding wavelength (nm)	Structure
Water (Ɛ=78.3553)			
Photo-induced proton transfer	3.53	352	Slight twist
Double proton transfer ground state	3.51	354	Planar
1-butanol (Ɛ=17.332)			
Photo-induced proton transfer	3.50	354	Planar
Double proton transfer ground state	3.56	348	Planar
DMSO (Ɛ=46.826)			
Photo-induced proton transfer	3.38	367	Slight twist
Double proton transfer ground state	2.98	416	56 °twist
DMF (Ɛ=37.219)			
Photo-induced proton transfer	3.39	366	Planar
Double proton transfer ground state	2.98	416	56 °twist
1,4-dioxane (Ɛ=2.2099)			
Photo-induced proton transfer	3.36	370	Planar
Double proton transfer ground state	3.02	411	55 °twist

To experimentally validate the calculation, the metal-phenolic particles were dispersed in these five solvents (water, 1-butanol, DMSO, DMF and 1,4-dioxane), followed by the UV light illumination. Consistent with that in the calculation, metal-phenolic particles did not induce light-steered motion and just trembled in polar solvent (water and 1-butanol), but shows obvious light-induced motion in aprotic solvents (DMSO, DMF and 1,4-dioxane), as shown in Figure SI5.9. The speed of the motion was quantified, showing the speed of MPP motion increased with the decrease in solvent polarity (**Figure 5.2b**). Then, the speed of the MPP particles in the mixed

solvent (DMF/1-Butanol) was further investigated (Figure SI5.10). The speed of MPP was 103 μm/s in the commercial DMF, but it gradually decreased with the addition of 1-butanol and finally lose the light-induced motion capacity (**Figure 5.3c**). We infer the addition of 1-butanol change the chemical environment of EA so that EA require more energy to undergo the photo-induced proton and double proton transition. When a significant amount of 1-Bunatol (e.g. 25%) was added into the system, the energy required for the transition was higher than what is provided by 365 nm UV light that is unable to induce proton transition and thus the light-induced motion of metal-phenolic particles.

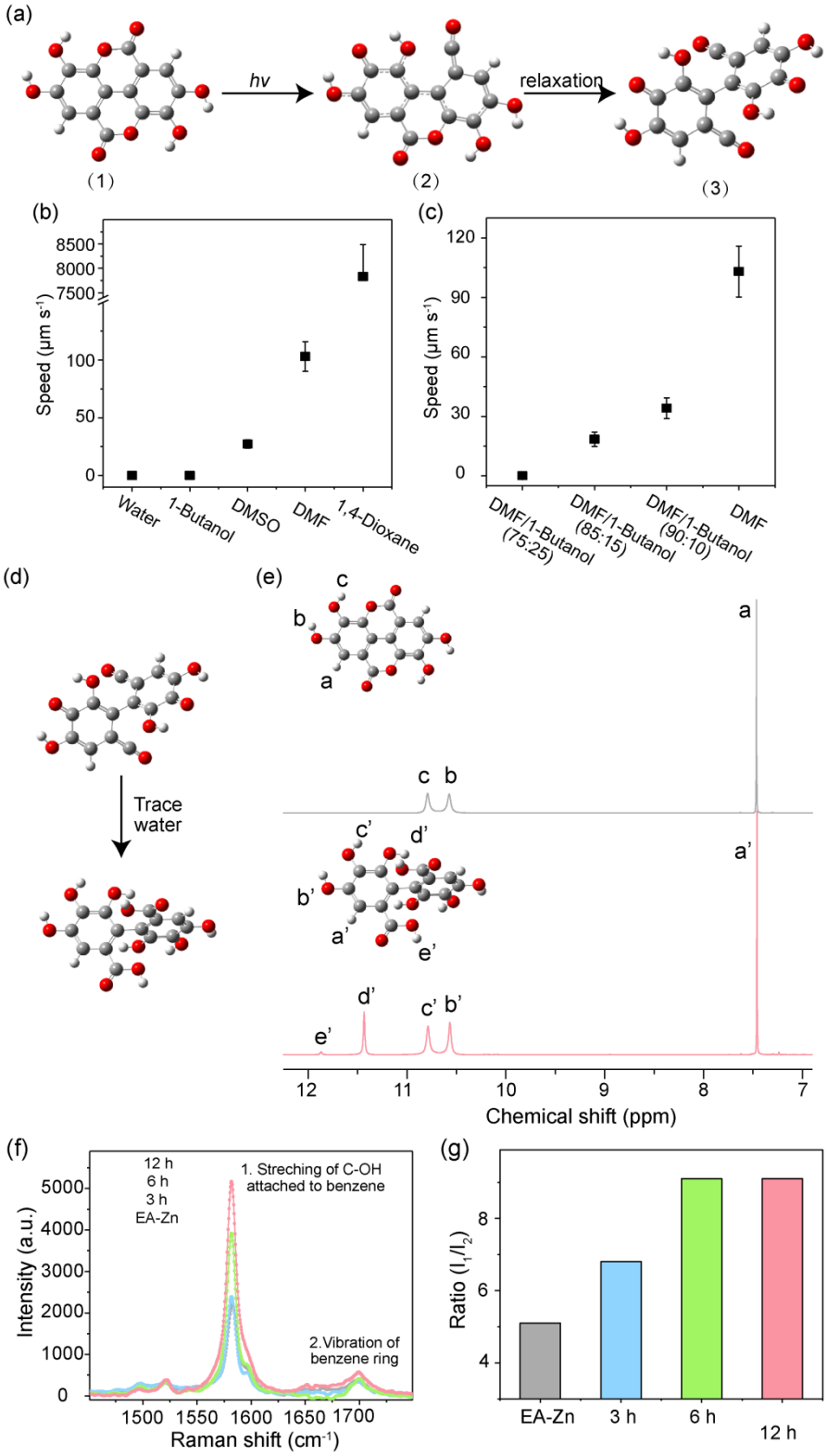

Figure 5.3. Suggested mechanism of light-steered motion of the metal-phenolic particles. (a) Possible molecular conformational changes of EA in aprotic solvents under UV light; the excited state was approximated by in quantum mechanics calculations density functional theory (DFT). (b) Speed of the metal-phenolic particles in different solvents (light intensity: 0.6 mW/cm^2); (c) Speed of the metal-phenolic particles in the mixed (DMF/1-Butanol) solvents (light intensity: 0.6

mW/cm^{-2}); (d) The chemical reaction between the excited molecule after double proton transfer with the trace water in the commercial aprotic solvent; (e) ^{1}H-NMR of EA and EA NMP dispersion after 24 h UV irradiation; (f) Raman spectral of metal-phenolic particles and those after different period of UV irradiation. (g) the ratio between the peak of hydroxyl stretching and that of benzene ring vibration in Raman spectral.

Then, we compared the particles fluorescence (Figure SI5.11) and speed in different solvents when upon UV light illumination. As shown in Table 5.2, there is a well negative correlation between the speed and the polarity of solvent, that is the speed increase with decrease in solvent polarity. Meanwhile, neither the particles fluorescence nor the solvent viscosity correlated with the particle's speed. Taken together, these suggested the polarity of the solvent is the dominant factor determining the speed of light-induced movement, which affects the chemical environment of EA when determine required energy for the proton transfer and further molecular twist.

Table 5.2. The velocity and fluorescence of EA-Zn particles in different solvents with varying polarity and viscosity.

Solvent	Polarity	Velocity	Viscosity (cp, 20 ℃)	Fluorescence
Water	+++++	**N/A**	**1**	+
1-Butanol	++++	**N/A**	**2.95**	++
DMSO	+++	+	**1.99**	+++
DMF	++	++	**0.92**	+++
1,4-dioxane	+	++++	**1.44**	++

Molecular Evidence

In the above photo-excited pathway, the diketene exhibits a dihedral angle between the two rings of ~56 °. The structure is likely short-lived, may reacting with any trace water in the solvent system and result in the hydrolysis of EA and form hexahydroxydiphenic acid (**Figure 5.3d**). ^{1}H NMR and Raman spectral were used to

inspect the molecular changes in EA and metal-phenolic particles, respectively. ^{1}H NMR spectral shows there were two additional peaks in ^{1}H NMR of the EA after UV exposure (**Figure 5.3e**. table SI5.2), 11.34 ppm and 11.86 ppm; the former was assigned to the additional hydroxyl group and the latter carbonyl group attached to the benzene group, confirming the hydrolysis of EA into hexahydroxydiphenic acid. Meanwhile, the hydrolysis of EA on the MPP particles was tracked by Raman spectroscopy, due to some limitations in ^{1}H NMR failing to yield nice spectra as the metal-phenolic particles are too big to rotate.

Figure 5.3f shows the two typical peaks of the metal-phenolic particles, ~1580 cm^{-1} and ~1700 cm^{-1}. The former peak was assigned to the stretching of the hydroxyl group attached to the benzene, and the latter was assigned to vibration of benzene. The stretching of hydroxyl of metal-phenolic particles increased gradually with the time of UV light exposure, while the vibration of benzene was almost constant. The ratio between the peak of hydroxyl group stretching and that benzene vibration was calculated, and it increased gradually and remained steady with the increase in UV exposure time, suggesting the additional of hydroxyl group, in agreement with ^{1}H NMR data.

5.4. Conclusion

We have presented a light-steered synthetic microswimmer based on metal-phenolic particles, which mimics the ‘phototaxis of natural motile algae and self-aligns with the direction of light. Our experimental and computational simulation generates insights into the detailed mechanism behind the light-induced motion of these particles, and also predicts the motion in different solvent. These metal-phenolic

microswimmers have several advantages: i) the simple and robust synthetic approach suggests the scalability of particles synthesis; ii) the movement is steered by the direction of the light source render the movement high controllability, due to the superior spatial and temporal precision of the light[14], iii) the pore within the metal-phenolic particles could be applied for loading cargos for diver application in various field, including robotics, drug delivery and environmental applications.

5.5. References

(1) Kreimer, G. Cell biology of phototaxis in flagellate algae. In *International Review of Cytology*; Jeon, K. W.; Jarvik, J., Eds.; Academic Press: 1994; pp 229-310.

(2) Bhaya, D. Light matters: phototaxis and signal transduction in unicellular cyanobacteria. *Molecular Microbiology* **2004,** *53* (3), 745-754, DOI: 10.1111/j.1365-2958.2004.04160.x.

(3) Kaupp, U. B.; Hildebrand, E.; Weyand, I. Sperm chemotaxis in marine invertebrates—molecules and mechanisms. *Journal of Cellular Physiology* **2006,** *208* (3), 487-494, DOI: 10.1002/jcp.20669.

(4) Haxo, F. T.; Blinks, L. R. Photosynthetic action spectra of marine algae. *The Journal of General Physiology* **1950,** *33* (4), 389, DOI: 10.1085/jgp.33.4.389.

(5) Adler, J. Chemotaxis in bacteria. *Annual Review of Biochemistry* **1975,** *44* (1), 341-356, DOI: 10.1146/annurev.bi.44.070175.002013.

(6) Tu, Y.; Peng, F.; Sui, X.; Men, Y.; White, P. B.; van Hest, J. C. M.; Wilson, D. A. Self-propelled supramolecular nanomotors with temperature-responsive speed regulation. *Nature Chemistry* **2016,** *9*, 480, DOI: 10.1038/nchem.2674.

(7) Felfoul, O.; Mohammadi, M.; Taherkhani, S.; de Lanauze, D.; Zhong Xu, Y.; Loghin, D.; Essa, S.; Jancik, S.; Houle, D.; Lafleur, M.; Gaboury, L.; Tabrizian, M.; Kaou, N.; Atkin, M.; Vuong, T.; Batist, G.; Beauchemin, N.; Radzioch, D.; Martel, S. Magneto-aerotactic bacteria deliver drug-containing nanoliposomes to tumour hypoxic regions. *Nature Nanotechnology* **2016,** *11*, 941, DOI: 10.1038/nnano.2016.137

(8) Wu, Y.; Si, T.; Gao, C.; Yang, M.; He, Q. Bubble-pair propelled colloidal kayaker. *Journal of the American Chemical Society* **2018,** *140* (38), 11902-11905, DOI: 10.1021/jacs.8b06646.

(9) Bozuyuk, U.; Yasa, O.; Yasa, I. C.; Ceylan, H.; Kizilel, S.; Sitti, M. Light-triggered drug release from 3D-printed magnetic chitosan microswimmers. *ACS Nano* **2018,** *12* (9), 9617-9625, DOI: 10.1021/acsnano.8b05997.

(10) Gao, S.; Hou, J.; Zeng, J.; Richardson, J. J.; Gu, Z.; Gao, X.; Li, D.; Gao, M.; Wang, D.-W.; Chen, P.; Chen, V.; Liang, K.; Zhao, D.; Kong, B. Superassembled biocatalytic porous framework micromotors with reversible and sensitive pH-speed regulation at ultralow physiological H_2O_2 concentration. *Advanced Functional Materials* **2019,** *29* (18), 1808900, DOI: 10.1002/adfm.201808900.

(11) Dai, B.; Wang, J.; Xiong, Z.; Zhan, X.; Dai, W.; Li, C.-C.; Feng, S.-P.; Tang, J. Programmable artificial phototactic microswimmer. *Nature Nanotechnology* **2016,** *11*, 1087, DOI: 10.1038/nnano.2016.187

(12) Bhangu, S. K.; Singla, R.; Colombo, E.; Ashokkumar, M.; Cavalieri, F. Sono-transformation of tannic acid into biofunctional ellagic acid micro/nanocrystals with distinct morphologies. *Green Chemistry* **2018,** *20* (4), 816-821, DOI: 10.1039/C7GC03163G.

(13) Frisch, M. J.; Trucks, G. W.; Schlegel, H. B.; Scuseria, G. E.; Robb, M. A.; Cheeseman, J. R.; Scalmani, G.; Barone, V.; Petersson, G. A.; Nakatsuji, H.; Li, X.; Caricato, M.; Marenich, A. V.; Bloino, J.; Janesko, B. G.; Gomperts, R.; Mennucci, B.; Hratchian, H. P.; Ortiz, J. V.; Izmaylov, A. F.; Sonnenberg, J. L.; Williams; Ding, F.; Lipparini, F.; Egidi, F.; Goings, J.; Peng, B.; Petrone, A.; Henderson, T.; Ranasinghe, D.; Zakrzewski, V. G.; Gao, J.; Rega, N.; Zheng, G.; Liang, W.; Hada, M.; Ehara, M.; Toyota, K.; Fukuda, R.; Hasegawa, J.; Ishida, M.; Nakajima, T.; Honda, Y.; Kitao, O.; Nakai, H.; Vreven, T.; Throssell, K.; Montgomery Jr., J. A.; Peralta, J. E.; Ogliaro, F.; Bearpark, M. J.; Heyd, J. J.; Brothers, E. N.; Kudin, K. N.; Staroverov, V. N.; Keith, T. A.; Kobayashi, R.; Normand, J.; Raghavachari, K.; Rendell, A. P.; Burant, J. C.;

Iyengar, S. S.; Tomasi, J.; Cossi, M.; Millam, J. M.; Klene, M.; Adamo, C.; Cammi, R.; Ochterski, J. W.; Martin, R. L.; Morokuma, K.; Farkas, O.; Foresman, J. B.; Fox, D. J. *Gaussian 16 Rev. B.01*, Wallingford, CT, 2016.

(14) van Leeuwen, T.; Lubbe, A. S.; Štacko, P.; Wezenberg, S. J.; Feringa, B. L. Dynamic control of function by light-driven molecular motors. *Nature Reviews Chemistry* **2017,** *1* (12), 0096, DOI: 10.1038/s41570-017-0096.

5.6. Supporting Information

1. Materials

Zinc acetate dihydrate (98%), ellagic acid hydrate (EA, technical grade), *N*–methyl–2–pyrrolidone (NMP), dimethylformamide (DMF, 99%) dimethyl sulfoxide (DMSO, 99%), 1-butanol and 1,4-dioxane were purchased from Sigma-Aldrich. The Milli-Q water was obtained from a water purification system (Millipore RiOs/Origin). The glass slides were purchased from knittel Glass(German).

2. Synthesis of metal-phenolic particles

The metal-phenolic particles were synthesized by a simple mixing EA and zinc acetate dihydrate. Briefly, 0.052 mmol of EA and 0.104 mmol zinc acetate dihydrate were dissolved in 10 ml of NMP solvent in a 15 mL vial in 25 ℃. After 24 h, the metal-phenolic particles were separated with centrifugation and washed with NMP and ethanol for three times to remove free small complexes. The metal-phenolic particles were dispersed in NMP for further experiments before use. The metal-phenolic particles with different sizes were synthesized under different precursor concentration (10.4, 5.02, 2.51, 1.25 M) with a constant EA/Zn ratio (1:2) by using the same protocol.

3. Characterization

The size and morphology of EA-Zn particles was observed on an inverted microscope (Olympus IX71) and scanning electron microscope (SEM, Nova 200 Nanolab, FEI). Element distribution determination was characterized by energy-dispersive X-ray (EDX) spectroscopy under transmission electron microscopy (TEM, F20). For the SEM and TEM observation, 5 μL of particles suspensions was allowed to air dry on piranha solution pretreated silicon slides and Formvar carbon-coated copper grids, respectively.

The analysis of the crystalline structure of EA, zinc acetate dihydrate and metal-phenolic (EA-Zn) particles was performed by X-ray powder diffraction (D8 Advance, Bruker, Australia) with a step size of 0.02°, and a 2θ range of 6°–90° at a scan rate of 2° min-1. X-ray photoelectron spectroscopy (XPS) analysis was conducted on a spectrometer equipped with a hemispherical analyzer (VG ESCALAB 220i-XL). The reference for energy calibration was the C 1s peak at 285.0 eV.

4. Light-induced motion experiment

The setting-up of the motion test in a macroscopic scale is shown below in Figure SI5.3. The metal-phenolic particles were dispersed in NMP (0.1 mg/mL) in a 15 mL transparent glass vial. Then, the vial was irradiated with a portable UV lamp (366 nm, 610 μW/cm²) from different sides (right and left). After 6 h, the EA-Zn particles settled down onto the bottom of the vial gradually. The photos of the vials after different light exposure from different sides were taken using commercial a commercial cell photo.

The observation of the motion test in a microscopical scale is carried out under an inverted fluorescence microscopy (Olympus IX71). The metal-phenolic particles (0.1 mg/mL) was pipetted onto a glass, followed by the UV light source in the fluorescence microscopy. A powerful 120W metal halide lamp with tunable intensity (X-Cite, series 120Q) was used as the light source in this study and a small silicon photo diode was used to measure the UV light intensity. The video was recorded under a high resolution camera using the OCULAR program. The image was analyzed using image J to quantify the motion of the metal-phenolic particles. At least 20 particles were randomly selected to calculate the average speed of metal-phenolic particles. In this part, a small silicon photo diode was used to measure the UV light intensity

5. The motion of metal-phenolic particles in different solution

Same as the above light motion test, the quantification of the motion speed of the metal-phenolic particles in different solvent with varying polarity was performed under an inverted Olympus IX71 fluorescence microscope. First, the particles dispersion (0.1 mg/mL, water, 1-butanol, DMSO, DMF and 1,4-Dioxane) was pipetted onto a glass, followed by the UV light (0.6 mW/cm^{-2}) in the fluorescence microscope. The light-induced motion was recorded using Ocular program and then analyzed by image J to calculate the speed of the metal-phenolic particles in different solvent.

6. Hydrolysis of EA and metal-phenolic (EA-Zn) particles

The hydrolysis of EA was monitored by ^{1}H-NMR. The free EA NMP solution was treated with 24 h of the light illumination of a UV lamp (365 nm). Then the solution was subjected for lyophilization. The product was dissolved in DMSO-d5 and characterized using 1H-NMR.

The hydrolysis of EA in metal-phenolic (EA-Zn particles) was characterized using by Raman spectral using confocal Raman microscopy. After different period UV illumination, the EA-Zn particles was centrifugated and washed with fresh NMP thrice. The particles was dispersed in NMP and then subject to Raman spectral analysis. For the sample preparation for Raman spectral analysis, 5 μL of particles suspensions was allowed to air dry on aluminium foil covered glass. The Raman spectrums of free EA, EA-Zn particles before and after UV illumination were taken using confocal Raman microscope (HORIBA LabRAM HR Evolution) with a 532 nm laser probe (Ar ion laser). Each sample was prepared by casting 5 μL suspensions on gold nanoparticles coated glass slide, followed by air dry. A 50 objective lens was used for focusing the laser beam on the sample. The acquisition time was 10 s, the

grating rate was 1800 grooves/mm and the spectral resolution was ~1 cm-1. The spectra represented the average of 3 accumulations.

7. Computational Calculation

Quantum mechanics (QM) calculations were performed using Gaussian 16 on charge-neutral ellagic acid in density functional theory (DFT). All calculations were performed at the M062X/6-311+G(d,p) level of theory with Grimme's D3 dispersion correction.[1] Structures were optimized in implicit water, 1-butanol, dimethyl sulfoxide (DMSO), n,n-dimethyl formamide (DMF), and 1,4-dioxane. The SMD[2] model was used to assess the effects of implicit solvation.

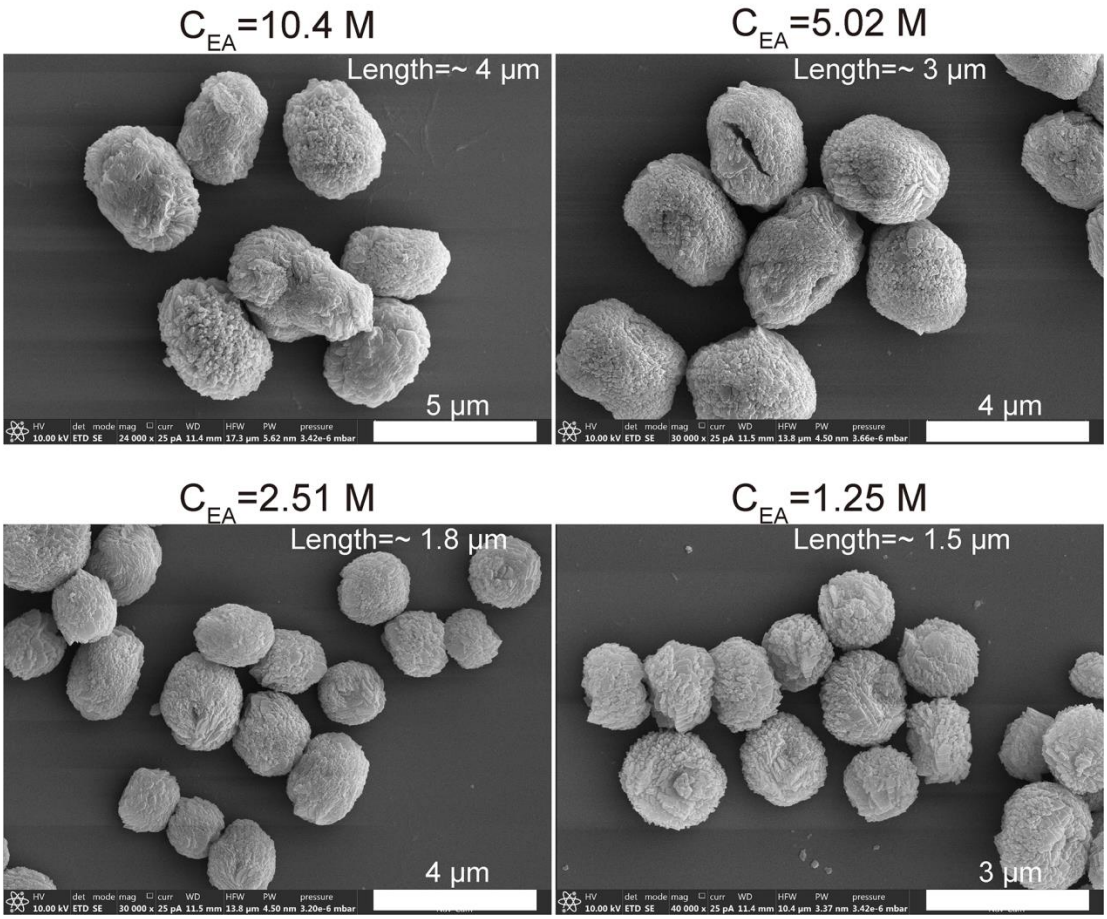

Figure SI5.1. SEM images of metal-phenolic particles obtained from the reaction with different ellagic acid concentration.

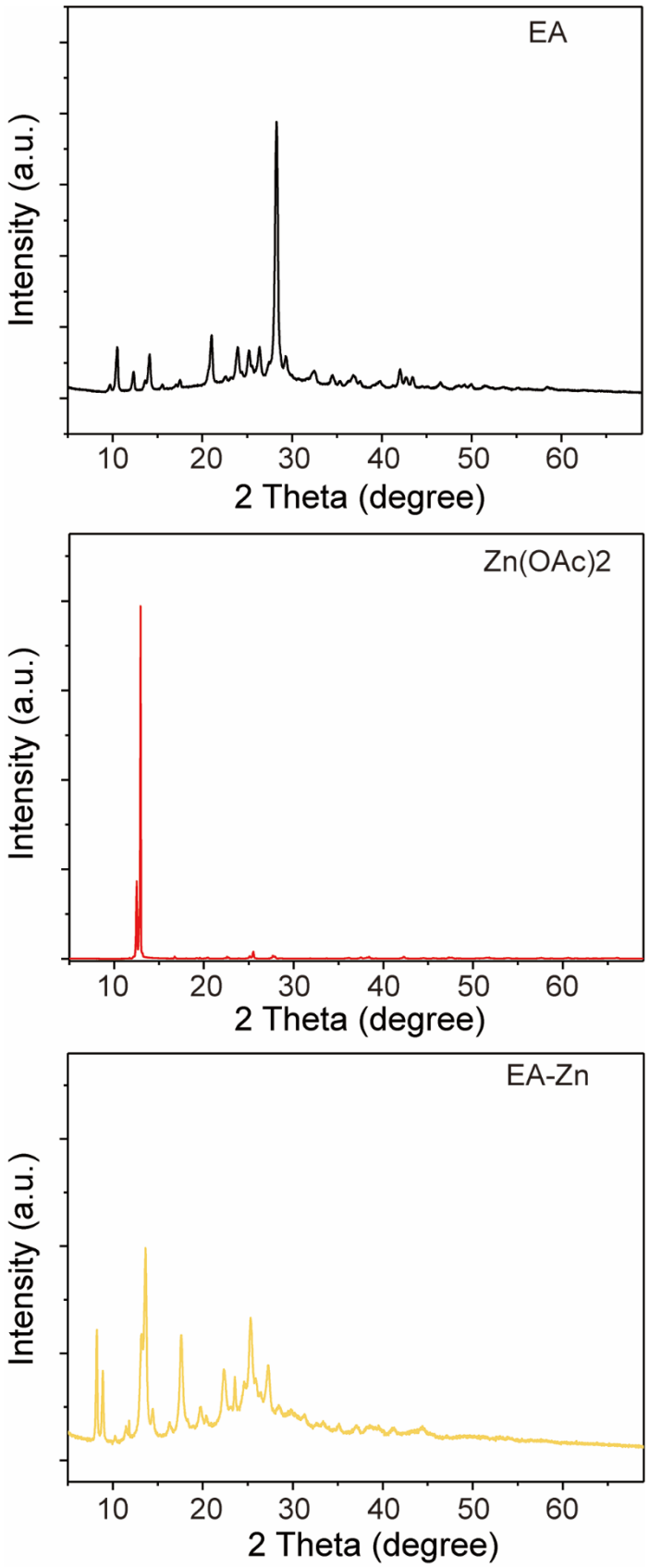

Figure SI5.2. XRD patterns of ellagic acid, zinc acetate dehydrate, and EA-Zn particles.

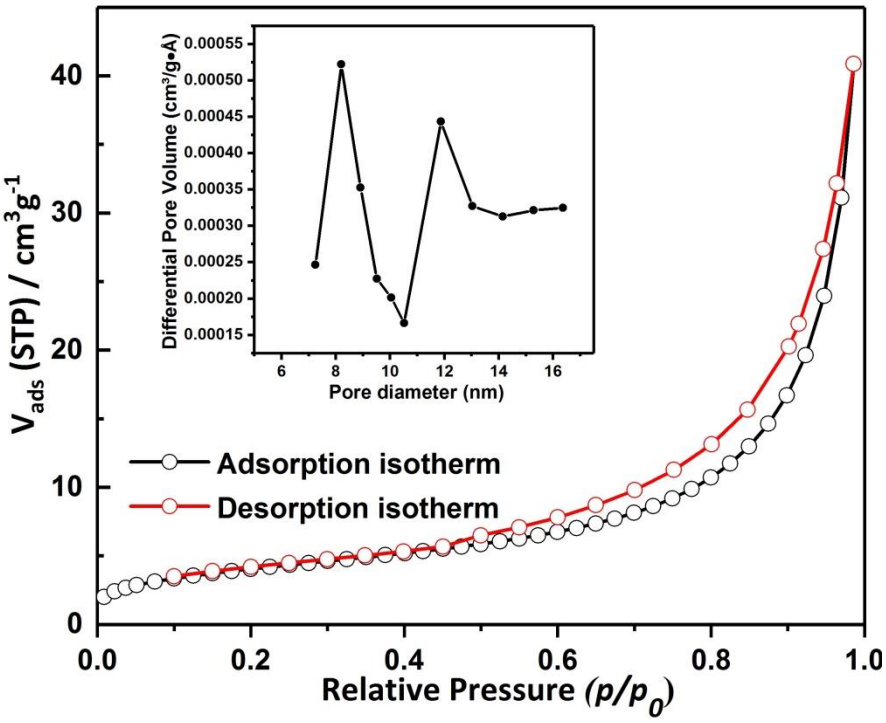

Figure SI5.3. Nitrogen isotherms at 77 K and pore size distribution of the metal-phenolic particles (inserted figure), calculated from nitrogen isotherms with the quenched solid density functional theory model.

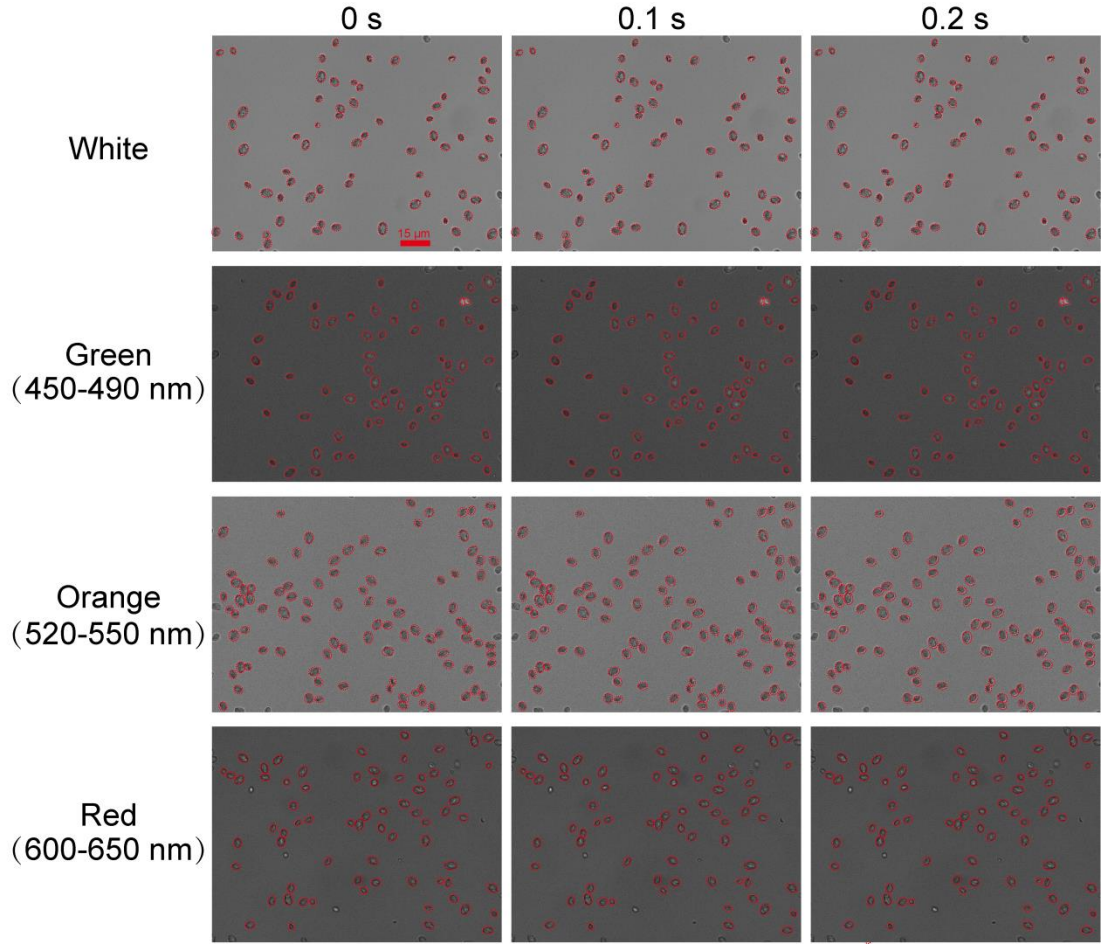

Figure SI5.4. The microscopic image showing the motion of metal-phenolic particles illuminated with white, green, organ and red light. The red circles represent the initial positions of the microswimmers, while the arrow indicates the direction of motion.

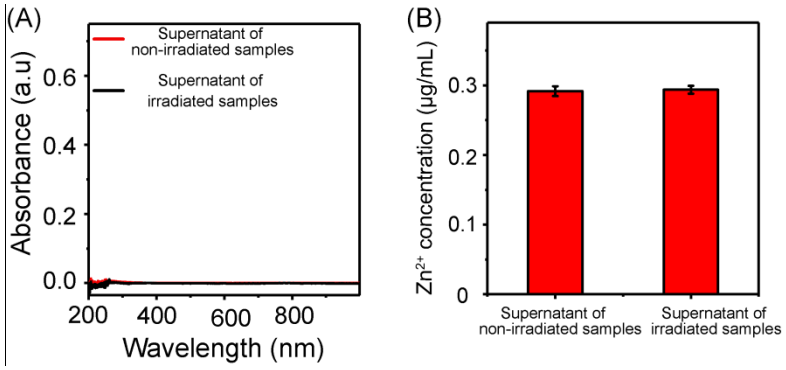

Figure SI5.5. (a) UV-vis spectral of supernatant of metal-phenolic particles dispersion with or without UV light illumination; (b) Zn^{2+} concentration of the supernatant of metal-phenolic particles dispersion with or without UV light illumination, determined by ICP.

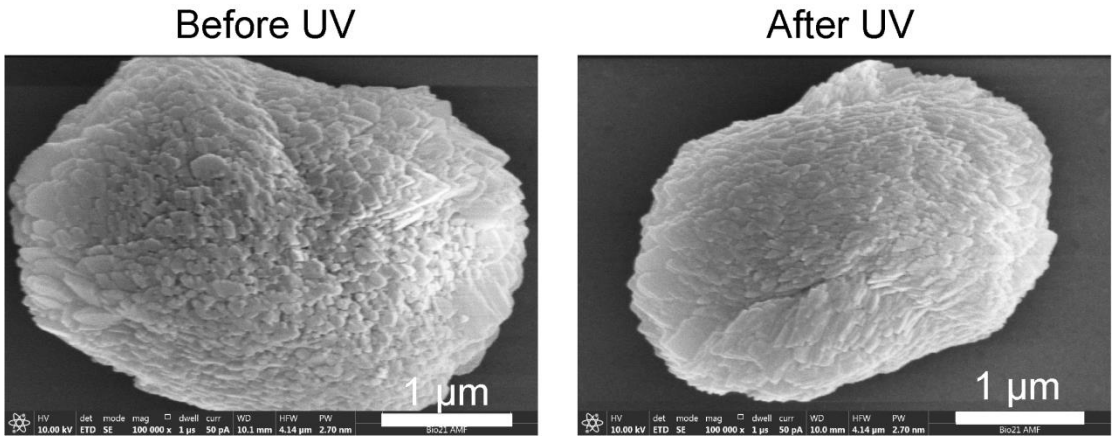

Figure SI5.6. SEM images of metal-phenolic particle before (a) and after (b) 24 h UV light illumination.

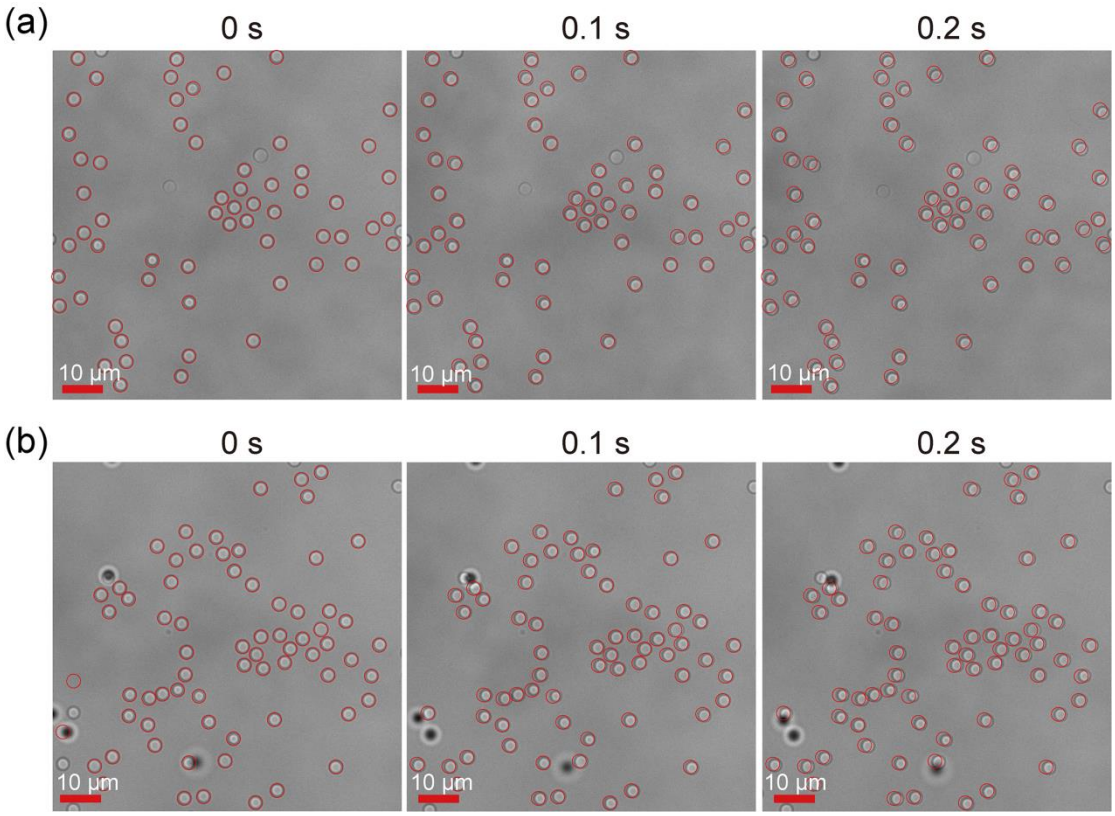

Figure SI5.7. Images of silica particles (~ 2.8 μm) in NMP solution when without (a) or with UV light illumination (b).

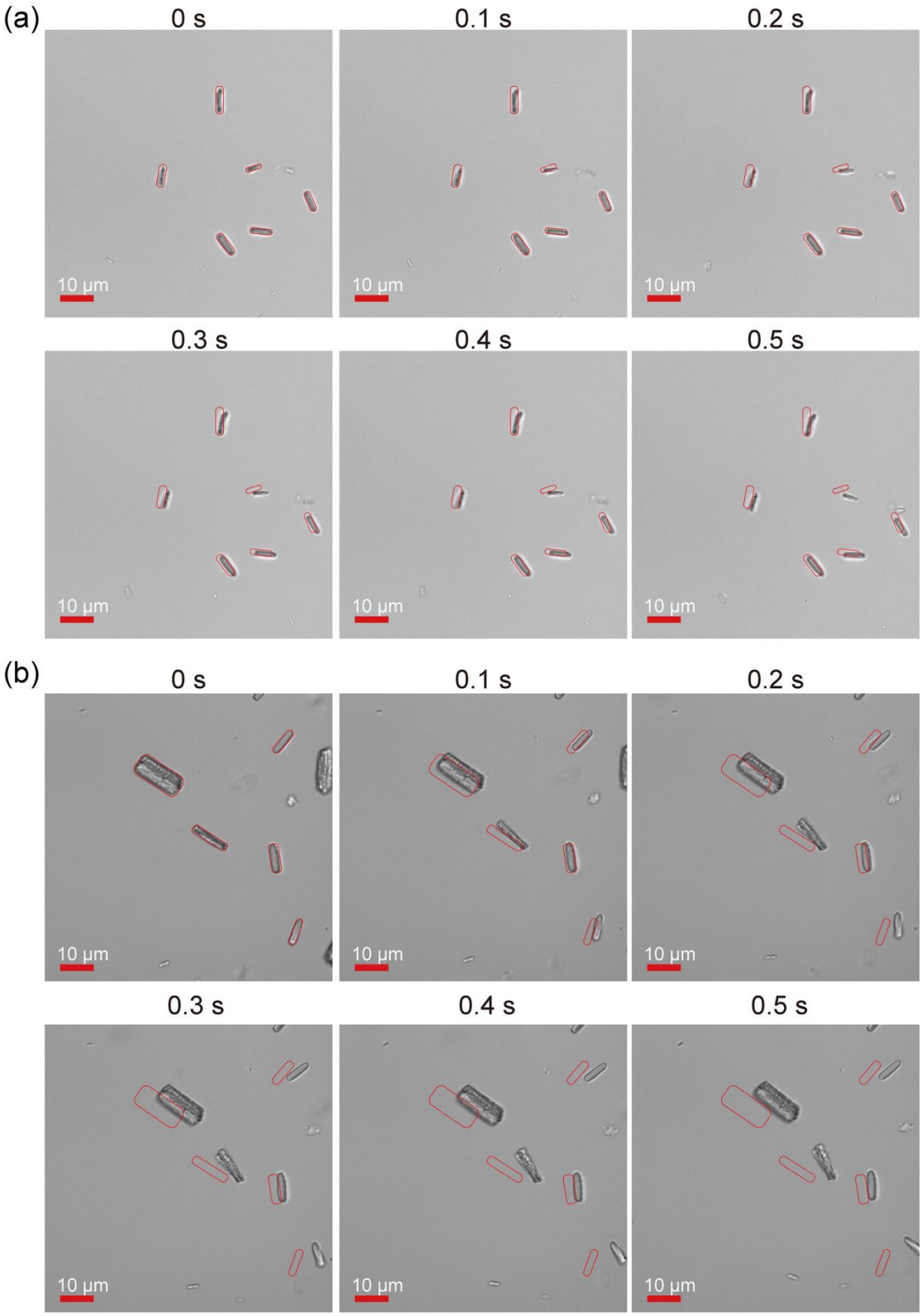

Figure SI5.8. Images of EA crystals in NMP solution when without (a) or with UV light illumination (b).

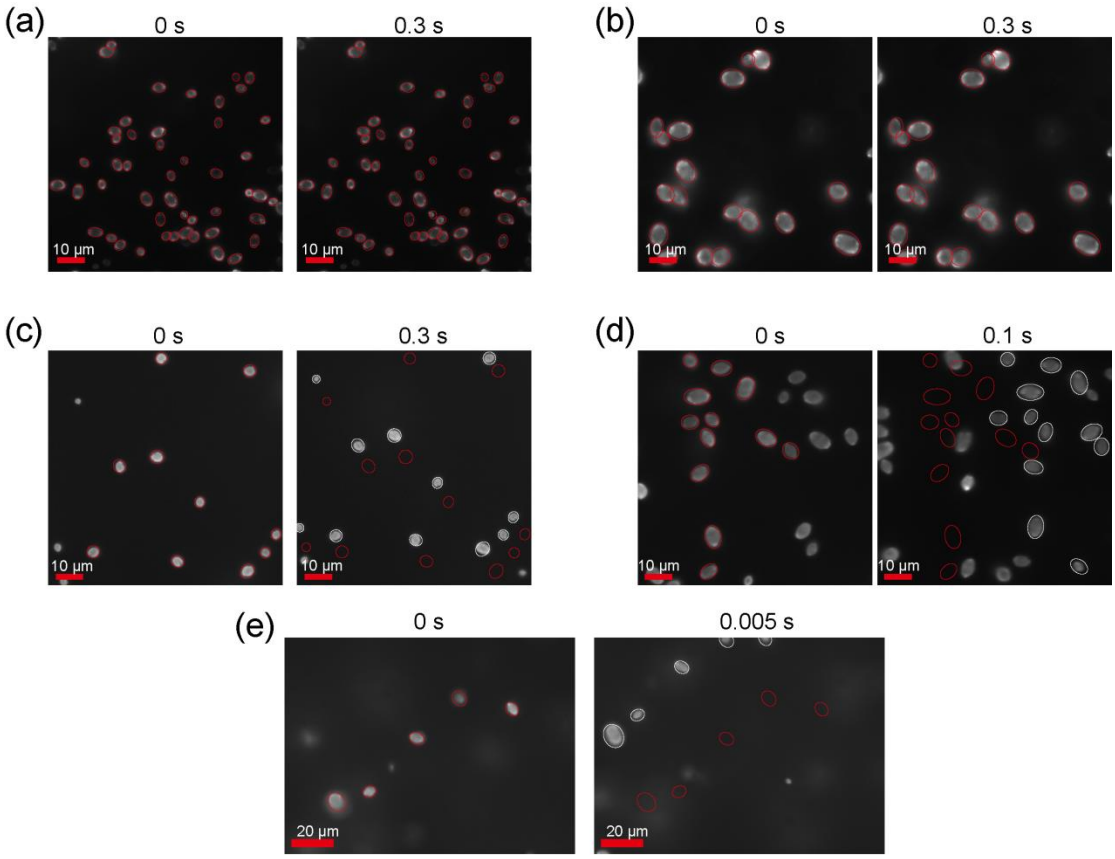

Figure SI5.9. Images of metal-phenolioc particles in different solvent: water (a), 1-butanol (b), DMSO (c), DMF (d) and 1,4-dioxane (e) when receiving the UV illumination. In (c), (d) and (e), the red circles present the initial positions of the metal-phenolic particles, while the white one present the positions of the metal-phenolic particles at the end-points.

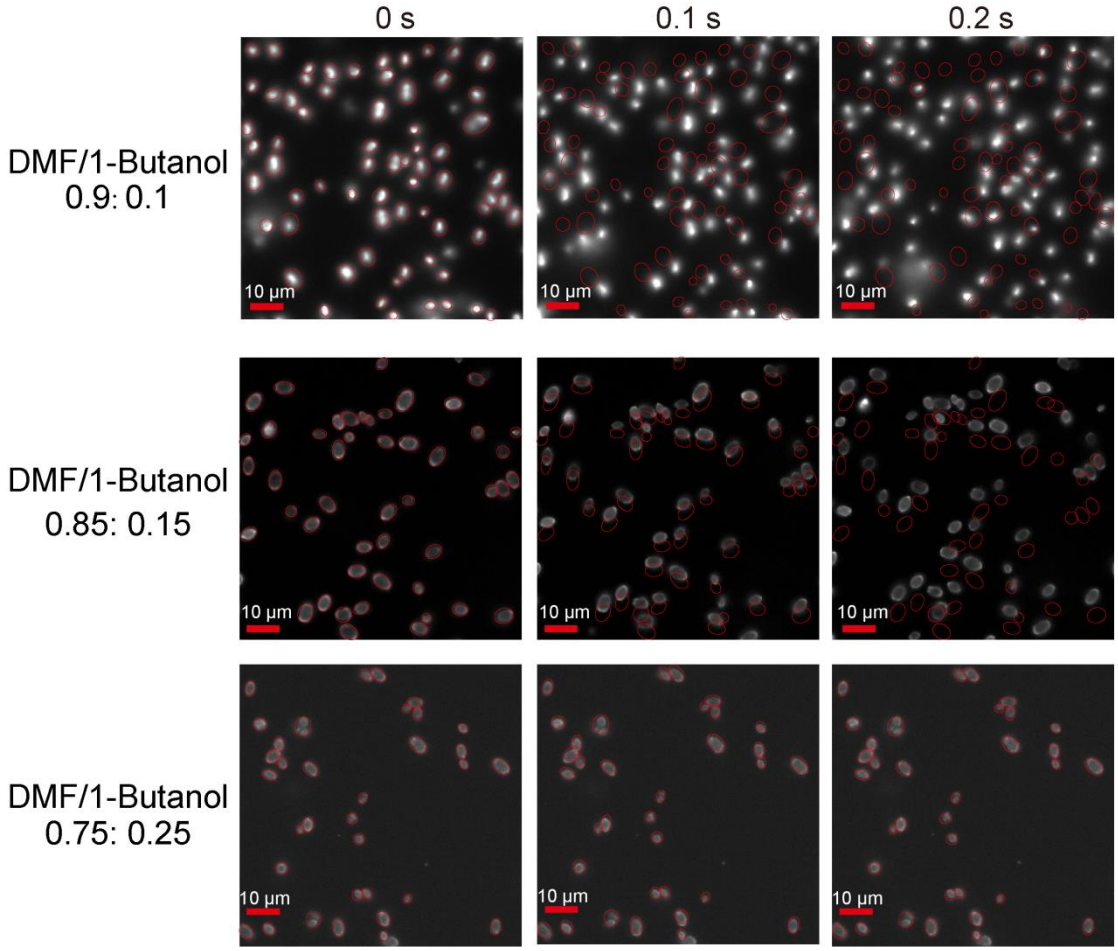

Figure SI5.10. Images of metal-phenolic particles in NMP solution in different mixed solvent (DMF/1-butanol) with varying ratios. The red circles present the initial positions of the metal-phenolic particles.

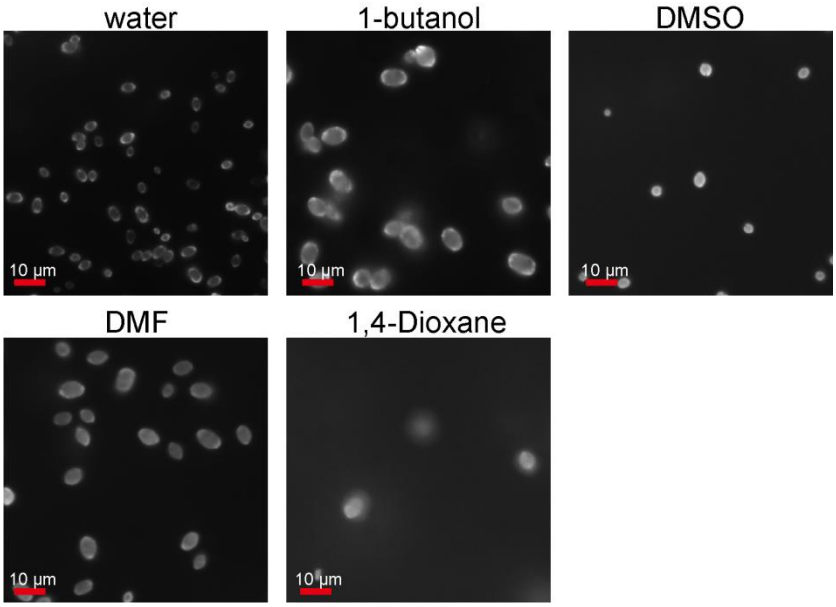

Figure SI5.11. Images of metal-phenolic particles in different solvent under UV light.

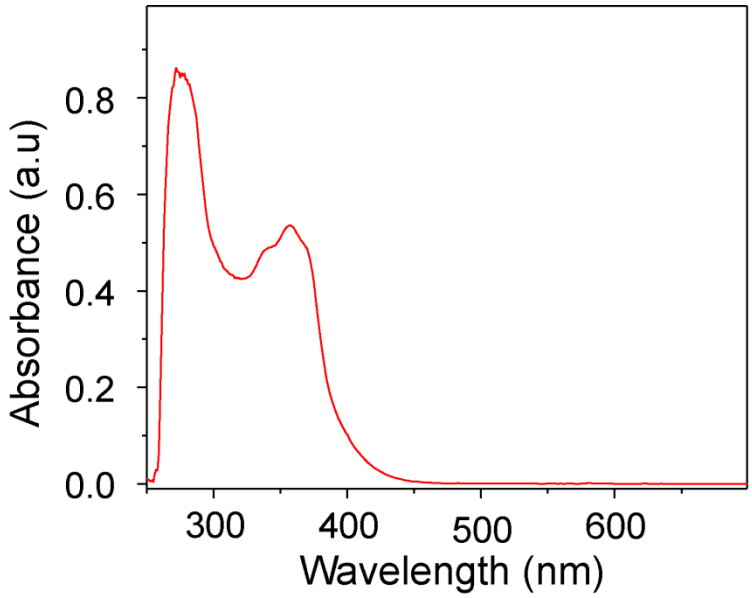

Figure SI5.12. UV-vis spectral of ellagic acid in NMP solution;

Table SI5.1. Size of metal-phenolic particles synthesized from different starting EA concentration.

Starting concentration (EA, M)	Average Size (μm)
1.25	1.62 ± 0.23
2.51	1.89 ± 0.32
5.02	3.06 ± 0.30
10.4	4.02 ± 0.62

Table SI5.2. Relative peak integral in ^{1}H-NMR of EA before and after UV illumination.

Chemical Shift (ppm)	7.45	10.56	10.78	11.34	11.86
Before UV	1	1	1		
After UV	1	0.99	0.97	0.67	0.01

References

(1) Grimme, S.; Antony, J.; Ehrlich, S.; Krieg, H. A consistent and accurate ab initio parametrization of density functional dispersion correction (DFT-D) for the 94 elements H-Pu. *The Journal of Chemical Physics* **2010,** *132* (15), 154104, DOI: 10.1063/1.3382344.

(2) Marenich, A. V.; Cramer, C. J.; Truhlar, D. G. Universal solvation model based on solute electron density and on a continuum model of the solvent defined by the bulk dielectric constant and atomic surface tensions. *The Journal of Physical Chemistry B* **2009,** *113* (18), 6378-6396, DOI: 10.1021/jp810292n.

Chapter 6

Conclusions and Perspectives

In summary, the versatility of metal-phenolic coordination for the assembly of particles and films was explored to construct multifunctional metal-phenolic materials with unique properties and tunable sizes and morphologies. By utilizing different assembly techniques, the combination of phenolic ligand and metal ions gives arise to a series of novel metal-phenolic materials, from hollow capsules to solid nano/microparticles. Metal-phenolic assembly using natural extracts containing multiple phenolic ligands was investigated to expand the phenolic library due to the ubiquitous occurrence of phenolic compounds in nature (e.g. plants, herbs, tea, etc.). The selective property of metal-phenolic assembly elucidated in this thesis provides a facile way to fabricate multifunctional MPN capsules using natural extracts for diverse applications. By using soft templates small sized (sub-100 nm) metal-phenolic particles with potential application in drug delivery can be produced. Finally, the self-assembly of phenolic ellagic acid and Fe was shown to form metal-phenolic particles with positive “phototaxis” property, highlighting potential novel applications (i.e., micromotors) using metal-phenolic materials.

In **Chapter 3**, MPN films were prepared using a natural extract (eucalyptus (Euc) leaf extracts) containing multiple phenolic ligands. Metal-phenolic assembly from this multi-component mixture demonstrated selectivity, where metal ions (Fe^{III}) selectively assemble

with phenolic components (e.g., myricetrin and quercetrin) even if present at low abundance in the mixture to form thin films on various templates, irrespective of template properties. Computational simulation of the metal-phenolic assembly using a model multi-component mixture suggests that the driving force for the selective behavior likely results from the differences in the number of possible chelating sites in the phenolic ligands. The resulting MPN films from eucalyptus leaf extracts showed recyclable antioxidant properties, demonstrating the potential for metal-phenolic assembly as a promising technique for the fabrication of natural, free-standing antioxidant films. In addition, the strategy developed here expands the toolbox of phenolic ligands for metal-phenolic assembly to natural multi-ligand extracts, and due to selective assembly, negates the need for isolation and purification of mono-ligands for MPN assembly.

In **Chapter 4**, a facile approach to engineer PEG particles with tunable size and morphology was developed by controlling the metal-phenolic coordination of multi-arm PEG-gallol in microemulsions. The range in size and morphology was likely influenced by the amphiphilicity of the PEG-gallol/Mn^{II} complexes, which could be tuned according to Mn-to-gallol ratios, as supported by contact angle measurements. SAXS was used to study intermolecular interaction during particle evolution, and showed by fitting analysis that ionic charges were the dominant

driving force in converting free PEG-gallol/Mn^{II} into the different. The pH sensitivity, low cytotoxicity, and low-fouling properties of the resulting PEG particles suggests their potential as delivery systems.

In **Chapter 5**, self-assembled metal-phenolic particles with positive "phototaxis" property were reported from coordination between metal (Zn^{II}) and ellagic acid (a natural phenolic acid). The particles were able to autonomously sense and "swim" towards an external light source, as seen in natural motile algae. The speed of motion could be precisely tuned by light intensity. Quantum mechanics calculation combined with experimental data suggests the possible driving force for the movement is the generation of a conformational change (large twist) in the planar molecule caused by proton transfer when ellagic acid is subjected to UV light illumination. The facile synthesis, tunable size and controllable motion of these metal-phenolic swimmers could be useful in biomedical and engineering applications, including cargo delivery and environmental remediation.

This thesis combines studies on the design and synthesis of novel metal-phenolic materials via different assembly techniques, including hard template-based, soft templates (microemulsions)-based and template-free assembly. Future work that exploit the properties of these materials is critical to fully realize their potential. The selective assembly in Euc extracts provides a facile and cheap technique to make

multifunctional hollow capsules using a natural source of phenolic compounds. Other types of natural extracts (e.g. fruits and vegetables extracts) can also be explored in the future. Besides antioxidant properties, other health benefits commonly associated with phenols (e.g., antibacterial, anticancer) could arise from these natural MPN capsules. Along this line, the effect of these MPN capsules on cancer cells and bacteria could be investigated, followed by the investigation on their mechanism of action. Moreover, the selective metal-phenolic assembly presented here could also be applicable in other multi-component mixtures to allow separation of phenolic compounds according to the number of chelating sites available, providing a facile method to isolate and separate phenolic compounds of interest.

PEG is the most commonly used synthetic material for imparting “stealth” property to materials and biomacromolecules to reduce protein association and uptake by phagocytes in the blood, making PEG-based particles attractive for drug delivery applications. The ability to tune the size and morphology of PEG particles, as demonstrated in this thesis, can lead to delivery systems with tunable biodistribution and drug release properties. The size of PEG-gallol/metal ion nanoparticles may also be tuned by changing the composition (e.g. water-to-cyclohexane ratio) of the microemulsion system, which can be investigated in future studies. Combined with the pH sensitivity, low cytotoxicity, and low-fouling

properties of the PEG particles, further drug loading and in vivo studies in animal models is warranted.

The UV light-induced “swimming” ability of EA-Zn metal-phenolic particles provides an exciting area of research. The tunability of the light-induced movement could open new applications for metal-phenolic materials in robotics (microswimmers), drug delivery, environmental remediation and biotechnology. Future work will explore the possible extension and application of the current system to other types of phenolic compounds (e.g. GA, TA, EGCG) and metal ions (Fe^{III}, Mn^{II}, Cu^{II}, Ti^{iv} and etc), and investigate if composition can influence and further control the phototaxis properties of particles.